UNIVERSITÀ DEGLI STUDI DI CATANIA

DIPARTIMENTO DI FISICA E ASTRONOMIA

DOTTORATO DI RICERCA IN FISICA

ROBERTO CATALANO

EXPERIMENTAL AND MODELING METHODS TO STUDY RADON TRANSPORT PROCESSES IN POROUS MEDIA

PH.D. THESIS

Ph.D. Coordinator: Chiar.mo Prof. F. RIGGI

Tutor: Chiar.ma Prof.ssa G. IMMÉ

XXVI CICLO

Contents

Introduction 1

Chapter 1

Radon diffusion models 4

1.1 Characteristics of radon and its decay products 4
1.2 Radon exhalation 6
1.3 Theory of radon diffusion 12
1.3.1 Plate sheet model 12
1.3.2 Infinite source model 18
1.3.3 Radon transport in dry, cracked soil 20
1.3.4 Radon transport in unsaturated soil 24

Chapter 2

Radon transport in porous materials: RnMod3d model 32

2.1 Basic definitions 32
2.2 Radon transport equation 34
2.3 Soil-gas transport equation 38
2.4 RnMod3d treatment of radon and soil gas 41
2.5 Finite-volume method 43
2.5.1 Solution procedure 45
2.5.2 Boundary conditions 48
2.5.3 A study case 49
2.5.4 Special considerations 51
2.5.5 Model limitations 52

Chapter 3

In situ measurements on Mt. Etna volcano …… 53

3.1 Tectonic structure ……... 53
3.1.1 Eastern Sicily ……... 57
3.2 Mt. Etna …….. 58
3.2.1 Site location ……. 62
3.3 Experimental devices …….. 64
3.3.1 Genitron AlphaGUARD ionization chamber …….. 65
3.3.2 Durridge RAD7 solid state detector …… 67
3.3.3 CR-39 nuclear track solid state detector …….. 69
3.4 Radon transport in fracturated porous media …….. 70
3.4.1 Results and discussion ……. 71
3.5 In-soil radon vertical profile ……... 75
3.5.1 Results and discussion ……. 76

Chapter 4

Experimental set-up and procedure ……. 80

4.1 Laboratory facility …….. 81
4.1.1 Radon concentration determination ……. 85
4.1.2 Temperature variations …… 85
4.2 Radon source characterization …… 87
4.2.1 Thoron attenuation inside the vessel……. 91
4.3 Radon detectors intercalibration ……. 93
4.4 Material properties …….. 100
4.4.1 Grain size, density and porosity ……... 100
4.4.2 Radium content …… 103
4.4.3 Radon emanation coefficient ……... 103
4.5 Computer code …… 105

Chapter 5

Laboratory measurements and results …… 106

5.1 Sample characteristics …… 106
5.2 Experimental procedures and analysis methods ……. 109
5.3 Experiments with upward advective transport ……... 112
5.3.1 Model description …… 113
5.3.2 Results and discussion ……. 116
5.4 Experiments with temperature variations ……... 124
5.4.1 Results and discussion ……. 126
5.5 Considerations on samples porosity ……... 134

Concluding remarks and future perspectives ……... 137

Appendix A ……..……... 140

References ……... 147

Introduction

Radon is a naturally occurring radioactive gas that is produced in the Earth's crust as a result of alpha-decay of radium and is free to migrate through soil, either by molecular diffusion or by advection, and be released to the atmosphere where his behavior and distribution are mainly governed by meteorological processes. Advection, in particular, may transfer radon over a wide range of distances, depending on the porosity and on the velocity of the carrier fluid. Due to its unique properties, soil gas radon has been established as a powerful tracer used for a variety of purposes, such as exploring uranium ores, locating geothermal resources and hydrocarbon deposits, mapping geological faults, predicting seismic activity or volcanic eruptions and testing atmospheric transport models. Much attention has also been paid to the health radiological hazard due to increased radon concentrations in the living and working environment.

In order to exploit radon profiles for geophysical purposes and also to predict its entry indoors, it is necessary to study its transport through porous soils. The complexity generated by the presence of a great number of uncontrollable and varying parameters and processes affecting the generation of radon in the soil grains and its transport in the source medium (pore-water distribution, permeability, porosity, radium content, radon emanation coefficient, advection, …), has led to many theoretical and/or laboratory studies. To measure these quantities *in situ*, in fact, it is not only hard, it is almost impossible to keep them constant during an experiment. Moreover, soil, as it is found *in situ*, is inhomogeneous due to mixing of different layers by geological and/or human activity, and it is influenced by flora and fauna presence, etc. The complexity is even larger if one considers, for example, that radon diffusion is mainly governed by porosity but not strongly influenced by pore size or pore size distribution.

For these reasons, laboratory measurements are preferred, allowing for experiments to be conducted under well-specified and controlled conditions. This approach constitutes the main basis for the study presented in this thesis. Therefore, a laboratory facility was built consisting of a large cylindrical vessel, homogeneously filled with different materials, with inserted sleeves that allow measurements of radon concentrations in the sample gas at various depths under the sample column surface. The vessel can be closed with a stainless steel cover, the space under the cover above the sample simulating a crawl space, and, in addition, a nearly homogeneous air-flow pattern can be induced in the column by means of two inlets at the bottom of the vessel. The results of the laboratory measurements are compared with expected concentrations, according to a transport model developed by C.E. Andersen (Risø National Laboratory, Denmark) and suitably adapted for our purposes.

The main goal of the present study is to better understand how some parameters could affect radon transport in porous media, through both *in situ* and laboratory measurements. In chapter 1 a brief introduction to the radon characteristics is given together with the description of some of the most widely-used and reliable models to describe the radon transport in porous media. In chapter 2, the physics of radon transport in porous materials is outlined in the framework of RnMod3d derived by Andersen. The derivation is made such that the mathematical equations remain applicable for multiphase transport in inhomogeneous media, i.e. for a porous medium containing a solid, liquid and gas phase. In this respect, the description is 'broader' than necessary to account for the transport phenomena studied with the radon vessel.

Chapters 3, 4 and 5 cover the experimental methods and techniques. In particular, in chapter 3, *in situ* measurements of radon activity concentration, together with soil thoron and carbon dioxide efflux on Mt. Etna volcano are discussed. Both horizontal and vertical profiles of radon activity concentration were studied, even in the close proximity of active faults. A comparison between experimental data and model calculations has been also performed. In chapter 4, the laboratory facility installed at the Environmental Physics Laboratory of the Department of Physics and Astronomy (University of Catania) is described in detail, with a description of the procedures and

equipment for measuring the material sample pore-air radon concentration The properties of the different sample materials (volcanic sand, volcanic rock, marble sand and clay), important for radon generation and radon transport are described in this chapter as well. Finally, in chapter 5, the results of measurements with steady-state combined diffusive and advective transport in low-moisture samples for different air-flow rates, temperatures and porosity are discussed and compared with analytical solutions of the governing differential equations given by 3D radon transport model.

Finally, concluding remarks are drawn on the experimental extracted in particular in laboratory measurements at controlled conditions and on the comparison of the data with radon transport model.

Future perspectives of this kind of study are envisaged because it represents a noticeable tool from different points of view, in particular *i)* for radioprotection by establishing optimal conditions of the materials, in particular building materials to mitigate indoor radon risk, *ii)* for geophysical investigation to enlighten on the role of radon gas as precursor of geodynamical events, in particular magma up-rise, but more studies in this direction are yet necessary.

Chapter 1

Radon diffusion models

1.1 Characteristics of radon and its decay products

Radon is a naturally occurring radioactive gas and it is one of the products of the natural decay chains of uranium and thorium, which are present in soil and rocks with varying concentrations according to the specific mineralogical and geological characteristics. It exists in three different isotopes: ^{222}Rn, member of ^{238}U series, with an half life of 3.82 days, ^{220}Rn (also called thoron), member of ^{232}Th series, with an half life of 54.5 s and ^{219}Rn, member of ^{235}U series, with an half life of only 3.92 s. In figure 1.1 are shown the radioactive decay chains.

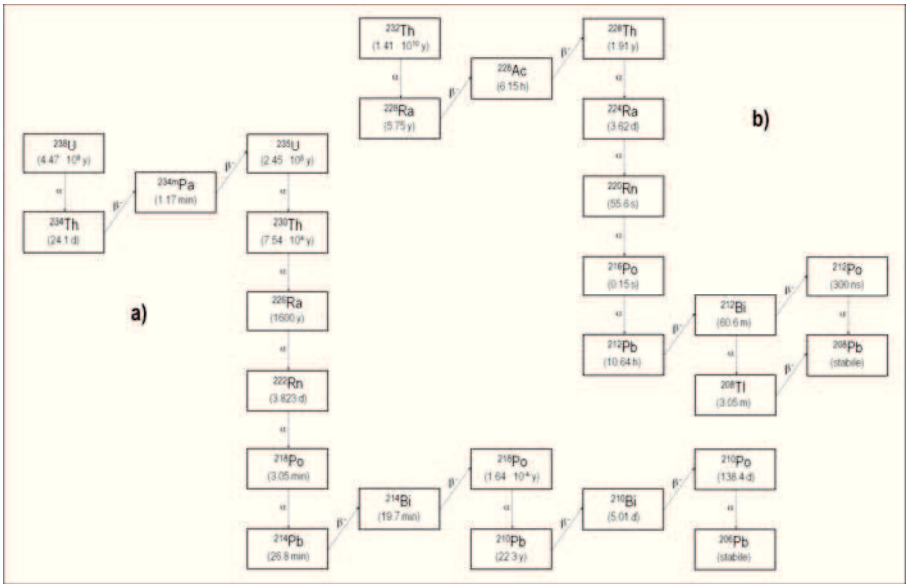

Figure 1.1 - Radioactive decay chains of ^{238}U (a) and ^{232}Th (b)

Owing to its higher half life, the most important of them is ^{222}Rn, the daughter of ^{226}Ra. After its production in soil or rock, ^{222}Rn can leave the terrestrial crust either by molecular diffusion or by convection and enter the atmosphere where its behavior and distribution are mainly governed by meteorological processes. The radon decay products are radioactive isotopes of Po, Bi, Pb and Tl and they easily attach to aerosol particles present in air. In table 1.1 the principal decay characteristics of ^{222}Rn and ^{220}Rn are shown, including properties of their respective parent radionuclides and their short-lived decay products.

Table 1.1 - Principal decay characteristics of ^{222}Rn and ^{220}Rn

Radionuclide	Half life	Radiation	E_α (MeV)	E_γ (MeV)
^{226}Ra	1600 y	α	4.78 (94.3%)	0.186 (3.3%)
			4.69 (5.7%)	
^{222}Rn	3.824 d	α	5.49 (100%)	-
^{218}Po	3.05 m	α	6.00 (100%)	-
^{214}Pb	26.8 m	β,γ	-	0.295 (19%)
				0.352 (36%)
^{214}Bi	19.7 m	β	-	0.609 (47%)
				1.120 (15%)
				1.760 (16%)
^{214}Po	164 µs	α	7.69 (100%)	-
^{224}Ra	3.66 d	α	5.45 (6%)	0.241 (3.9%)
			5.68 (94%)	
^{220}Rn	55.6 s	α	6.29 (100%)	-
^{216}Po	0.15 s	α	6.78 (100%)	-
^{212}Pb	10.64 h	β,γ	-	0.239 (47%)
				0.300 (3.2%)
^{212}Bi	1.01 h	α,β,γ	6.05 (25%)	0.727 (11.8%)
			6.09 (10%)	1.620 (2.8%)
^{212}Po	298 ns	α	8.78 (100%)	-
^{208}Tl	3.05 m	B,γ	-	0.511 (23%)
				0.583 (86%)
				0.860 (12%)
				2.614 (100%)

The production of ^{222}Rn depends on the activity concentrations of ^{226}Ra in the earth's crust. Trace concentrations of radium of various levels are present in soil,

rock, water and building materials. Some estimates of the activity concentration of the uranium and thorium series in soil are reported in table 1.2.

Table 1.2 - Activity concentration in some rocks

Type of rock	Example	Concentration (Bq kg^{-1})			
		^{226}Ra		^{228}Ra	
		Average	Range	Average	Range
Acid intrusive	Granite	78	1 – 370	111	0.4 – 1030
Basic extrusive	Basalt	11	0.4 – 41	10	0.2 – 36
Chemical sedimentary	Limestone	45	0.4 – 340	60	0.1 – 540
Detrital sedimentary	Clay, shale, sandstone	60	1 – 990	50	0.8 – 1470
Metamorphosed igneous	Gneiss	50	1 – 1800	60	0.4 – 420
Metamorphosed sedimentary	Schist	37	1 - 660	49	0.4 - 370

1.2 Radon exhalation

Radon enters the atmosphere mainly by crossing the soil-air interface. The contributions of other sources such as oceans, lakes and rivers are relatively small. Radon from ground water or natural gas released into enclosed spaces may sometimes be important.

Since soil has 10^3-10^4 times higher gas concentrations than the normal surrounding atmosphere, there is a great radon concentration gradient between such materials and open air. This gradient is permanently maintained by the constant generation of radon by its long-lived parent predecessor from the ^{238}U series present in the material. The amount of radon activity released from the surface expressed in Bq m^{-2} s^{-1} is called the *exhalation rate*. Mechanisms governing the exhalation of radon from the soil are illustrated in figure 1.2. The exhalation rate depends on the emanation and transport of radon in the material.

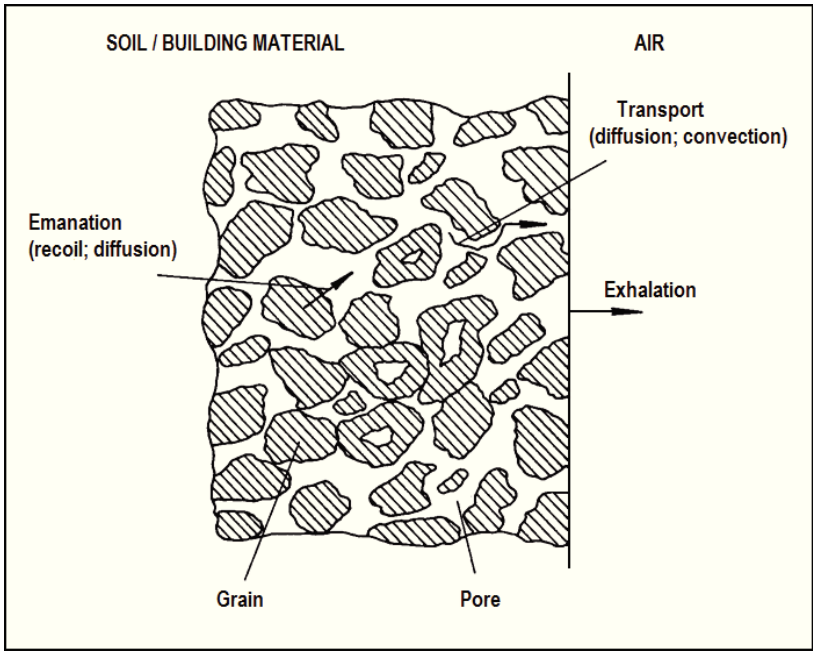

Figure 1.2 - Radon emanation from soil and building material

When radium decays in a mineral substance, the resulting radon atoms must first emanate from the grains into the air-filled pore space. The fraction of radon formed that enters the pores is commonly known as the *emanation fraction*, *emanation power* or *emanation coefficient*. The emanation fraction consists of two components: recoil and diffusion. Since the diffusion coefficient of gases in solid grain materials is very low, it is assumed that the main portion of the emanation fraction comes from the recoil process. Following the alpha decay of radium, radon atoms possess sufficient kinetic energy to move from the site of generation. The kinetic energy of the ^{222}Rn is about 86 keV. The range of ^{222}Rn is between 20 and 710 nm for common materials, 100 nm for water and 63 μm for air. The radon atom could be ejected from the grain as a result of the recoil, provided it was close to the surface, and was kicked in an outward direction. In the same way, the radon atom could be ejected to a micro-fissure in the mineral grain. Further transport in the micro-fissure is by diffusion. The recoil process inside the grain is shown in figure 1.3.

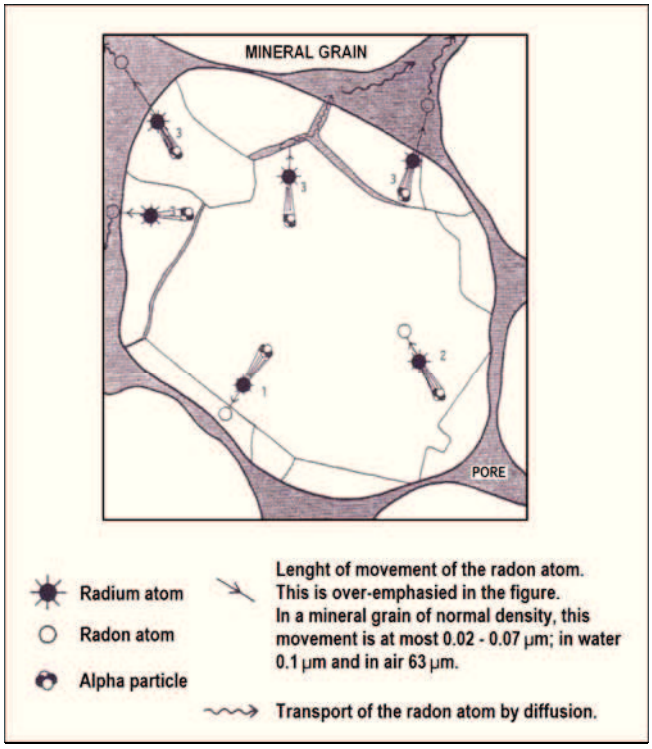

Figure 1.3 - Principles of radon emanation from a mineral grain. Case (1). When radium decays, a radium atom and an alpha particle are formed. The radon atom is moved into an adjacent crystal by a recoil effect from the ejected alpha particle. Case (2). The radon atom is moved through the crystal. Case (3). The radon atom is moved from the crystal to a micro-fissure or the air in an adjacent pore. It is assumed that further transport is by diffusion.

Although the emanation fraction can theoretically be assessed under some well-defined conditions, the results are generally much lower than the values of this parameter obtained experimentally. It is assumed that the large discrepancy between measured and calculated fractions is partly due to uneven distribution of radium, which could occupy places on or near the surface of the grains, and also partially due to radiation damage of the crystalline structure in the vicinity of the newly created radon atom.

The emanation fraction can be strongly affected by water content in the material. This impact of moisture is illustrated in figure 1.4 where relative changes of the emanation fraction are shown as a function of the water content in samples of uranium tailings.

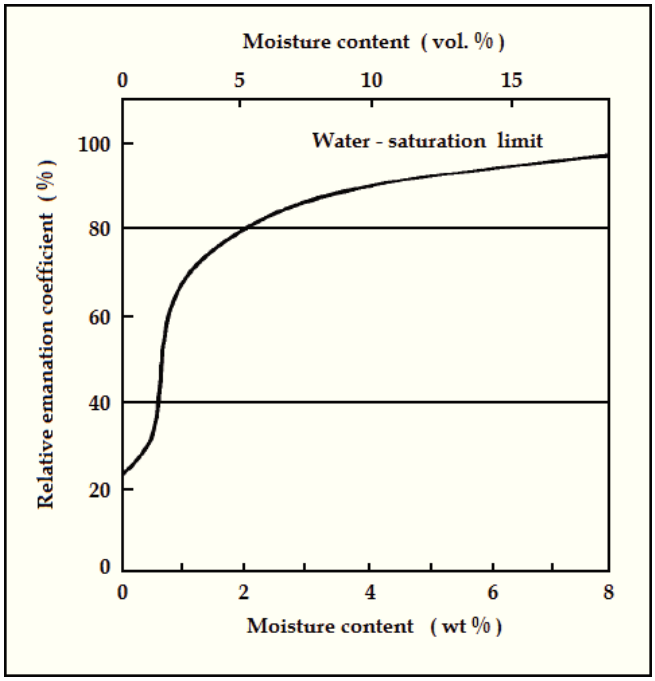

Figure 1.4 - The effect of water content on the ^{222}Rn emanation fraction

The emanation increases with increasing-soil moisture content, first quickly and later more slowly, in a way that can be considered almost constant in the normal range of soil moisture content (between 2% and saturation).

This increasing in the emanation fraction can be explained by the lower recoil range of radon atoms in water than in the air. If the pore space contains water, the ejected recoil most often will be brought to rest in liquid as sketched in the upper part of figure 1.5 and the radon atom is then free to diffuse from the water or be transported by it [Kigoshi, 1971]. If the interstitial space is dry (i.e. filled only with soil gas) and not wide enough to stop the recoiling radon, it enters a neighboring grain, apparently immobilizing itself as shown in the lower part of figure 1.5. It is, however, less isolated than if it failed to exit its grain of origin, the reason being that radiation damage extends to it from where it entered its new grain. This damage turns out to be etchable by exposure to water [Fleischer, 1980]. Hence, if the originally dry grains become wet before the radon has decayed, it can be released into the interstitial space.

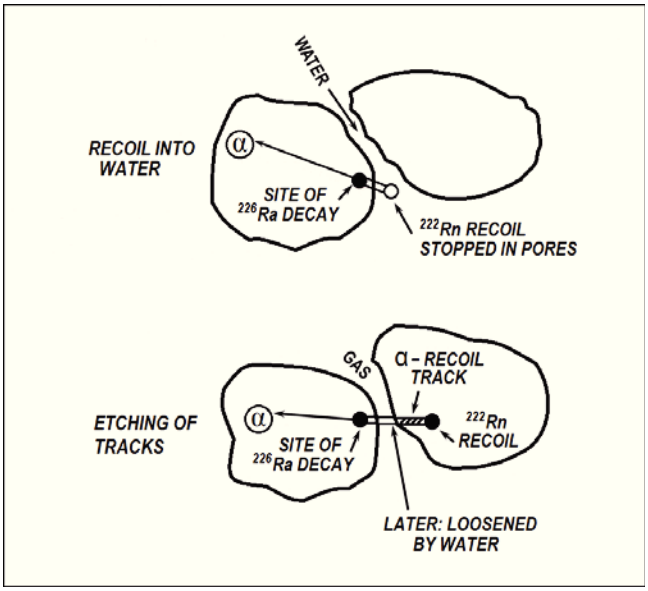

Figure 1.5 - Models of two radon-release mechanism: (top) the recoiling ^{222}Rn nucleus is stopped by water in the intergranular material; (bottom) the nucleus recoils into an adjacent grain and damage track is later removed chemically by the intergranular liquid, releasing the recoil nucleus.

In addition to the moisture effect, dependence of the emanation fraction on grain size and temperature has also been observed [Markkanen and Arvela, 1992]. Small grain size soils, such as clay, display maximum emanation at about 10%-15% water content. The ratio of the maximum emanation fraction to that of a dry sample also decreases as the grain size increases. A rise in temperature also causes an increase in the emanation fraction, which is probably due to the reduced adsorption of radon.

Different types of soil show different emanation fractions, which are generally about five times higher for ^{222}Rn (in the range 0.01 - 0.5) than ^{220}Rn (in the range $2 \cdot 10^{-4}$ - $6 \cdot 10^{-2}$). Measurements of the emanation fractions of various building materials revealed a slightly lower values than in soils, namely in the range of $2 \cdot 10^{-4}$ - $3 \cdot 10^{-2}$ for ^{222}Rn and from $2 \cdot 10^{-4}$ - $5 \cdot 10^{-2}$ for ^{220}Rn [Sabol and Weng, 1995].

Some emanated radon atoms, after their penetration through the material pores, may finally reach the surface before decaying. Radon gas and its movement in material follows some well-known physical laws. There are essentially two mechanisms of radon transport in material: molecular *diffusion* and forced *advection*.

In diffusive transport, radon flows in a direction opposite to that of the increasing concentration gradient. Fick's law describes the process. It is possible to derive the expression for the radon fluence rate in Bq m^{-2} s^{-1} for specified geometric conditions. Assuming the ground to be a porous mass of homogeneous material semi-infinite in extent, the radon fluence J_D emerging at the surface can be given as [UNSCEAR, 1988]:

$$J_D = C_{Ra}\,\lambda_{Rn}\,f\,\rho\left[\frac{D_e}{\lambda_{Rn}\,\varepsilon}\right]^{0.5} \tag{1.1}$$

where C_{Ra} is the activity concentration of ^{226}Ra in soil material (Bq kg^{-1}), λ_{Rn} is the decay constant of ^{222}Rn ($2.1 \cdot 10^6$ s^{-1}), f is the emanation fraction, ρ is the density (kg m^{-3}), D_e is the effective diffusion coefficient (m^2 s^{-1}) and ε is the porosity, all of these parameters referred to soil material.

A similar expression can be written for a building element, such as a wall or floor, considering it as a semi-infinite slab of porous material [Sabol and Weng, 1995]:

$$J_D = C_{Ra}\,\lambda_{Rn}\,f\,\rho\left[\frac{D_e}{\lambda_{Rn}\,\varepsilon}\right]^{0.5} \tanh d\left[\frac{D_e}{\lambda_{Rn}\,\varepsilon}\right]^{-0.5} \tag{1.2}$$

where d is the thickness (m) of the slab and the other symbols have the same meaning as in equation (1.1), but in this case the parameters refer to the building material. The expressions(1.1) and (1.2) are the same apart from the hyperbolic term in the second equation. This term takes into account the finite thickness of the considered slab and is always less than unity.

Since the main mechanism governing the entry of radon into the atmosphere from the surface of the earth is the diffusion, the radon fluence rate can be calculated by using appropriate parameters in equation (1.1). Representative values of these parameters and C_{Ra} = 40 Bq m^{-3} yield J_D = 0.026 Bq m^{-2} s^{-1} which is quite close to the average value experimentally obtained for some regions [Sabol and Weng, 1995].

The other mechanism affecting the movement of radon from the earth into a building is forced advection. In this case the movement of radon is caused by the slightly negative pressure differences (underpressure) that usually exist between the indoor and outdoor atmospheres. Underpressure inside a building can be created by two mechanisms: wind blowing on the building and heating inside the building. Some other factors such as changes in barometric pressure and negative pressure generated by mechanical ventilation, may sometimes also be important.

1.3 Theory of radon diffusion

Different models have been proposed to describe radon diffusion. In this section we will give a brief review of some of them.

1.3.1 Plate sheet model

One of the most reliable models to describe radon diffusion is the plane sheet model. The molecular diffusion is considered in one direction only and, for any stable element, can be described by Fick's second law [Gauthier et al., 1999]:

$$\frac{\partial C}{\partial t} = D\frac{\partial^2 C}{\partial z^2} \tag{1.3}$$

where C is the concentration of the element and D the diffusion coefficient along the *z-direction*. This equation admits a solution C(z, t) which is constrained by the initial and boundary conditions ($C = C_0$ at t = 0 and $-a < z < a$; C = 0 at $t > 0$ and z = +a):

$$C(z,t) = \frac{4C_0}{\pi}\sum_{n=0}^{\infty}\left\{\left(\frac{(-1)^n}{2n+1}\right)\cdot\cos\left(\frac{(2n+1)\pi\, z}{2a}\right)\cdot\left(\frac{-D(2n+1)^2\,\pi^2 t}{4a^2}\right)\right\} \tag{1.4}$$

where *a* is the half-width of the slab.

In order to take into account that radon is a radioactive gas, equation (1.3) has to be modified for radon by adding a production term from its parent ^{226}Ra and a decay term, which leads to:

$$\frac{\partial [Rn]}{\partial t} = \lambda_{Ra} [Ra] - \lambda_{Rn} [Rn] + D \frac{\partial^2 [\mathrm{Rn}]}{\partial z^2} \tag{1.5}$$

where brackets represent concentrations (in atoms · g^{-1}), λ_{Ra} and λ_{Rn} are the decay constants of ^{226}Ra and ^{222}Rn, respectively. Defining the function *K*(z, t) as:

$$K(z,t) = \left([Rn](z,t) - \left(\frac{\lambda_{Ra}}{\lambda_{Rn}} [Ra] \right) \right) \exp(\lambda_{Rn}\, t) \tag{1.6}$$

and introducing *K*(z, t) in equation (1.5), it yields:

$$\frac{\partial K}{\partial t} = D \frac{\partial^2 K}{\partial z^2} \tag{1.7}$$

which is the Fick's second law expressed for the function *K*(z, t). Nevertheless the solution of equation (1.7) cannot be merely obtained by combining the solution of the general Fick's second law (1.3) with the substitution (1.6) because the two functions *K*(z, t) and [Rn] (z, t) do not admit the same initial and boundary conditions. These conditions, for [Rn] (z, t), are:

$$[\mathrm{Rn}](z,0) = [Rn]_{eq} = \frac{\lambda_{Ra}}{\lambda_{Rn}} = [Ra] \qquad \text{for } -a < z < a, \quad t = 0$$

$$[\mathrm{Rn}](z,t) = 0 \qquad \text{for } z = -a, \quad z = a$$

(the atmosphere is considered as a reservoir of concentration C = 0) that means for *K*(z, t):

$$K(z,0)=0 \qquad \text{for } -a<z<a,\quad t=0$$
$$K(z,t)=-[Rn]_{eq}\exp(\lambda_{Rn}\,t) \qquad \text{for } z=-a,\quad z=a$$

Fick's law is usually solved for plane sheet geometry by separation of variables but this method is unsuccessful for such initial and boundary conditions. Several studies have been done for heat conduction in a slab having an initial zero temperature and surfaces maintained at the temperature $T(t) = V\,exp\,(vt)$ [Gauthier et al., 1999], obtaining:

$$\mathrm{K}(z,t)=-[Rn]_{eq}\exp(\lambda_{Rn}\,t)\frac{\cosh\left(z\sqrt{\frac{\lambda_{Rn}}{D}}\right)}{\cosh\left(a\sqrt{\frac{\lambda_{Rn}}{D}}\right)}+ \\ +\frac{4[Rn]_{eq}}{\pi}\sum_{n=0}^{\infty}\frac{(-1)^n\exp\left(\frac{-(2n+1)^2\,\pi^2\,Dt}{4a^2}\right)}{(2n+1)\left[1+\left(\frac{4\,\lambda_{Rn}\,a^2}{(2n+1)^2\,\pi^2\,D}\right)\right]}\cos\frac{(2n+1)\pi\,z}{2a} \tag{1.8}$$

and therefore, combining with (1.6):

$$[Rn](z,t)=[Rn]_{eq}-[Rn]_{eq}\ \frac{\cosh\left(z\sqrt{\frac{\lambda_{Rn}}{D}}\right)}{\cosh\left(a\sqrt{\frac{\lambda_{Rn}}{D}}\right)}+ \\ +\frac{4[Rn]_{eq}}{\pi}\sum_{n=0}^{\infty}\frac{(-1)^n\exp\left(-\left(\frac{(2n+1)^2\,\pi^2\,D}{4a^2}+\lambda_{Rn}\right)t\right)}{(2n+1)\left[1+\left(\frac{4\,\lambda_{Rn}\,a^2}{(2n+1)^2\,\pi^2\,D}\right)\right]}\cos\frac{(2n+1)\pi\,z}{2a} \tag{1.9}$$

By multiplying by λ_{Rn} both sides of the equation (1.9), we obtain the activity of *Rn (z, t):*

$$(Rn)(z,t)=(Ra)-(Ra)\frac{\cosh\left(z\sqrt{\frac{\lambda_{Rn}}{D}}\right)}{\cosh\left(a\sqrt{\frac{\lambda_{Rn}}{D}}\right)}+$$
$$+\frac{4(Ra)}{\pi}\sum_{n=0}^{\infty}\frac{(-1)^n\exp\left(-\left(\frac{(2n+1)^2\pi^2 D}{4a^2}+\lambda_{Rn}\right)t\right)}{(2n+1)\left[1+\left(\frac{4\lambda_{Rn}a^2}{(2n+1)^2\pi^2 D}\right)\right]}\cos\frac{(2n+1)\pi z}{2a} \quad (1.10)$$

where *(Rn)* and *(Ra)* represent the activity of ^{226}Ra and ^{222}Rn, respectively.

Knowing this function *Rn (z, t)* allows calculation of the radon concentration at each point of the slab for a given diffusion coefficient and at a given time. Figure 1.6 shows the diffusion profiles derived from the equation (1.10) for $0<z<a$ and compared with the solution obtained for a stable element (equation (1.4); Fig. 1.6a). Figures 1.6a and 1.6b present highly similar patterns for diffusion experiments shorter than 10^4 seconds, then the effect of ^{222}Rn radioactive ingrowth becomes more and more important, counterbalancing the effect of diffusion. In fact, a steady-state profile is reached, for which diffusion is exactly balanced by radon production from ^{226}Ra. Such steady-state profiles are governed by the following equation (Gauthier et al., 1999):

$$(Rn)(z,\infty)=(Ra)-(Ra)\frac{\cosh\left(z\sqrt{\frac{\lambda_{Rn}}{D}}\right)}{\cosh\left(a\sqrt{\frac{\lambda_{Rn}}{D}}\right)} \quad (1.11)$$

and strongly depend on $\zeta=a\sqrt{\lambda_{Rn}/D}$ (figure 1.6c). For low values of ζ ($\zeta<0.1$), the ^{222}Rn radioactive ingrowth is negligible and radon behaves like a stable element. On the other hand, for high values of ζ ($\zeta>50$), diffusion processes are too slow and balanced by ^{226}Ra decay, leading to very little, if any, radon depletion in the slab.

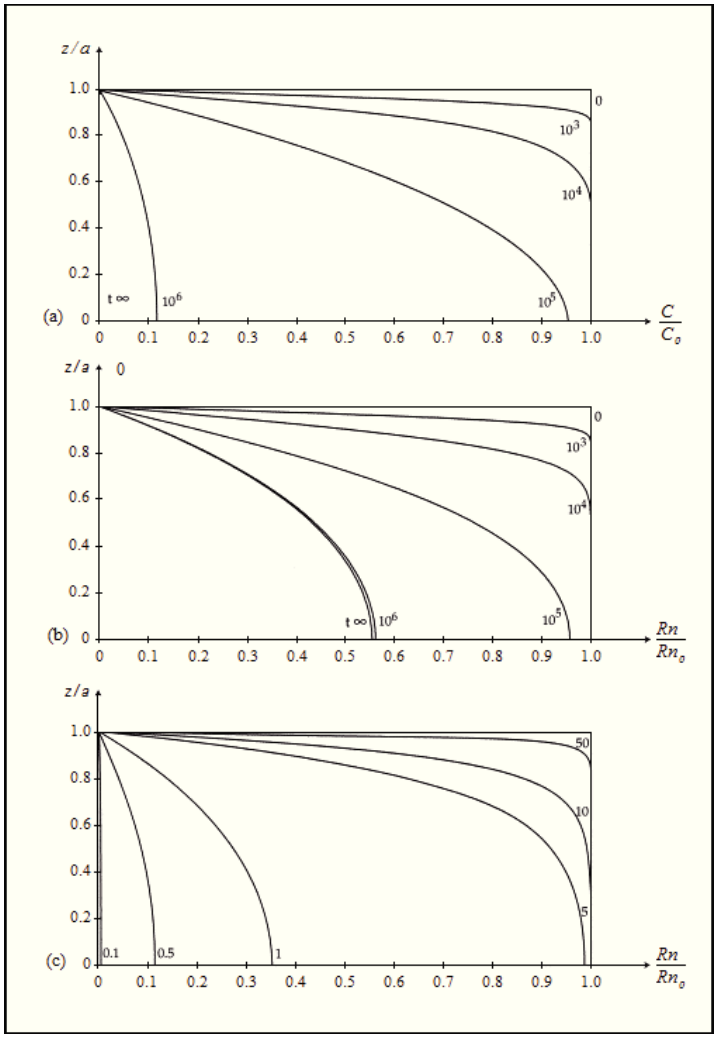

Figure 1.6 - Diffusion profiles in a half-slab stable element (a), and for radon (b, c). (a) Curves are drawn from equation (1.4) with a = 10^{-2} m and D = 10^{-10} m^2 s^{-1}. Values on the curves refer to the duration t (in seconds) of the diffusion process. When t tends towards infinity, the concentration C becomes zero in all the slab. (b) Curves are drawn from equation (1.10) with a = 10^{-2} m and D = 10^{-10} m^2 s^{-1}. After a sufficient time the system reaches a steady-state for which diffusion is exactly balanced by radioactive ingrowth. (c) Steady-state (t = ∞) diffusion profiles drawn from equation (1.11); numbers on diffusion curves refer to values of $\zeta = a\sqrt{\lambda_{Rn} / D}$.

The inverse problem for which radon concentration is known at a given t and z can also be considered and allows determination of the diffusion coefficient D. Such

an approach can be attempted by studying the bulk variation of radon concentration, expressed as a fractional loss f defined by (Gauthier et al., 1999):

$$f = \frac{N_i - N_t}{N_i} \tag{1.12}$$

where N_i is the initial number of radon atoms before heating and N_t the remaining number of radon atoms at the end of heating. N_i and N_t are obtained by integrating over the thickness the differential concentrations $\delta n = [Rn]\,(z, t)\,\rho S\,dz$, where ρ is the volumic mass of the melt and S the surface area of the slab. Thus, f is given by:

$$f = \frac{\int_{-a}^{a} [Rn](z,0)\,dz - \int_{-a}^{a} [Rn](z,t)\,dz}{\int_{-a}^{a} [Rn](z,0)\,dz} \tag{1.13}$$

After integration of (1.9), we obtain:

$$N_i = \int_{-a}^{a} \delta N = 2a\,\rho S\,[Rn]_{eq} \tag{1.14}$$

and:

$$\begin{aligned} N_t = {} & 2a\,\rho S\,[Rn]_{eq} - \frac{2\rho S\,[Rn]_{eq}}{\sqrt{\frac{\lambda_{Rn}}{D}}} \tanh a\sqrt{\frac{\lambda_{Rn}}{D}} + \\ & + \frac{16a\,\rho S\,[Rn]_{eq}}{\pi^2} \sum_{n=0}^{\infty} \frac{\exp\left(-\left(\frac{(2n+1)^2\,\pi^2\,D}{4a^2} + \lambda_{Rn}\right)t\right)}{(2n+1)^2 + \frac{4\lambda_{Rn}\,a^2}{\pi^2\,D}} \end{aligned} \tag{1.15}$$

Therefore, the fractional loss f can be written:

$$f = \frac{\tanh a\sqrt{\frac{\lambda_{Rn}}{D}}}{a\sqrt{\frac{\lambda_{Rn}}{D}}} - \frac{8}{\pi^2}\sum_{n=0}^{\infty}\frac{\exp\left(-\left(\frac{(2n+1)^2\,\pi^2\,D}{4a^2}+\lambda_{Rn}\right)t\right)}{(2n+1)^2+\frac{4\lambda_{Rn}\,a^2}{\pi^2\,D}} \tag{1.16}$$

This relation allows calculation of f at a given D and t, and also estimation of D once f, obtained from gamma-ray measurements, and t are known.

As shown in Figure 1.6c, the maximum ^{222}Rn loss obtained for infinite time of diffusion, depends on $\zeta = a\sqrt{\lambda_{Rn}/D}$ and tends toward 1/2 tanh ζ/ζ. For values of ζ ranging between 0.1 and 50, f varies from 18.9% to only 1%. For a given diffusion coefficient, the maximum fractional loss is directly constrained by the thickness of the slab.

1.3.2 Infinite source model

Let us consider an earth model in which a radon infinite source with concentration C_0 is overlain by an overburden of thickness *h*, which contains no radon sources. This model resembles the study area where measured radon production rate of the overburden is zero. In this case the radon transportation equation in the overburden can be written as [Wattananikorn et al., 1998]:

$$\frac{d^2C}{dz^2}+\frac{v}{D}\frac{dC}{dz}-\frac{\lambda}{D}=0 \tag{1.17}$$

where *C* is the radon concentration at any depth *z*, *v* is the gas flow velocity (positive upward), *D* is the diffusion coefficient of radon and λ is the decay constant. The solution of (1.17) is:

$$C = C_0 \exp\left[\frac{v(h-z)}{2D}\right] \frac{\sinh\left[\left(\sqrt{\left(\frac{v}{2D}\right)^2 + \frac{\lambda}{D}}\right) z\right]}{\sinh\left[\left(\sqrt{\left(\frac{v}{2D}\right)^2 + \frac{\lambda}{D}}\right) h\right]} \tag{1.18}$$

From (1.18), if the depth of the source h and the diffusion coefficient D are known, the value of flow velocity *v* may be found from the radon concentration C measured at two different depths. Figure 1.7 is a graph showing the relationship between the ratio of radon concentration at 50 cm and 100 cm depths ($C_{z=50}$ / $C_{z=100}$) versus an upward flow velocity *v* (in terms of $\sqrt{\lambda D}$), for the case of an earth model having h = 20 m and D = 0.036 cm^2/s.

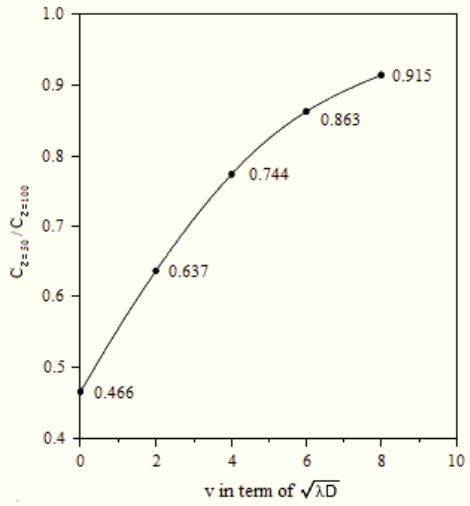

Figure 1.7 - Relation between the ratio of radon concentration at 50 and 100 cm depths, versus an upward flow velocity

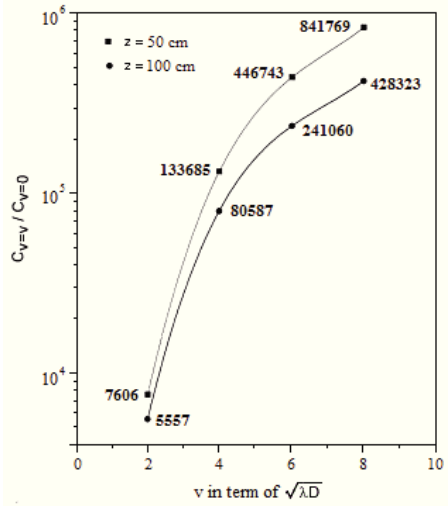

Figure 1.8 - Correlation between the ratio of radon concentration for flow rate velocities v and zero, versus an upward flow velocity v, in the case of 50 and 100 cm depths.

In any earthquake event the change in radon concentration in the overburden may be induced by the change in flow velocity *v*. However, the change in concentration C caused by flow velocity change depends on the depth of measurement. Figure 1.8

shows such correlation that is derived from (1.18) for the same earth model mentioned earlier. From the figure it is seen that the change in the value of *v* causes more change in radon concentration C at 50 cm than at 100 cm depth. This fact must be taken into consideration if deep hole radon measurement is used to reduce the near surface effects due to meteorological parameters.

1.3.3 Radon transport in dry, cracked soil

A model of radon transport in dry and cracked soil, proposed by *Holford et al.* [1993], starts from the diffusive flux density in soil (F_d), that is the mass of radon transported per unit time in bulk cross-sectional area of soil by molecular diffusion, defined by Fick's law for molecular diffusion:

$$F_{d_i} = - D_{ij} \frac{\partial (nC)}{\partial x_j} \tag{1.19}$$

where D_{ij} is the diffusion coefficient for radon in dry soil, i and j are subscripts indicating direction and are summed over the range i = 1, 2 and j = 1, 2, C is the concentration of radon gas in air, defined as the mass of radon per unit volume of air, n is the total porosity of the soil (ratio of the volume of void space to the total volume of soil), and nC is the mass of radon transported in dry soil per unit bulk volume of soil. The diffusion coefficient for radon in dry soil is defined as [Holford et al., 1993]:

$$D_{ij} = D_A \, \tau_{ij} \tag{1.20}$$

where D_A is the diffusion coefficient for radon in pure air and τ_{ij} is the coefficient of tortuosity of the soil. The diffusion of radon in pure air is calculated as a function of temperature and pressure, the tortuosity can be defined as the ratio of the straight-line distance between two points to the same points by way of the connected pores. The tortuosity is empirically determined to be between 0.01 and 0.66 for most soils.

The advective flux density (F_a), the mass of radon transported per unit time per unit bulk cross-sectional area of soil by air flow, is defined as:

$$F_{a_i} = v_i\, C \tag{1.21}$$

where v_i is the Darcy's velocity of soil air, which is defined as the volume of air flowing per unit bulk cross-sectional area of soil per unit of time in the direction i = 1, 2. Conservation of mass results in the following continuity equation:

$$-\frac{\partial (nC)}{\partial t} = \frac{\partial F_i}{\partial x_i} + \lambda\,(nC) - n\phi \tag{1.22}$$

where t is time, F_i is the total flux density, λ is the ^{222}Rn decay coefficient, and the source term, ϕ, is the production rate of radon per unit volume of soil pore space.

Substituting equations (1.19) and (1.21) into equation (1.22) and neglecting the effect of rock compressibility yields the governing equation for radon transport in dry soil:

$$\frac{\partial C}{\partial t} = \frac{\partial}{\partial x_i}\left(D_{ij}\,\frac{\partial C}{\partial x_j}\right) - \frac{\partial}{\partial x_i}\left(\frac{v_i}{n}\,C\right) - \lambda C + \phi \tag{1.23}$$

Cracks and holes are assumed to be perfectly dry, with a porosity of 1 and no production of radon. Therefore the radon transport in cracks can be described by:

$$\frac{\partial C}{\partial t} = \frac{\partial}{\partial x_i}\left(D_A\,\frac{\partial C}{\partial x_j}\right) - \frac{\partial}{\partial x_i}\left(v_i\, C\right) - \lambda C \tag{1.24}$$

Now, if we consider the airflow, radon transport and air flow are coupled by Darcy's law:

$$v_i = -\frac{k_{ij}}{\mu}\left(\frac{\partial P}{\partial x_j} + \rho g_j\right) \tag{1.25}$$

where v_i is the Darcy velocity, k_{ij} is the intrinsic permeability of the dry soil, μ is the dynamic viscosity of air at a given temperature, P is the absolute pressure, ρ is the density of air at a given temperature and g_j is the gravitational acceleration vector.

Conservation of mass requires that the change of fluid mass stored within a unit volume of soil equal the net rate of fluid flow into that volume. The resulting continuity equation takes the form [Bear, 1979]:

$$-\frac{\partial(n\rho)}{\partial t} = \frac{\partial(v_i\rho)}{\partial x_i} \tag{1.26}$$

Combining the continuity equation (1.26) and Darcy's law (1.25) gives:

$$\frac{\partial(n\rho)}{\partial t} = \frac{\partial}{\partial x_i}\left[\frac{k_{ij}}{\mu}\left(\frac{\partial P}{\partial x_j} + \rho g_j\right)\rho\right] \tag{1.27}$$

For an ideal gas, the equation of state is:

$$\rho = \frac{MP}{RT} \tag{1.28}$$

where M is the molecular weight, R is the universal gas constant and T is the absolute temperature. For isothermal flow, then:

$$\frac{\partial\rho}{\partial t} = \frac{M}{RT}\frac{\partial P}{\partial t} \tag{1.29}$$

Substituting equations (1.28) and (1.29) into (1.27) and assuming the effects of rock compressibility to be negligible gives an equation for isothermal air flow:

$$n\frac{\partial P}{\partial t}=\frac{\partial}{\partial x_i}\left(\frac{k_{ij}}{\mu}\frac{\partial P}{\partial x_j}P\right)+\frac{\partial}{\partial x_i}\left(\frac{k_{ij}}{\mu}\rho g_j P\right) \tag{1.30}$$

The permeability distribution is parabolic, with the maximum permeability at the center of the crack and an average vertical permeability of:

$$k_{C2}=\frac{w^2}{12} \tag{1.31}$$

where w is the width of the crack. The horizontal permeability in the crack, k_{C1}, is arbitrarily assigned a value several orders of magnitude larger than that of the soil.

The boundary conditions at the soil surface may vary in both space and time. The boundary conditions for the flow and transport equations for the two-dimensional soil model with cracks are shown in Figure 1.9.

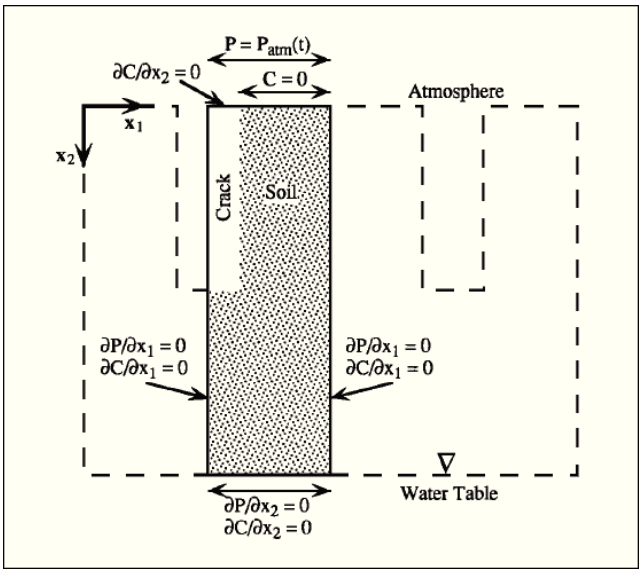

Figure 1.9 - Boundary conditions for a two-dimensional gas flow and radon transport simulation

At the top boundary, the atmospheric pressure is prescribed but varies with time. The concentration at the top of the soil is prescribed as zero, but the concentration at the

top of the crack is allowed to rise above zero by specifying no concentration gradient. Advective flux of radon occurs across the top cracks boundary if the velocity is not equal to zero. The left and right boundaries of the model are assumed to be axes of symmetry, at the center of the crack and at the midpoint between two cracks, respectively. The bottom boundary, at the water table, is considered to be impervious to flow and transport. The boundary conditions for the flow and transport equations for a one-dimensional soil model without cracks are exactly the same as those for the soil in the two-dimensional case.

Holford et al. [1993] have solved the governing equations for airflow and radon transport using the Galerkin finite element numerical method and a fully implicit time-weighting scheme. They compared radon transport calculations to a one-dimensional analytical solution of the advective-dispersion equation with radioactive decay and a linear source term. If the concentration is zero at the surface, the surface flux density is given by:

$$F(z=0)=\frac{\phi}{2}\left[\frac{v}{2}+\left(\frac{v^2}{4}+n^2\lambda D\right)^{1/2}\right] \tag{1.32}$$

while the concentration as a function of depth is given by:

$$C=\frac{\phi}{2}\left\{1-\exp\left[z\left[\frac{v}{2nD}+\left(\left(\frac{v}{2nD}\right)^2+\frac{\lambda}{D}\right)^{1/2}\right]\right]\right\} \tag{1.33}$$

1.3.4 Radon transport in unsaturated soil

A radon transport model in unsaturated soil was proposed by *Chen et al.* [1995]. They started with the consideration that transient movement of soil radon to the atmosphere through the shallow subsurface can be considered as a process of volatilization and that, in general, transport of chemicals from soil into atmosphere is

complicated and difficult to predict because of the many parameters affecting sorption, motion, and persistence of gaseous and highly volatile compounds. Mechanism and factor affecting volatilization of chemicals from soil can be group into three categories: (1) those that affect the equilibrium process within the soil, (2) those that affect gas transport through the soil profile to the soil surface, and (3) those that affect the mechanism of chemical release in gas phase from the unsaturated soil to the atmosphere, as described by *Spencer et al.* [1990]. Volatilization can dominate the transport of highly volatile species from shallow unsaturated soil into the general environment as well as the efficiency of field application and disposal [Taylor et al., 1990]. In general, however, transport involves sorption on soil particles, movement to the soil surface and dispersal into the atmosphere.

The factors that affect gas equilibrium within soil are vapor pressures or vapor density, aqueous solubility, sorption, transformation and degradation (or decay for radon). The interaction of gas-phase chemicals with the liquid phase can be described by Henry's constant, which governs equilibrium vapor pressure or vapor density, and Fick's law, which describes diffusive flux rates through the media with which the gas interacts [Alzaydi et al., 1978; Thorstenson et al., 1989; Falta et al., 1989; Gierke et al., 1990].

Soil properties, such as size distribution of soil particles and organic matter, affect transformation and degradation of chemicals [Brusseau, 1991] and emanation rates of radon [Tanner 1980, 1988; Schery et al., 1984; Nilson et al., 1991]. These factors can be described and incorporate in a general convection-diffusion equation. All of these are, however, also dependent on soil water content, characteristics of chemicals, chemical concentration and soil properties and, hence, time variations of these soil properties must also be included in the convection-diffusion equation. The sorption processes that involve radon are physical adsorption on solids and equilibrium solubility in liquids.

Factors that affect gas transport through the soil profile to the soil surface, in addition to those previously mentioned, are soil air permeability, which is closely

related to the soil structure and water content, and concentration and distribution of the chemical in the soil column.

The factors that affect mechanism of chemical release in gas phase from the unsaturated soil to the atmosphere are controlled by soil water content, barometric pressure and soil temperature [Tanner, 1980, 1988; Schery et al., 1984; Nilson et al., 1991; Thomas et al., 1992]. Many investigations have been done using radon and other gasses as tracers in the natural environment, and their results have shown that soil pores are the pathway of gas-phase transport but soil water content controls pore space: when soil water content increases, gas transport decreases. This is, however, a nonlinear response because saturation and drainage of soil pores and accumulation and ventilation of radon from the soil pores are not time-reversible processes [Tanner, 1980, 1988; Schery et al., 1984; Goh et al., 1991; Thomas et al., 1992]. Because the soil gas phase is highly mobile, atmospheric factors such as barometric pressure changes can have a strong impact on gas-phase transport in the field. Relatively small changes of barometric pressure can result in advective gas fluxes which are much larger than diffusive gas fluxes [Thorstenson et al., 1989; Massman, 1989]. Barometric pressure changes usually have an inverse influence on the movement of soil gases to the atmosphere: when barometric pressure decreases, gas flux from soil to the atmosphere increases because of the air-pumping process; increasing pressures tend to force atmospheric air into the soil and, to some extent, counteract the diffusion gradient [Tanner, 1980, 1988; Schery et al., 1984; Goh et al., 1991; Washington et al., 1992]. Because soil has a low thermal conductivity, it strongly attenuates short-period variations of air temperature with increasing depth; hence thermally dependent volatilization responds most strongly to large variations of air temperature or to seasonal changes [Goh et al., 1991; Washington et al., 1992]. The influence of wind speed on transport through unsaturated soil is still not well understood.

Starting from these considerations, *Chen et al.* [1995] have proposed a model to simulate transport of radon through unsaturated soil considering environmental parameters such as air temperature changes and air flow driven by barometric pressure changes. They started from a convection-diffusion equation:

$$\frac{\partial C_T}{\partial t} = -\frac{\partial J_T}{\partial z} + \Phi \tag{1.34}$$

where t is the time (in days), z is the depth (in meters), Φ represents unspecified source or sinks of solute such as emanation and decay of soil radon and C_T is the total solute concentration in all phases (liquid, gas, sorbed). C_T is defined as:

$$\begin{aligned} C_T &= \rho_B C_S + \theta C_L + nC_G \\ &= \rho_B K_D C_L + \theta C_L + nK_H^* C_L \\ &= C_L \left(\rho_B K_D + \theta + nK_H^*\right) \end{aligned} \tag{1.35}$$

where C_L is the concentration in solution (in g m^{-3}), C_S is the concentration of chemical in the sorbed phase (in mg kg^{-1} of dry sand) ($C_S = K_D \times C_L$), C_G is the concentration in gas phase (in grams per cubic meter) ($C_G = K^*_H \times C_L$), ρ_B is the soil bulk density (in kg m^{-3}), K_D is a partition or distribution coefficient (in m^3 kg^{-1}), θ is the volumetric water content (dimensionless), n is the air-filled porosity, K^*_H is a modified Henry's law constant, defined as the saturated vapor density (C^*_G) of the compound divided by the aqueous solubility (C^*_L), both in units of mass per volume. In addition, $K_D = K_{OC} \times f_{OC}$, where K_{OC} is an organic carbon partition coefficient (in m^3 kg^{-1}) and f_{OC} is the organic carbon fraction of soil (dimension-less). J_T is the total solute flux density (in mg m^{-2} d^{-1}) and can be expressed as (for soil radon, the unit of flux density will be Bq m^{-2} s^{-1}):

$$J_T = J_{DL} + J_{CL} + J_{DG} + J_{AG} \tag{1.36}$$

where J_{DL} is the diffusion flux density in the liquid phase (in mg m^{-2} d^{-1}), J_{CL} is the convection flux density in the gas phase (in mg m^{-2} d^{-1}), J_{DG} is the diffusion flux density in the gas phase (in mg m^{-2} d^{-1}) and J_{AG} is the advection flux density in the gas phase (in mg m^{-2} d^{-1}). *Chen et al.* [1995] assumed that air in soil is stagnant and

the advection component of transport is approximated by adding an enhancement factor in the diffusion flux of the gas phase. The total solute flux is represented by:

$$\begin{aligned} J_S &= J_{DL} + J_{CL} + J_{DG} \\ &= -\theta\, D(\theta, q)\frac{dC_L}{dz} + qC_L \end{aligned} \tag{1.37}$$

where $D(\theta, q)$ is the apparent diffusion coefficient (in $mm^2\ d^{-1}$) that includes a description of the effects upon solute movement of mechanical dispersion and both aqueous and gas phase chemical diffusion and is defined as:

$$D(\theta, q) = \frac{D_P(\theta)}{\theta} + D_M(q) + D_{OG}\frac{K_H^*}{\theta} \tag{1.38}$$

where q is the water flux density (in $m\ d^{-1}$), $D_P(\theta)$ is the efficiency diffusion coefficient in liquid phase (in $m^2\ d^{-1}$) and it can be estimated by:

$$D_P(\theta) = D_{OL}\,\alpha\, e^{(\beta\theta)} \tag{1.39}$$

where D_{OL} is the diffusion coefficient in a pure liquid phase (in $m^2\ d^{-1}$), α and β are empirical constants, reported to be $0.005 < \alpha < 0.01$ and $\beta \approx 10$ [Olsen et al., 1968], DM(q) is the mechanical dispersion coefficient that de-scribes mixing of liquid phase between large and small pores as a result of local variations in mean water flow velocity (in square meters per day) and can be estimated by:

$$D_M(q) = \lambda\left|\frac{q}{\theta}\right| \tag{1.40}$$

where λ is the dispersivity with a range of about 2-80 mm. $D_{OG}(n)$ is the diffusion coefficient for the vapor through the gas-filled porosity (in $m^2\ d^{-1}$) and can be estimated by:

$$D_{OG}(n) = D_{OT}(n) + D_{BARO} \tag{1.41}$$

where D_O is the diffusion coefficient in air (outside the porous media) (in $m^2\ d^{-1}$) and D_{BARO} (in $m^2\ d^{-1}$) is the enhancement factor for barometric effects on gas advection as mentioned above. *T(n)* is the dimensionless Millington and Quirk tortuosity factor given by [Jury et al., 1983]:

$$T(n) = n^{\frac{3.333}{\theta_S^2}} \tag{1.42}$$

For nonvolatile and low-volatile gas advection of air flow through soil may be negligible. Radon gas is, however, treated as a highly volatile chemical. Changes of barometric pressures, causing air flow and resulting in gas advection, play an important role in chemical transport.

Commonly, gas advection J_{AG} (in mm $m^{-2}\ d^{-1}$) is equal to $q_a \times C_G$, where C_G is the gas concentration (in $g\ m^{-3}$) and q_a is the air flux through soil (in $m\ d^{-1}$). Barometric pressure change is the driving force to cause air flow in soil. Adopting the derivation of the Richards equation for the water flow [Massmann, 1989], the air flow can be described by:

$$\frac{\partial(n\rho_a)}{\partial t} = -\frac{\partial(q_a\rho_a)}{\partial z} = \frac{\partial}{\partial z}\left(\frac{K_a}{g}\frac{\partial P_T}{\partial z}\right) \tag{1.43}$$

where ρ_a is the air density (in $kg\ m^{-3}$), K_a is the soil air conductivity (in $m\ d^{-1}$), $P_T = P + \rho_a g z$ is the total air pressure, P is the barometric (atmosphere) pressure (10^2 Pa), z here is the depth (in m) and g is the gravitational acceleration. The air filled porosity, $n = \theta_S - \theta$, here is a constant and can be obtained from the calculation of water content, θ, by the Richards equation. For an ideal gas we have a relationship:

$$\rho_a = \frac{MP}{RT} \tag{1.44}$$

where M is the molecular weight, R is the gas constant and T is the temperature (in kelvins). In addition, the model applies the *Campbell* [1974] formula to describe the relationship between the soil hydraulic conductivity K_w (in m d^{-1}) and water content θ as:

$$K_w = K_{ws}\left(\frac{\theta}{\theta_s}\right)^{2b+3} \tag{1.45}$$

where K_{ws} is the saturated hydraulic conductivity and b is a constant. K_{ws} also can be approximated by the intrinsic permeability k (in cm^2),

$$K_{ws} = k\, g\, \frac{\rho_w}{\mu_w} \tag{1.46}$$

where μ_w is the water dynamic viscosity (in g s^{-1} cm^{-1}), and ρ_w is the water density (in kg m^{-3}). Because the intrinsic permeability is independent from fluid properties, the dry-soil air conductivity K_{ad} can be expressed from (1.46):

$$\begin{aligned} K_{ad} &= \frac{k\, g\, \rho_a}{\mu_a} \\ &= K_{ws}\frac{v_w\, \rho_a}{\mu_a} \end{aligned} \tag{1.47}$$

where μ_a is the air dynamic viscosity (in g s^{-1} cm^{-1}), and $v_w = \mu_w / \rho_w$ is the kinematic viscosity (in cm^2 s^{-1}). Assuming that the relationship between the air-filled porosity n and the soil air conductivity K_a is:

$$K_a = K_{ad}\left(\frac{n}{\theta_s}\right)^{\frac{1}{2b+3}} \tag{1.48}$$

combining (1.46), (1.47) and (1.48) with (1.43) gives:

$$n\frac{\partial P}{\partial t}=\frac{\partial}{\partial z}\left[\frac{K_{ws}\,v_w}{\mu_a\,\mathrm{g}}\left(\frac{n}{\theta_s}\right)^{\frac{1}{2b+3}}P\frac{\partial P}{\partial z}\right] \tag{1.49}$$

which can be solved numerically. Surface and bottom boundary conditions are based on simulation conditions and site characteristics.

The advective gas flux density is:

$$q_a\,C_G=q_a\,K_H^*\,C_L \tag{1.50}$$

which is expressed in terms of concentration in the liquid phase, is added to (1.37) with the resulting solute flux equation:

$$J_s=-\theta\,D(\theta,q)\frac{dC_L}{dz}+q_w\,C_L+q_a\,K_H^*\,C_L \tag{1.51}$$

and a new numerical calculation. Because (1.49) for air flow is a nonlinear differential equation and is not very stable for numerical convergence, a numeric smoothing technique and small time steps are used to reach convergence and mass balance. This approach is especially important when the concentration of the volatile species is low and the barometric pressure change is large. In addition, some computational problems are avoided by expressing barometric pressure changes relative to a standard pressure rather than in absolute terms.

Chapter 2

Radon transport in porous materials: RnMod3d Model

In this chapter, the radon transport in isotropic porous materials, will be discussed in the framework of *RnMod3d* model derived by *Andersen* [1992]. The description is made for a three-phase system, i.e. for a porous medium containing solid, liquid and gas phase. Although most experiments with the radon vessel were performed with low-moisture materials, this approach is chosen because the equations for dry porous media form a subset of the more complex description for a three-phase system. Similar descriptions for multi-phase radon transport have been used by *Rogers and Nielson* [1991, 1993] and *van der Spoel et al.* [1997]. An outline of the finite-volume approach is also given.

2.1 Basic definitions

Consider a reference element δV of soil. This volume may be split into three parts: δV_g for the volume of grains, δV_w for the volume of water, and δV_a for the volume of air:

$$\delta V = \delta V_g + \delta V_w + \delta V_a \tag{2.1}$$

Hence the (total) porosity ε, the water porosity ε_w, and the air porosity ε_a can be expressed as:

$$\varepsilon = \frac{\delta V_w + \delta V_a}{\delta V_a} \tag{2.2}$$

$$\varepsilon_w = \frac{\delta V_w}{\delta V} \tag{2.3}$$

$$\varepsilon_a = \frac{\delta V_a}{\delta V} \tag{2.4}$$

We define the fraction of water saturation of the pore volume (i.e. the volumetric water content) as:

$$\theta_V = \frac{\delta V_w}{\delta V_a + \delta V_w} = \frac{\varepsilon_w}{\varepsilon} \tag{2.5}$$

Hence $\theta_V = 1$ means that the pores are completely filled with water, whereas $\theta_V = 0$ means that the soil is dry. The total mass of the reference element is:

$$\delta M = \delta M_g + \delta M_w \tag{2.6}$$

where δM_g is the mass of grain material and δM_w is the mass of water. The mass of pore air is neglected. The density of the grain material is:

$$\rho_g = \frac{\delta M_g}{\delta V_g} \tag{2.7}$$

For different types of soils ρ_g is in the (narrow) range from 2.65 to 2.75 · 10^3 kg m^{-3}. The density for water:

$$\rho_w = \frac{\delta M_w}{\delta V_w} \tag{2.8}$$

is about 1.0 · 10^3 kg m^{-3}. The wet-soil density for given porosity and water content can be calculated as:

$$\rho_{ws} = \frac{\delta M}{\delta V} = (1-\varepsilon)\,\rho_g + \theta_V\ \rho_w \tag{2.9}$$

The dry-soil density is:

$$\rho_{ds} = \frac{\delta M_g}{\delta V} = (1-\varepsilon)\,\rho_g \tag{2.10}$$

We define the amount of water per dry mass of soil (i.e. the gravimetric water content) as:

$$\theta_g = \frac{\delta M_w}{\delta M_g} = \frac{\rho_w\,\delta V_w}{\rho_g\,\delta V_g} = \frac{\varepsilon_w}{1-\varepsilon}\,\frac{\rho_w}{\rho_{ds}} = \frac{\varepsilon}{1-\varepsilon}\,\frac{\rho_w}{\rho_{ds}}\,\theta_V \tag{2.11}$$

Hence if the porosity of the soil is ε = 0.3, then full water saturation (θ_V = 100%) means that the amount of water per dry mass is normally about θ_g = 16%.

2.2 Radon transport equation

The total activity δA of ^{222}Rn (simply referred to as “radon” in all the following) in the reference element δV may be split into three parts:

$$\delta A = \delta A_g + \delta A_w + \delta A_a \tag{2.12}$$

where the indices have the same meaning as in the equation (2.1). We now define the concentration of radon in the air-filled parts of the pores as:

$$c_a = \frac{\delta A_a}{\delta V_a} \tag{2.13}$$

and the radon concentration in the water-filled parts of the pores as:

$$c_w = \frac{\delta A_w}{\delta V_w} \tag{2.14}$$

Part of the grain activity δA_g is available for transport in the pore system. This is the radon adsorbed to soil-grain surfaces: $\delta A_{g,s}$. The immobile part (δA_g - $\delta A_{g,s}$) is radon produced by the "non-emanating" part of the grain radium. In line with the framework presented by *Rogers and Nielson* [1991], we introduce the sorbed radon concentration per kg dry mass (Bq kg^{-1}) as:

$$c_s = \frac{\delta A_{g,s}}{\delta M_g} \tag{2.15}$$

where δM_g is the grain mass within δV.

We assume rapid sorption kinetics [Wong et al., 1992] such that the partitioning of radon between air, water and soil grains is permanently in equilibrium at any point of the soil:

$$c_w = L\, c_a \tag{2.16}$$

$$c_s = K\, c_a \tag{2.17}$$

where L is the Ostwald partitioning coefficient given in table 2.1 and K is the radon surface sorption coefficient [Rogers and Nielson, 1991; Nazaroff, 1992]. The equilibrium assumption simplify the problem considerably, then we can express the total mobile radon activity by referring to the concentration in just one phase. Normally, the radon concentration in the air phase c_a is selected as "reference concentration". This approach is also used in *RnMod3d*. The mobile activity in δV is hence given as:

$$\delta A_{g,s} + \delta A_w + \delta A_a = \beta\, c_a\, \delta V \tag{2.18}$$

where

$$\beta = \varepsilon_a + L\,\varepsilon_w + K\,\rho_{d,s} \tag{2.19}$$

is sometimes called the partition-corrected porosity. If the medium is dry and without grain sorption, we have $\beta = \varepsilon$. The equilibrium assumption is widely used in models of pollutant transport, but is not universally correct [Thomson et al., 1997]. Support for the assumption can be found in [Nazaroff et al., 1988; Nazaroff, 1992].

If radium is present only in soil grains, we define the radon generation rate per pore volume (Bq s^{-1} per m^3-pore) as:

$$G = \frac{\lambda\,\rho_{ds}\,E}{\varepsilon} = \lambda E\,\frac{1-\varepsilon}{\varepsilon}\,\rho_g \tag{2.20}$$

where λ is the decay constant of radon ($2.09838 \cdot 10^{-6}$ s^{-1}), and E is the emanation rate of radon to the soil pores (i.e. the number of atoms that emanates into water and air per second per kg dry mass). We can write the emanation rate as $E = f\,A_{Ra}$, where f is the fraction of emanation and A_{Ra} is the activity concentration (Bq kg^{-1}) of ^{226}Ra per dry mass.

Table 2.1 - Radon solubility L in water as function of temperature [Clever, 1979]

Temperature K	*L* -
273.15	0.5249
278.15	0.4286
283.15	0.3565
288.15	0.3016
293.15	0.2593
298.15	0.2263
303.15	0.2003
308.15	0.1797

A mass conservation equation for the mobile radon activity in δV is:

$$\frac{\partial \beta c_a}{\partial t} = \varepsilon G - \lambda \beta c_a - \nabla \cdot \vec{j} \tag{2.21}$$

where $\vec{j}$ is the bulk flux density (in units of Bq s^{-1} per m^2) at time *t*. With the term 'bulk' we means that the density is measured per total cross-sectional area perpendicular to $\vec{j}$. Hence, a flux *J* (Bq s^{-1}) across some plane with geometric area *A* and uniform bulk flux density $\vec{j}$ gives $J = \vec{j} \cdot A\hat{a}$, where $\hat{a}$ is a unit vector perpendicular to the plane.

The bulk flux density consists of two, advective and diffusive, components:

$$\vec{j} = \vec{j}_a + \vec{j}_d \tag{2.22}$$

Neglecting water movement, the advective flux density is given by:

$$\vec{j}_a = c_a \vec{q} \tag{2.23}$$

where $\vec{q}$ is the bulk flux density of soil gas (in units of m^3 s^{-1} per m^2) discussed later. We assume that the diffusive flux can be written as:

$$\vec{j}_d = -D \nabla c_a \tag{2.24}$$

such that the bulk diffusivity accounts for radon diffusion through air and water in the pores. *D* is a function of temperature and pressure [Washington et al., 1994] and may therefore change in time and space. We assume that the soil-gas flow is so low that mechanical dispersion can be ignored (i.e. *D* is independent of $\vec{q}$) [Domenico et al., 1992]. In box 2.1 a summary of the *RnMod3d* equations for radon transport is drawn.

RnMod3d solves the following equation for radon transport:

$$\frac{\partial \beta c_a}{\partial t} = \varepsilon G - \lambda \beta c_a - \nabla \cdot \vec{j} \tag{2.25}$$

where

$$\vec{j} = c_a \, \vec{q} - D \nabla c_a \tag{2.26}$$

is the bulk flux density of radon (in Bq s^{-1} per m^2), and where

c_a is the radon concentration in the air-filled parts of the pores (Bq m^{-3})

t is the time (s)

$\beta = \varepsilon_a + L \, \varepsilon_w + K \, \rho_{d,s}$ is the partition-corrected porosity (dimensionless)

ε is the porosity (dimensionless)

G is the radon generation rate per pore volume (Bq s^{-1} per m^3)

λ is the decay constant for radon ($2.09838 \cdot 10^{-6}$ s^{-1} for ^{222}Rn)

D is the bulk diffusivity (m^2 s^{-1})

$\vec{q}$ is a known bulk flux density of soil gas (m^3 s^{-1} per m^2)

Box 2.1 - Radon transport equations

2.3 Soil-gas transport equation

It is assumed that the flow is of the Darcy type, that the soil has a uniform temperature (natural convection in the soil is ignored), and that ε_a is constant in time. Also, it is assumed that pressure variations are small in comparison with the absolute pressure. The equation can be derived as given next.

The equation of continuity for soil gas transport is [Bird et al., 1960]:

$$\frac{\partial \varepsilon_a \rho_a}{\partial t} = -\nabla \cdot (\rho_a \, \vec{q}) \tag{2.27}$$

where $\vec{q}$ is given by Darcy's law:

$$\vec{q} = -\frac{k}{\mu}\nabla p \tag{2.28}$$

and where ρ_a is the density of the gas (in kg m^{-3}). For an ideal gas under isothermal conditions, ρ_a is proportional to the absolute pressure *P(x, y, z, t)* (in Pa). Hence, we have:

$$\frac{\partial \varepsilon_a P}{\partial t} = -\nabla \cdot (P\,\vec{q}) \tag{2.29}$$

We can split the absolute pressure into three parts:

$$P(x, y, z, t) = P_0 - \rho_{a,0}\, g\, z + p(x, y, z, t) \tag{2.30}$$

where P_0 is the mean pressure at the atmospheric surface, and where p is the disturbance pressure field. The "aerostatic" pressure P_H at depth $-z$ below the atmospheric surface (located at $z = 0$, the z-axis pointing upwards) is:

$$P_H(z) = P_0 - \rho_{a,0}\, g\, z \tag{2.31}$$

where $\rho_{a,0}$ is the average air density at a given temperature (~ 1.3 kg m^{-3}). Thus P_H increases of about 13 Pa per m depth.

The left-hand side of equation (2.28) can be evaluated as follows:

$$\frac{\partial \varepsilon_a P}{\partial t} = \frac{\partial \varepsilon_a \left(P_H(z) + p(x, y, z, t)\right)}{\partial t} \tag{2.32}$$

$$= P_H(z)\frac{\partial \varepsilon_a}{\partial t} + \frac{\partial \varepsilon_a p}{\partial t} \tag{2.33}$$

We limit the treatment to the situation when ε_a is constant in time, and we therefore have:

$$\frac{\partial \varepsilon_a P}{\partial t} = \frac{\partial \varepsilon_a p}{\partial t} \tag{2.34}$$

On the right-hand side of equation (2.29), we assume that the disturbance pressure is small in comparison with $P_H(z)$ such that:

$$P\,\vec{q} = (P_H(z) + p)\,\vec{q} \tag{2.35}$$

$$\approx P_H\,\vec{q} \tag{2.36}$$

From this, we can approximate equation (2.29) as:

$$\frac{\partial \varepsilon_a P}{\partial t} = -\nabla \cdot (P_0\,\vec{q}) \tag{2.37}$$

or

$$\frac{\varepsilon_a}{P_0}\frac{\partial P}{\partial t} = -\nabla \cdot \vec{q} \tag{2.38}$$

In the special case of homogeneous soil, we can reduce equation (2.37) and (2.28) to:

$$\frac{\partial P}{\partial t} = D_p\,\nabla^2 p \tag{2.39}$$

which is a usual diffusion equation, where:

$$D_p = \frac{k\,P_0}{\mu\,\varepsilon_a} \tag{2.40}$$

is the diffusivity. We observe, that without the important simplification in equation (2.36) we would have obtained a transport equation with the term $\nabla^2 p^2$. Instead, only $\nabla^2 p$ is part of the final equation. Hence, equation (2.35) has lead to a linearization of the problem.

In box 2.2 a summary of the *RnMod3d* equations for soil-gas transport is drawn.

RnMod3d solves the linearized equation for soil-gas transport:

$$\frac{\varepsilon_a}{P_0}\frac{\partial P}{\partial t} = -\nabla \cdot \vec{q} \tag{2.41}$$

where

$$\vec{q} = -\frac{k}{\mu}\nabla p \tag{2.42}$$

is the bulk flux density of soil gas (in $m^3\ s^{-1}$ per m^2), and where

p is the disturbance pressure (Pa)

t is the time (s)

$\beta = \varepsilon_a + L\,\varepsilon_w + K\,\rho_{d,s}$ is the partition-corrected porosity (dimensionless)

ε_a is the air porosity (dimensionless)

P_0 is the mean absolute pressure (about 10^5 Pa)

k is the gas permeability (m^2)

μ is the dynamic viscosity (about $17.5 \cdot 10^{-6}$ Pa s at 10 °C)

Box 2.2 - Soil-gas transport equations

2.4 RnMod3d treatment of radon and soil gas

RnMod3d is programmed to solve equations (2.25) and (2.26) in box 2.1 and the formalism used to define problems in RnMod3d closely follows that used in these equations. For the soil-gas problem, the situation is a bit more complicated. First, we observe that equations (2.41) and (2.42) in box 2.2 are also of the form given in equations (2.25) and (2.26). We just have to substitute c_a with p, D with k/μ and β with ε_a/P_0. The rest of the "radon-equation coefficients" must be set to zero: $\lambda = 0$, $G = 0$, $\varepsilon = 0$ and $\vec{q} = 0$. If we do that, RnMod3d solves the soil-gas problem as defined by equations (2.41) and (2.42).

Table 2.2 should ease the translation of quantities used in RnMod3d and the two sets of transport equations.

Table 2.2 - Quantities used by Rnmod3d in the radon and soil-gas transport problem.

RnMod3d	Radon problem Equations (2.39) and (2.40)		Soil-gas problem Equations (2.41) and (2.42)	
Basic field value	c_a	[Bq m^{-3}]	p	[Pa]
`D_def`	D	[m^2 s^{-1}]	$\frac{k}{\mu}$	[m^2 Pa^{-1} s^{-1}]
`e_def`	ε	[-]	0	
`beta_def`	β	[-]	$\frac{\varepsilon_a}{P_0}$	[Pa^{-1}]
`G_def`	G	[Bq s^{-1} m^{-3}]	0	
`lambda_def`	λ	[s^{-1}]	0	
`flowfield`	`import`		`export`	
`J`	$\int_\Omega \vec{j} \cdot d\vec{a}$	[Bq s^{-1}]	$\int_\Omega \vec{q} \cdot d\vec{a}$	[m^3 s^{-1}]
`Q`	$\int_\Omega \vec{q} \cdot d\vec{a}$	[m^3 s^{-1}]	0	

The first line of the table concerns the "field values" used by RnMod3d. For radon problems, these field values represent the radon concentration in the air-filled pore parts (c_a). For soil-gas problems, they correspond to the disturbance pressure (p). therefore these quantities should be used when specifying fixed-value boundary conditions. Furthermore, it should be observed that model output of field values are based on these quantities.

The next lines concern control variables `D_def` to `lambda_def`. These control variables are Pascal pointers to user-defined functions. Here we just state that their meaning relates directly to the coefficients of equations (2.25) and (2.26). Hence, for radon problems, `D_def` should point to the user-defined function where the bulk diffusivity D of the material is defined and `e_def` should point to the user-defined function of (total) porosity. For soil-gas problems, the situation is different as already stated: `D_def` should point to the function where the gas permeability divided by the

dynamic viscosity is defined, `e_def` should point to a function which always return zero.

The next line of the table concerns the soil-gas flow field $\vec{q}$. It links the soil-gas problem and the radon problem. It must be observed, that in the soil-gas equation, $\vec{q}$ results from the calculation. Its relation to the pressure field is given in equation (2.42). In advective radon problems, $\vec{q}$ is a known flow field of soil gas. RnMod3d has a control variable called `flowfield`. In a soil-gas simulation, we may set this to `export` meaning that the calculated flow field $\vec{q}$ should be output (exported) to a file. Later, in a radon simulation, we may want to import this soil-gas flow field. We can do that by setting `flowfield` to `import`.

The two final lines of the table concern RnMod3d "probes" for flux measurements. In radon problems `J` and `Q` give the flux of radon and soil gas, respectively, in problems with pure diffusion, the soil-gas flow will be zero. In soil-gas problems, `J` is the calculated flow of soil gas whereas `Q` is without meaning (the model returns `Q` = 0). Flux measurements are done over some surface Ω as indicated in the table.

2.5 Finite-volume method

The RnMod3d code is based on a finite-volume (also called control-volume) method, closely related to the finite-difference method. Information about these numerical techniques can be found in [Patankar, 1980; Versteeg et al., 1995; Helmig, 1996; Ferziger et al., 1999]. The finite-volume approach has been used also in other models of radon transport [Loureiro, 1987; Andersen, 1992; van der Spoel, 1998].

The computational grid is divided into control volumes as sketched in figures 2.1 and 2.2.

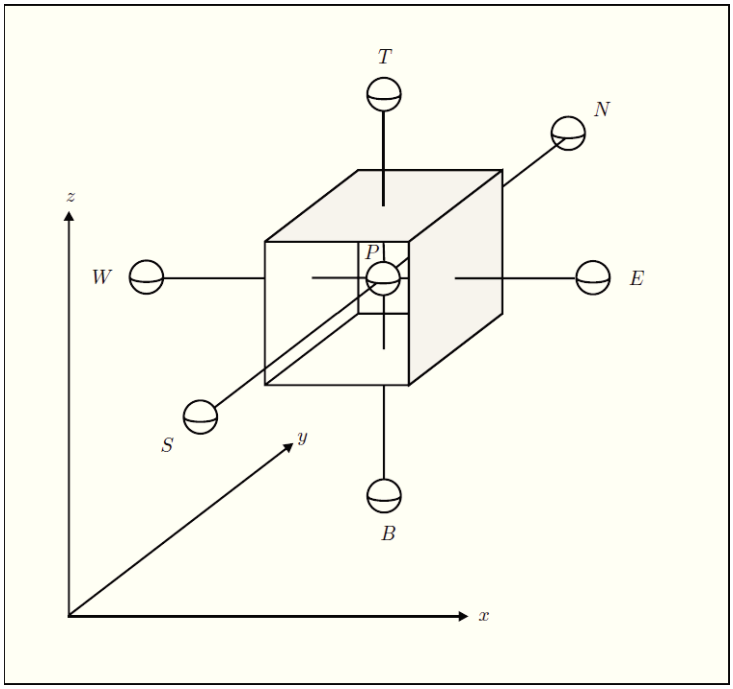

Figure 2.1 - Sketch of the control volume located around node P. the six adjacent nodes are called W for *west*, E for *east*, S for *south*, N for *north*, B for *bottom*, and T for *top*.

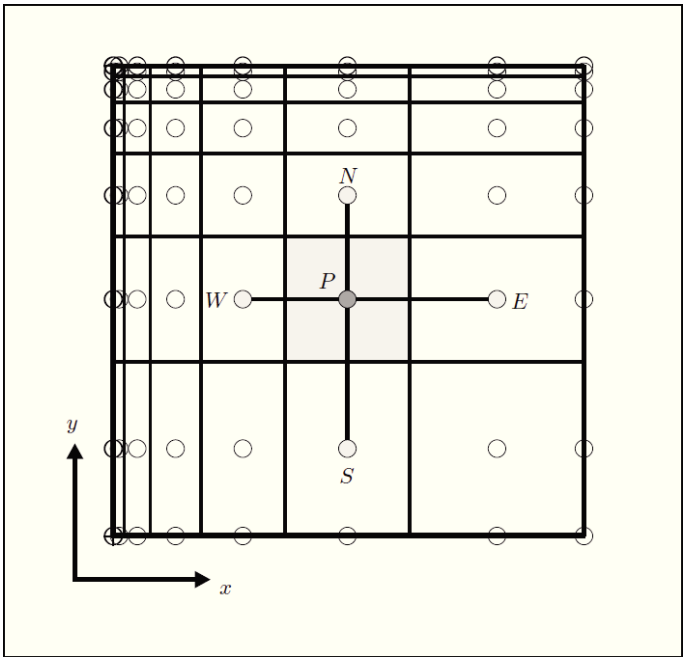

Figure 2.2 - Two-dimensional projection of a grid of control volumes. Observe, that control volumes need not have the same size, and that nodes are always located midway between control-volume interfaces.

Each control volume is a box with one (center) node and six faces. The prime variable is the value of the field at the nodes. Soil-gas problems are based on the disturbance pressure field *p(x, y, z)* whereas radon problems are based on the radon concentration field in the air-filled parts of the pores $c_a(x, y, z)$. Transport from one control volume to another is approximated by linear flux expressions. These expressions involve field values at pairs of adjacent nodes (e.g. *P* and *E* in figure 2.1). Fluxes are calculated for each of the six control-volumes faces. Considering sources and sinks and that the soil-gas and radon may accumulate in the control volume, we than require strict conservation of mass. This gives one algebraic equation for each control volume *P*:

$$a_P c_P = a_E c_E + a_W c_W + a_N c_N + a_S c_S + a_T c_T + a_B c_B + b \tag{2.43}$$

where the *a*'s and the *b* are coefficients, the *c*'s are the unknown field values, and where indices *E*, *W*, *N*, *S*, *T*, and *B*, refer to the adjacent control volumes on the east, west, north, south, top, and bottom sides of *P* respectively. The coefficients are calculated from material properties and control volume sizes.

We extend procedure to all of control volumes in the grid obtaining a system with *N* equations and *N* unknown field values. *N* is typi-cally 10000 or more, so it is virtually impossible to solve the equation by ordinary matrix inversion (the main matrix would be of size *N* by *N*). RnMod3d therefore uses iterative methods for finding the solution.

In summary, RnMod3d is based on field values at control-volume *nodes* and fluxes at *interfaces* between pairs of adjacent nodes.

2.5.1 Solution procedure

Essentially, RnMod3d solves a matrix equation of the form

$$A\vec{c} = \vec{b} \tag{2.44}$$

where A is a matrix of coefficients. These tell how the field quantity (i.e. pressure or radon) moves from one control volume to another. Hence, the matrix elements reflect material properties like diffusivity, size of control volumes etc. Most of the elements are zero since transport can take place only between adjacent control volumes. $\vec{c}$ represents a field of radon concentrations or pressures. If there are 10000 nodes in the grid then $\vec{c}$ is a column vector with 10000 elements. Likewise, A is a matrix with 10000 by 10000 elements. Finally, $\vec{b}$ is a vector with coefficients that relate to the source term. In radon problems, $\vec{b}$ reflects the radon generation rate. In time-dependent problems, $\vec{b}$ also include information about the field at the previous time step.

Because of the shear size of a typical matrix A, this equation cannot be solved by simple matrix inversion. Instead iterative solution procedures are used. The iterative solution procedures work as follows: first, a solution $\vec{c}_0$ is guessed; then on the basis of the procedure, an improved guess $\vec{c}_1$ is found; from this, a new field $\vec{c}_2$ is found etc. This is continued until convergence is met (in the first model run this field is zero all over: $\vec{c}_0 = \vec{0}$). In RnMod3d there are two available iterative solution procedures:

- Gauss-Seidel: This is a point-iterative solution procedure. The grid is swept point by point. For each point, we calculate an improved estimate of the field value directly from equation (2.45) as:

$$c_{P,i+1} = \frac{a_E c_{E,i} + a_W c_{W,i} + a_N c_{N,i} + a_S c_{S,i} + a_T c_{T,i} + a_B c_{B,i} + b}{a_P} \qquad (2.45)$$

where $c_{P,i+1}$ is the new improved estimate and all other field values: $c_{E,1}$, $c_{W,1}$ etc. are from the previous iteration.

- Thomas: The Thomas algorithm is similar to that of Gauss-Seidel. The only difference is that the Thomas procedure works line by line. This means faster convergence. The reason is that e.g. the impact of boundary conditions can reach all the way to the other side of the computational plane in one single

iteration. To further speed up convergence, the direction of lines is alternated from one iteration to the next: first, a line parallel to the x-axis is selected, then one parallel to the y-axis and finally one parallel to the z-axis.

The criterion for convergence is that the sum of residuals is less than a sufficiently small value *R_max* fixed *a priori* in the range $10^{-10} \div 10^{-20}$. This criterion is based on the reccommendations given by *Patankar* [1988]. After the *i-th* iteration, the guessed solution of the matrix equation is $\vec{c}_1$. To evaluate how close this solution is to the right one, we insert $\vec{c}_1$ into equation (2.44) and calculate the residual vector $\vec{r}_i$:

$$\vec{r}_i = A\vec{c}_i - \vec{b} \tag{2.46}$$

We then define the absolute sum of residuals R_i (after the *i-th* iteration) as:

$$R_i = \sum \left| r_i \right| \tag{2.47}$$

where the sum is over all nodes in the grid. In the end, the sum of residuals R_i should approach zero. However, as already mentioned, we consider the problem to be solved when $R_i < R\_max$. To better understand the significance of R_i, it is sometimes of interest to know the value:

$$R^0 = \sum \left| b \right| \tag{2.48}$$

where (as before) the sum is over all nodes in the grid. This is the value of R_i that is obtained where $\vec{c}_i = \vec{0}$. In the end, R_i should reach a value that is low compared with R^0.

To minimize the time to reach convergence, computations are often over-relaxed. The idea is quite simple if we take a look at one particular node in the grid. After the *i-th* iteration, the field value at this node is c_i. After the next iteration a new value called c_{i+1} is obtained. Each iteration leads to an improved estimate of the true value.

In the beginning, relatively large steps are taken (i.e. the difference between c_i and c_{i+1} is large), but eventually step sizes get smaller. If we know in what "direction" the true value can be found, we can take a larger step. With relaxation, we multiply the step size by a factor α:

$$c_{i+1,R} = c_i + \alpha\,(c_{i+1} - c_i) \tag{2.49}$$

The relaxation factor α can be set by the user with a proper control variable, but if it is too large unstability will result.

2.5.2 Boundary conditions

Equation (2.25) is solved for given boundary conditions. In most cases, c_a is set to some fixed value (e.g. zero at the soil-atmosphere interface), or the flux density of radon is set to some fixed value (e.g. zero at the boundary between soil and some low-diffusivity material). Some situations, however, require more elaborate boundary conditions [Andersen, 2001]. For example, the boundary condition at the interface between soil and indoor environment can be based on a 'room accumulation model' [Loureiro, 1987; Andersen, 1992]. If we consider a straight, smooth-walled crack in a concrete slab, the top of the crack ends in a well-mixed room with concentration c_{in}. The total flux of radon (in Bq s^{-1}) into the room (not just from the crack) is J. The air-exchange rate of the room is λ_v. Hence, the boundary condition needed to model radon entry through the crack is that radon concentration at the top of the crack equals c_{in} where c_{in} in turn fulfils:

$$J = V\,\lambda_v\,c_{in} \tag{2.50}$$

where V is the volume of the room. J is calculated by the numerical model and is a function of c_{in} (for example, diffusion of radon through the crack will diminish as c_{in} increases). The solution may be found iteratively: guess a value of c_{in}, calculate J with

the numerical model, and find an improved value of c_{in}. This process is continued until equation (2.50) is fulfilled. It may be necessary to underrelax the process.

In situations when soil interfaces with a free-air compartment, that is not well mixed (e.g. by turbulence from fans), it may be inappropriate to impose a fixed radon concentration at the boundary. A more refined treatment is to introduce a stagnant air layer between soil and open air and to extent the computational domain to include the film, or to derive special boundary conditions, for example based on diffusion through the film [Bird et al., 1960; Jury et al., 1984; Petersen et al., 1996; He et al., 1998].

In normal situation, the pressure field is found from equation (2.41), based on the requirement that the pressure should be fixed at a certain value at the boundary and that there should be fixed of soil gas flows values. Sometimes, the calculation of boundary pressures is linked to experimental data or other models. For example, *Riley et al.* [1996] used wind-tunnel data for the ground-surface pressure field around a house exposed to wind, and a computational fluid dynamics code for determining house ventilation rates in the presence of wind. Subsequently, a soil model was used for the calculation of sub-soil flows (soil venting) and radon entry into house. In another study, indoor airflows and pressure differences were calculated with a house infiltration model for given temperature and wind scenarios. These results were used as boundary conditions for a numerical model of radon entry [Janssen et al., 1998].

2.5.3 A study case

It is interesting to perform calculation for a study case [Andersen, 1992; Nazaroff. 1992; van der Spoel, 1998]. We consider a semi-infinite homogeneous soil column dominated by diffusion. Homogeneity here means that all material characteristics are uniform (and constant) in all parts of the soil. For example, the soil is assumed to have a uniform distribution of moisture and a uniform temperature. The radon concentration at the atmospheric surface is zero. For steady-state conditions, we obtain the solution to equation (2.25):

$$c_a(z) = c_{a,\infty}\left(1 - \exp\left(-\frac{z}{L_d}\right)\right) \tag{2.51}$$

where z is the depth and the deep-soil radon concentration is:

$$c_{a,\infty} = \frac{\varepsilon}{\beta}\frac{G}{\lambda} \tag{2.52}$$

Observe that at 10 °C, $c_{a,\infty}$ changes by a factor of $1/L \approx 2.8$ if we consider $c_{a,\infty}$ for a fully water-saturated medium compared to a dry medium [Rose et al., 1990]. For this reason (and others) it is therefore important to take moisture into account when modelling soil-gas radon. The diffusion length is:

$$L_d = \sqrt{\frac{D}{\beta\lambda}} = \sqrt{\frac{D_e'}{\lambda}} \tag{2.53}$$

where we have introduced the effective diffusivity D_e'. The relation to the bulk diffusivity is:

$$D = \beta\, D_e' \tag{2.54}$$

Observe, that under dry conditions, we have $D = \varepsilon\ D_e'$. In the literature it is sometimes unclear what type of diffusion constant that is applied (see e.g. *Rogers et al*. [1994]), and terms like 'effective', 'bulk', and 'pore averaged' diffusivities mean different things to different people. Fortunately, it appears that there is general agreement on the meaning of 'diffusion length': it is the inverse of the z factor in equation (2.51). Hence, equation (2.53) may sometimes be used to identify particular types of diffusivity. Finally, we state that the exhalation rate $j(0)$ (in Bq s^{-1} m^{-2}) from the surface at $z = 0$ is:

$$j(0) = D \frac{c_{a,\infty}}{L_d} \tag{2.55}$$

2.5.4 Special considerations

Numerical solution of equation (2.25) in medias that are not homogeneous requires special consideration as ε and β will change from point to point [Andersen, 1992; van der Spoel, 1998]. It is therefore not advisable to divide equation (2.25) by β or ε to obtain 'effective equations' (compare *Rogers and Nielson* [1991]) corresponding to write flux equations on the basis of flux per air-filled pore area. When media of different porosity, moisture content or temperature meet, it should be required that bulk fluxes are the same at each side of the interface between the media and that radon concentrations 'phase-by-phase' are continuous:

$$\vec{j}\,(+) = j\,(-) \tag{2.56}$$

$$c_a\,(+) = c_a\,(-) \tag{2.57}$$

$$c_w\,(+) = c_w\,(-) \tag{2.58}$$

$$c_s\,(+) = c_s\,(-) \tag{2.59}$$

where + and – designate the two sides of the interface. We can observe, that these requirements are automatically fulfilled by equation (2.25). A benchmark test relating to these problems is described in [Andersen et al., 1999].

Many expressions exist for gas diffusivity in soils. For radon diffusion, the most used expression is probably that of *Rogers and Nielson* [1991]. It appears that their empirical expression is an effective diffusivity in the sense given by equation (2.54):

$$D_e^{'} = D_0\ \varepsilon \exp\left(-6\, m\varepsilon - 6\, m^{14\varepsilon}\right) \tag{2.60}$$

where $D_0 = 1.1 \cdot 10^{-5}$ m^2 s^{-1} and m is the water saturation $\varepsilon_w / \varepsilon$. This interpretation has been tested by *van der Spoel* [1998] for wet sand.

All the equations given here treat soil as a porous medium. However, some studies indicate that soil properties of interest for gas flow may be dominated by bio-porosity created by roots or worms [Garbesi, 1993; Holford et al., 1993; Hoff, 1997]. This can lead to preferential flow. This does not necessarily mean that it is inappropriate to model such soils as 'porous media equivalents'. For example *Hoff* [1997] studied a sample of clayey-till and demonstrated that although the bioporosity control-led the effective gas permeability (and provided fast-flow paths for radon-222 as well as radon-220) it was a fine approximation to model the column as if it was homoge-neous.

2.5.5 Model limitations

As discussed in this chapter, RnMod3d is a computer code of radon transport in porous media. It can be used for: simulations of vertical profile of radon concentrations in soil and flux calculations of radon from the soil surface into the atmosphere; simulations of entry of soil gas and radon into houses in response to indoor-outdoor pressure differences or changes in atmosphere pressure; calculation of radon exhalation from building materials; error analysis of measurement procedures related to radon. Three-dimensional steady-state or transient problems with Darcy flow of soil gas and combined generation, radioactive decay, diffusion and advection of radon can be solved. Moisture is included in the model, and partitioning of radon between air, water and soil grains (adsorption) is taken into account. Most parameters can change in time and space, and transport parameters (diffusivity and permeability) may be anisotropic.

Nevertheless, RnMod3d has a few limitations that, however, do not affect its efficacy as technical research tool. The model cannot treat the non-Darcy flow of soil gas or soil-gas flow in non-isothermal soil. Moreover, in transient soil-gas simulations there are two restrictions: the air-filled porosity must be constant in time, and the pressure variations must be small (compared with the absolute pressure). Finally, RnMod3d is based on orthogonal grids and not suitable for complex geometries.

Chapter 3

In situ measurements on Mt. Etna volcano

It is known that there is a scientific discussion if the radon concentrations in the soil and underground water can be used as a possible earthquakes precursor. From many years much efforts have been made in order to improve in-situ radon data monitoring and analysis, technical methodologies and mathematical modeling, with the aim to reinforce the link between ground radon concentration anomalies and geodynamical events. Because of the complexity of its transport mechanisms, however, the correlation needs much more investigations in order to clearly and firmly established it. In a volcanic environment, in particular, some variables (very high temperatures, magma uprising, degassing from soil surface) contribute to further increase the complexity of the problem, requiring even more careful and detailed studies.

In this chapter, in-situ measurements of radon activity concentration together with soil thoron and carbon dioxide (CO_2) efflux on Mt. Etna volcano are discussed. Both horizontal and vertical profiles of radon activity concentration were studied, even in the vicinity of a active fault system. A first comparison between experimental data and model calculations has been also performed.

3.1 Tectonic structure

The Calabrian arc and the eastern Sicily are currently affected by large earthquakes and by intense volcanic activity. The main regional feature in this area is given by a prominent fault belt that runs more or less continuously along the inner side of the

Calabrian arc, extending through the Strait of Messina along the Ionian coast of Sicily as far as the Hyblean Plateau. The fault belt also controls the eastern sector of the Aeolian archipelago and the eastern Sicily coastline, bordering wedge-shaped extensional basin in the Ionian offshore [Monaco et al., 2000]. This regional fault belt, often called the Siculo-Calabrian rift zone, is about 370 km long and is made up of distinct fault segments with lengths ranging from 10 to 45 km (figure 3.1) that in Plio-Pleistocene times controlled the overall evolution of a system of marine sedimentary basins. They strike (1) N-S, in northern Calabria; (2) NNE-SSW in southern Calabria, nort-easter Sicily and in the Hyblean Plateu; and (3) NNW-SSE, in the Gulf of Patti and in the south-eastern Sicily.

These structures strongly deform the Quaternary deposits outcropping in the area whereas their surface expression, on land, includes huge fault scarps which define the modern fronts on the main mountain ranges of the region (Catena Costiera, Serre and Aspromonte), In eastern Sicily the fault belt mostly extends offshore, bordering the uplifted Peloritani mountains range and the Mt. Etna-Hyblean region which forms, as a whole, the footwall of this extensional fault zone. The fault belt also controls the development of different active volcanoes, as the easternmost islands of the Aeolian archipelago (Stromboli, Lipari and Vulcano) and the Mt. Etna. From a seismologic point of view, the Calabrian arc and eastern Sicily, as well as the Southern Appennines, represent very active areas which are characterized by historical crustal events, the largest of which reached an MCS intensity of X-XI (magnitude $6 < M \leq 7.4$). The epicenters of these earthquakes outline a seismic belt that includes the largest earthquakes occurred in the region (as the 1783 earthquake sequence, the Messina earthquake of 1908, the Monteleone earthquake of 1905 and the 1693 earthquakes) and runs mainly along the downfaulted Pleistocene basins on the Thyrrenian side of the Arc and along the Ionian coast of Sicily.

The seismicity of the Calabrian Arc and eastern Sicily is defined by the occurrence of both crustal ($H < 35$ km) and subcrustal ($H > 35$ km) earthquakes. The latter are located beneath the southern Thyrrenian sea, reaching depth of 470 km and depicting a slab dipping about 45° toward NW. The occurrence of a gap in depth distribution (bet-

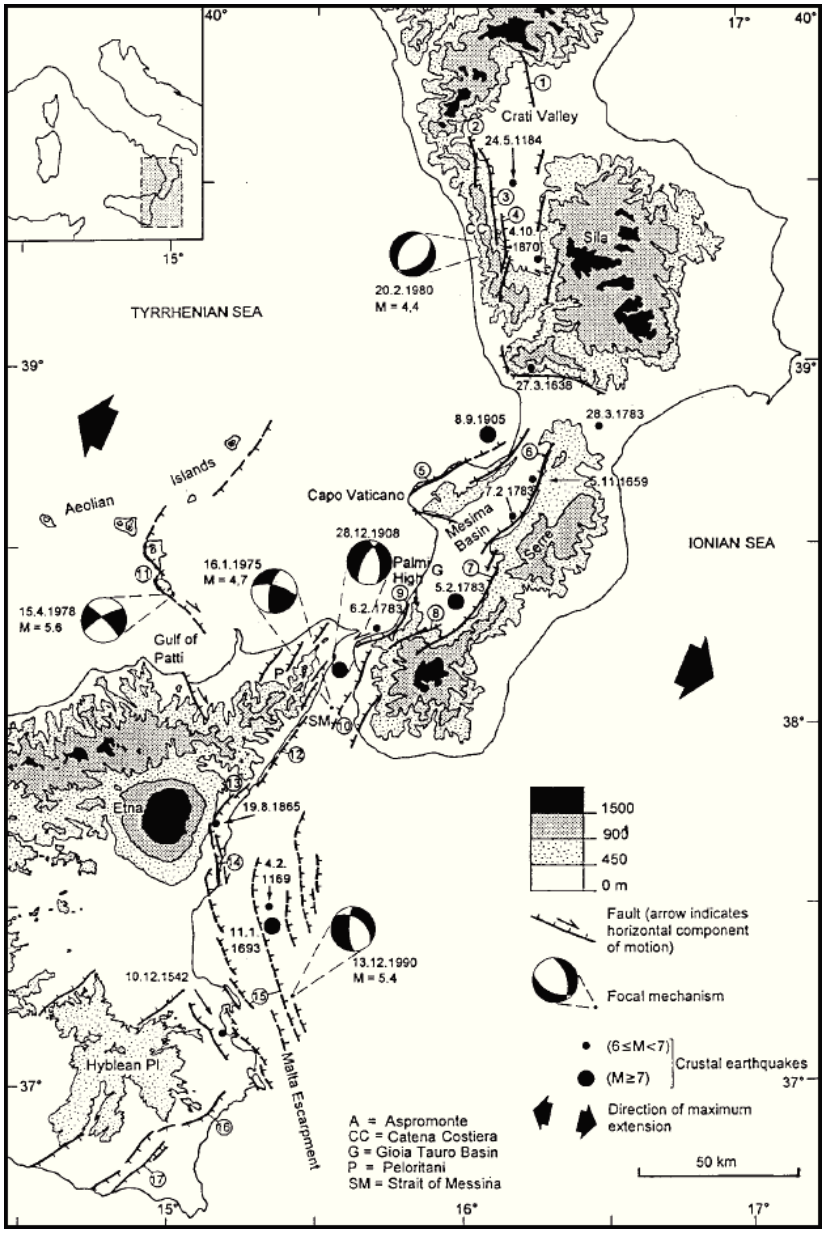

Figure 3.1 - Seismotectonic map of the Calabrian arc and eastern Sicily. Number refer to fault segments: 1) Castrovillari; 2) Fagnano Castello; 3) S. Marco-S. Fili; 4) Montalto-Rende; 5) Capo Vaticano; 6) Serre; 7) Cittanova; 8) Santa Eufemia; 9) Scilla; 10) Reggio Calabria; 11) Lipari-Vulcano; 12) Messina-Taormina; 13) Piedimonte; 14) S. Alfio-Acireale; 15) western offshore; 16) Avola; 17) Rosolini-Pozzallo [Monaco et al., 2000].

ween 50 and 200 km for earthquakes with M ≥ 5) suggests the existence of a discontinuity that may be related to the detachment of Ionian lithosphere during the Middle Pleistocene times. Crustal seismicity is defined by historical and instrumental earth-

quakes which occurred since 1000 AD. The epicentral distribution of the M ≥ 5 earthquakes (figure 3.2) outline a seismic belt which runs along the Thyrrenian side of Calabria and, southward, along the Ionian coast of Sicily and the Hyblean Plateau. Some earthquakes with M < 6 have also been recorded on the Ionian side of Calabria [Monaco et al., 2000].

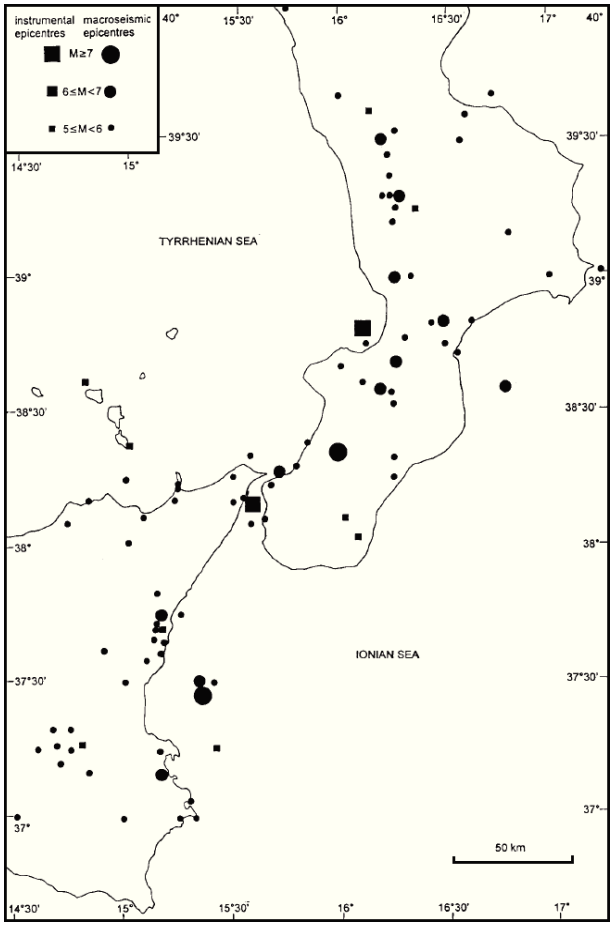

Figure 3.2 - Map of the crustal seismicity (H < 35 km) since 1000 AD of the Calabrian arc and eastern Sicily [Monaco et al., 2000].

Fault plane solutions available for some of these events, as for the Messina-Reggio Calabria earthquake (December 28, 1908; M = 7.1) and for other smaller events that occurred in the Strait of Messina (January 6, 1975; M = 4.7), in the Gulf of Patti (April 15, 1978; M = 5.6), in the Crati Valley (February 20, 1980; M = 4.4), and in the south-eastern Sicily (December 13, 1990; M = 5.4), show that the deformation pattern along

the main fault belt is consistent with an ESE-WNW oriented extension [Monaco et al., 2000].

3.1.1 Eastern Sicily

Our interest is pointed to the eastern Sicily. In this region, the Siculo-Calabrian rift is formed by a few fault segments mostly running along the Ionian coastline, and striking both NNE and NNW. The major fault segments include the Messina-Taormina fault, the Piedimonte and the S. Alfio-Acireale faults that are located at the base of the eastern flank of Mt. Etna volcano, the western fault (extending along the Ionian offshore) and the Avola and Rosolini-Pozzallo faults.

The Messina-Taormina fault (12 in figure 3.1) is an east-facing, 30 km-long, normal fault running parallel to the coastline of the Ionian offshore and bounding the uplifted block of the Peloritani mountain range. The fault-related Quaternary uplift of the Peloritani mountains is clearly indicated by the occurrence of several levels of marine terraces engraved on the crystalline rocks, and by the uplifted Holocene coastlines. Thyrrenian sediments located at an elevation of about 130 m and 5 kyear old shoreline uplifted up to 5 m [Monaco et al., 2000] suggest, for this fault segment, a minimum vertical slip rate of about 1 mm/yr.

At south of Taormina, the fault belt penetrates onshore where it is represented by the 15 km-long, NNE trending Piedimonte fault segment (13 in figure 3.1). The fault exhibits a 60 m high cumulative escarpment across the 35 kyear-old volcanic on Mt. Etna which is consistent with an average vertical slip-rate of 1.7 mm/yaer. The Piedimonte fault also effsets the Middle Pleistocene clays that crop out at the base of the volcanic edifice. Since these clays lie at ~50 m above sea level in the hangingawall and at an elevation of up to 550-600 m on the footwall side of the fault, the long-term slip-rate of Piedimonte faults appears to be in the order of 1.1-1.2 mm/yaer.

Southwards, the fault belt swings to a NNW trend forming the S. Alfio-Acireale fault zone (14 in figure 3.1). The fault zone occurs at the base of the eastern flank of the volcano, extending for about 20 km from Acireale to S. Alfio. It is made of several

NNW trending fault segments that control the present-day topography and show steep escarpments with very young, mostly Late Pleistocene to Holocene, morphology. The S. Alfio fault is characterized by a sharp, fairly linear scarp, with different cumulative heights along strike and a particularly large escarpment at its northern end.
From Catania to Siracusa, the fault belt continues offshore, where it includes several segments striking NNW-SSE. These segments, as shown by several seismic profiles carried out in the Ionian offshore, display an overall right-hand and echelon arrangement and are represented by two main east-facing normal faults that affect the entire crust and define, in the hangingawall, well-developed eye-shaped basins infilled with Middle-Upper Quaternary syn-rift clastic wedges thickening towards the boundary faults. The most prominent fault segment of this branch of the Siculo-Calabrian rift is represented by the western fault (15 in figure 3.1), that extends parallel to the coastline for a total of about 45 km. This fault segment cuts the thinned crust of the Ionian domain and re-activating the Malta-escarpment to the south, offsets the sea-floor creating well-developed steep scarps that reach heights ranging from about 80 to 240 m.
The Avola fault (16 in figure 3.1) is represented by a 20 km long, east-dipping normal fault fault that separates the Avola mountains from the coastal plain. The Avola fault controls the present-day topography, showing a steep escarpment with very sharp, mostly Late Pleistocene to Holocene, morphology.
Finally, in the south, the Rosolini-Pozzallo fault system (17 in figure 3.1) is constituted by two main left-stepping fault segments characterized by very sharp, linear scarps that, extending for a total length of about 20 km, show heights reaching values of 70 m. The faults escarpments offset the large 480 kyear-old wave-cut platform surface.

3.2 Mt. Etna

Mount Etna is a typical strato-shield volcano located on the external margin of the Appenninic-Maghrebian belt (figure 3.3). This belt is crossed by several seismogenic structures, which define a complex (and not yet fully understood) tectonic framework.

The volcano, which is about 3360 m heigh, has building up for about 500,000 yrs, producing magmatic activity of both tholeiitic and alkaline affinity [Patanè et al., 1994]. The structural features of the Etna region and their relations to the main tectonic structures of Sicily are controlled by convergence of the African and Eurasian plates (figure 3.3). This motion resulted in a significant distortion of the litospheric front of the African plate, including the opening of the Thyrrenian basin about 7 Myear ago and subduction of the Ionian sea-floor beneath the eastern margin of Calabria. The subduction process also caused the genesis of the Calabro-Peloritan Arc, together with longitudinal and transversal brittle brittle deformations in the Sicilian Northern Chain and in eastern Sicily [La Delfa et al., 2001].

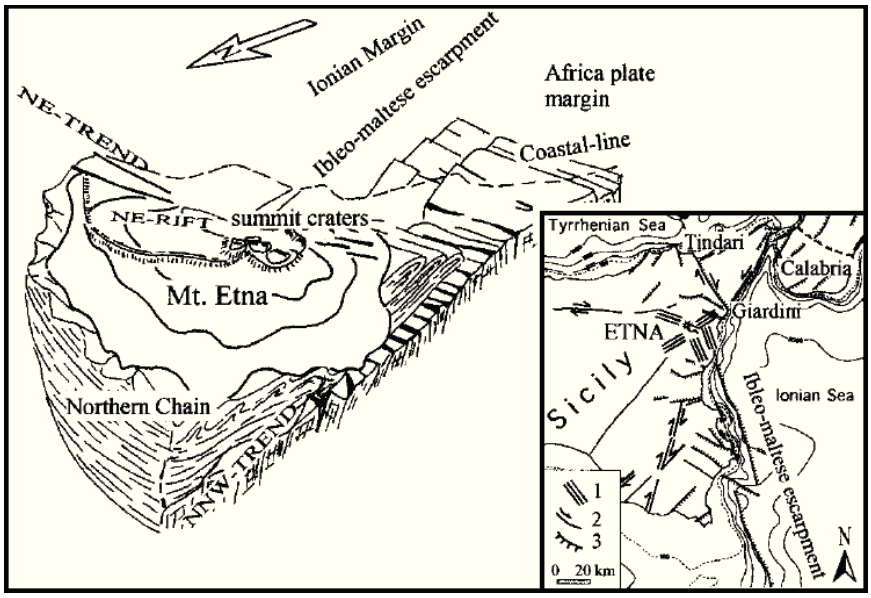

Figure 3.3 - Geodynamic framework of Mat. Etna.

Mount Etna is cut by several fractures and faults closely associated with various structural directions. It has grown at the intersection of two regional master faults, the Malta Escarpment and the Messina-Fiumefreddo line striking respectively NNW and NE, and at the front of the Appennine-Maghrebian thrust belt (figura 3.4a). The former is a crustal scale fault with a vertical dip separation of 3000 m at the contact of the continental African Platform and the oceanic Ionian basin. The latter marks an exten-

sional zone through South Calabria and Northeast Sicily that has developed as far as the Etna area. The tectonic setting of Etna's flanks results from the interaction of regional tectonics and local scale volcano-related processes [Azzaro, 1999].

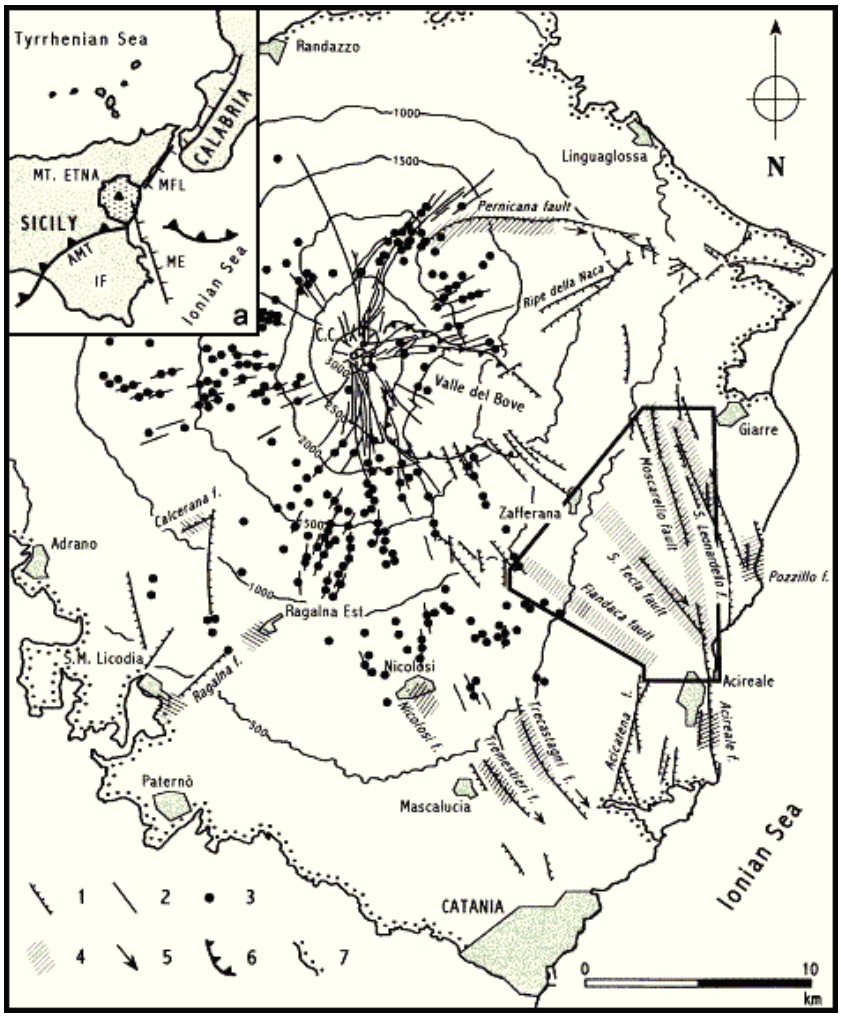

Figure 3.4 - Simplified structural map of Mt. Etna: 1) faults with bar on downthrown side; 2) eruptive fissures; 3) cinder cones; 4) coseismic surface faulting zones; 5) strike-slip components; 6) caldera rims; 7) limit of Etna volcanic; CC) central crater. Box indicates area of the "Timpe" fault system. Inset map (a) shows the regional geological setting: AMF, front of the Appennine-Maghrebian thrust belt; IF, Iblean Foreland; ME, Malta Escarpment; MFL, Messina-Fiumefreddo line [Azzaro, 1999].

The analysis of the main morphological and tectonic lineaments shows a different dynamic behavior between the western and the eastern parts of the volcano [La Delfa

et al., 2001]. The most outstanding tectonic features are confined to the volcano's eastern flank, where the "Timpe" system represents the northernmost prolongation of the Malta Escarpment and forms a NNW-SSE-trending system of parallel east-facing step faults of considerable length (8-10 km) and vertical offsets (up to 200 m) that downthrow toward the sea (figure 3.4). To the north this system is interrupted by the E-W Pernicana fault, which cuts a large part of the volcanic edifice and by the NE-SW Ripe della Naca system. [Azzaro, 1999]. The NNE rift beginning from the summit NE crater extends downwards to the Pernicana fault which represents a major dislocation roughly trending W-E, with its south rim deepened by more than 40 m. This fault is located about 5 km north of the Valle del Bove depression, another structured feature resulting from ancient flank collapses and caldera system [La Delfa et al., 2001].

The west flank, on the contrary, is buttressed by the orogenic Northern Chain and only affected by morphological flexures and minor faults which follow the regional tectonic directions. These are mainly trending N-S, NNW-SSE and NE-SW (figure 3.4) altough nearly W-E flexures are also encountered in the lower northern region. It should be noticed that the SW-NE-trending faults are evident in the lower Southwest region where they form the Ragalna-Adrano system. On the west flank, more generally, the earthquakes are located along NNW-SSE and NE-SW trends and tend to occur at greater depth than on the east side of the volcano [La Delfa et al., 2001]. The latter, evidence of which also appears in the lower south-western side of the volcano, represents the southern prolongation of the Messina-Fiumefreddo line. Finally, at the southern flank two isolated structures - the Trecastagni and Tremestieri faults - present morphological evidence [Azzaro, 1999].

The geodynamic behavior of Mount Etna seems to be controlled by the flank instability processes, implying the seaward sliding of the volcano's eastern side as a result of a complex interaction between regional tectonic stresses, gravity forces acting on the volcanic edifice and the dyke-induced rifting. In this context, the faults dissecting the eastern side of Etna represent the main structures which accommodate the downslope movement of this sector of the volcano, whereas the Pernicana and the Trecastagni-Tremestieri fault systems, or the Ragalna system as an alternative to latter, seem to

identify the northern and the southern boundaries respectively of the unstable sector. Most of the faults move with high slip-rates as indicated both by the appreciable offsets of Holocene and historical lava flows and by fault creep due to the shallow seismicity. Instrumental data, according to historical and recent macroseismic information indicate that more than 80% of the earthquakes are shallower than 5 km and occur mainly on Etna's eastern flank, where, although characterized by moderate magnitudes ($M \leq 4.8$), they may produce destructive effects - epicentral intensities reaching often the VIII-IX grade MSK in narrow zones - and by coseismic surface faulting. Fault plane solutions of these events indicate a general E-W extension whereas deeper earthquakes (H = 10-30 km) prevailing in the western side are associated with regional N-S oriented compressive stresses [Azzaro, 1999].

3.2.1 Site location

We focused on the eastern flank of Mt. Etna, being the most interesting one from a geological point of view. In particular, three different sites was chosen (figure 3.5). The first one, Vena (V), is located at 825 m a.s.l.; the second near the village of Santa Venerina (SV) at 400 m a.s.l.; and the last one in Cugno di Mezzo (CDM), located at 1400 m a.s.l. in the southern edge of the eastern caldera of the Valle del Bove.
Vena is a village near Piedimonte in the NE flank of Mt. Etna. The structural belt system is that of the Naca and Piedimonte fault system. On the basis of its morphostructural aspects, this highly tectonic area can be divided into two structurally linked systems where the NE-SW trend is always the tectonically dominant one. The whole north eastern flank of the Etnean complex, in fact, is characterized by disturbances in that orientation, in particular along a strip developing almost continuously by the Naca and Piedimonte fault system. The Naca fault system is a couple of sub-parallel step faults facing the southeast with an overall extent of about 200 m. They give rise to escarpments, locally called Ripe della Naca, dislocated by minor faults running N-S. The eruptive events of 1928 were associated with this system, originating from effusive cracks along one of the main fault lines.

The Piedimonte fault system is the repetition at NE of the Naca fault system of the dominant NE-SW trend. It is a step fault between Piedimonte and Fiumefreddo, variously dislocated by faults on NW-SE average trend; the most developed of these partly coincides with the upper course of the Fogliarino river. The NE-SW tectonic li-

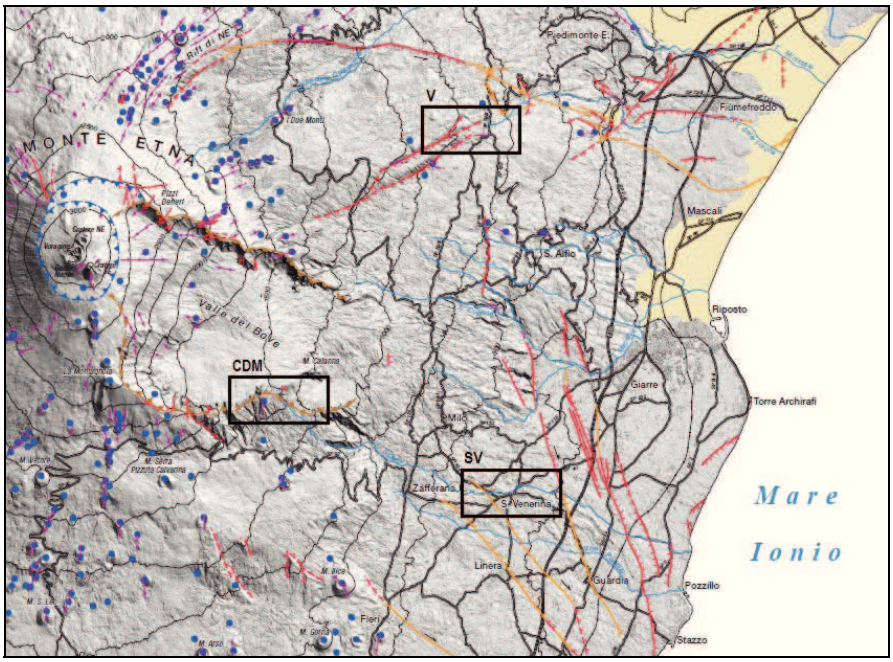

Figure 3.5 - Etna fault structure and site locations (black box). From [Azzaro et al., 2012].

nes then proceed as a group until Calatabiano in the peripheral sedimentary terranes, where the lower the "Piedimonte Formation" towards the coast; they also continue to the south forming a structural top (Contrada Saette). The structural trend of the defined Naca and Piedimonte fault system is dislocated by minor faults generally running WNW-ESE. The main faults are in steps facing the east. The trend can be considered one of the most important elements for interpreting correctly the structural pattern of the volcano. In fact the swarm of the eruptive cracks characterizing the northern slope of the Valle del Bove between Piano Provenzana and Monte Scorsone can be correlated with the trend. It is particularly interesting observe that the disturbances connected with the trend appear dislocated on the north-eastern flank by transverse faults

along the NW-SE trend. Locally these faults seem to show large strike-slip movement. The division of the structural trend into the above described two systems is probably connected with a disturbance having a NW-SE trend, completely covered by the Scorciavacca lavas and therefore with no *in situ* evidence to support it [Lo Giudice et al., 1992].

The village of Santa Venerina is located in the lower eastern slope of Mt. Etna, at altitudes between 200 and 480 m above sea level at an average distance from the Ionian coast of about 5 km. This area is mainly affected by the NW-SE trending Santa Tecla fault and it is crossed by the Timpe Fault System (TFS). In particular, the Santa Venerina faults appear to be important tectonic elements connecting the TFS with the central part of the volcano and the volcano-tectonic depression of the Valle del Bove [Azzaro et al., 2013]. These structural discontinuities are strictly linked to the geodynamics of the volcano, and seem to play an important role in the readjustment of crust masses on the more unstable eastern flank of the volcano, before, during and after eruptive periods [La Delfa et al., 2010]. It should be stressed that all these faults are very active also from the seismic point of view, representing the sources of the strongest earthquakes reported in the seismic catalogue for the last centuries [Azzaro et al., 2013]. Moreover, the Santa Venerina area is well known for high CO_2 soil gas emissions [Burton et al., 2004; D'Alessandro et al., 1992; Giammanco et al., 1995; Bruno et al., 2001].

3.3 Experimental devices

Instruments for the measurement of radon and its decay products are based mostly on the detection of alpha particles, the energy of which ranged from 5.5 for ^{222}Rn to 7.7 MeV for ^{214}Po. Usually, radon measurements, especially in impervious zone, are carried out by means of passive devices, i.e. detectors in which the radon concentration is measured under natural condition, radon entering the detection volume by mere diffusion. Measurements in soil, in particular, are usually done by solid state nuclear

tracks detectors (SSNTD), although these can give only long-term measurements and need frequent substitutions to read the tracks and, at the same time, avoid saturation effects. Active devices, on the contrary, involve the pumping of gas into the detection instrument and allow short time period radon monitoring.
In view of different type of measurements of gas radon in soil, both active and passive detection techniques were applied in this study. In particular, measurements of radon and thoron were performed to investigate transport mechanisms in fracturated media by means of active devices with silicon diode detector and ionization chamber; passive measurements were performed using plastic nuclear track detectors, CR-39 type, to determine vertical in-soil radon profile.

3.3.1 Genitron AlphaGUARD ionization chamber

The AlphaGUARD PQ 2000PRO by GENITRON Instruments GmbH, Germany, is a compact system for the continuous determination of radon and thoron concentrations which uses a real-time ionization chamber to detect the alpha-particles from ^{222}Rn and ^{220}Rn decay and allow both short and long term analysis. It can operate in two modes: diffusion mode (with 10 min and 60 min measuring cycles) and flow mode (1 min or 60 min measuring cycles), maintaining in both cases its linear response from 2 Bq/m^3 to 2 MBq/m^3 of total concentration. The cylindrical chamber of the AlphaGUARD has an active volume of 0.56 liters. The metallic interior constitutes the anode, setted at a potential of +750 V respect to the stiff centre electrode located along the longitudinal axis. Figure 3.6 shows the ionization chamber scheme.
For digital signal processing there are three independent signal processing channels. To each channel belongs a specific analog-to-digital converter. Spectrometric analysis is performed through signal characterization according to the pulse height and shape, allowing differentiation between real alpha-decay events and other interference effects. Gas enters for diffusion, via a large surface glass fiber filter, into the ionization

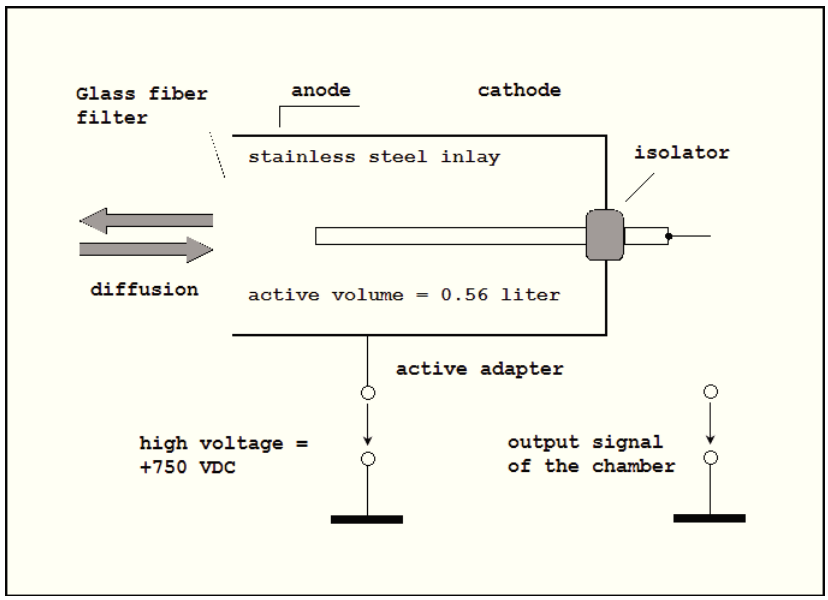

Figure 3.6 - Ionization chamber scheme

chamber. Through the glass fiber only the radon isotopes pass, while the progeny products are prevented to enter the ionization chamber; at the same time the filter protects the interior of the chamber from contamination of dusty particles. Operating in flow-through mode the device needs a flow adapter that, closing the diffusion glass fiber, allows the connection with the pump. In any case, radon and thoron interfere with each other inside the ionization chamber and the device detects alpha emitters without any energy discrimination.

In our measurements we have used a soil-gas unit consisting of a drilling rod with an exchangeable drilling tip with air-lock, which is closed by a rivet and a capillary probe. The drilling rod is hit into the ground and the capillary probe is inserted into the drilling rod. The higher part of the capillary probe is connected to an aquastop filter, in order to reduce as much as possible the moisture, then to a nylon filter (ϕ = 30 mm), with pore diameter of 0.45 μm and a glass fibre pre-filter of 1 μm, that let only the radon pass. The system is connected to the AlphaGUARD by means of a pump. The pump has been set at an aspiration rate of 0.05 liter/min and the probe is hit at 1 meter depth into the soil.

The technical specifications of the device are reported in table 3.1.

Table 3.1 - AlphaGUARD technical data

Type of radon detector	Ionization chamber, HV ≈ 750 VDC
Total detector volume	0.62 l
Active detector volume	0.56 l
Type of Rn-FP filter	Glass fiber filter
Detector filling mechanism	Design-optimized far fast passive diffusion or automatic filling via active adapter
Transient response function (time delay)	Signal >30% after 10 min Signal >70% after 20 min Signal >90% after 30 min
Detector signal acquisition	Fast digital signal sampling network, using three separate ADC-channels
Spectral signal extraction	DSP (Digital Signal Processing), on-line-cross correlation algorithms
Sensitivity of detector	1 CPM at 20 Bq/m^3 (0.55 pCi/l)
Background signal due to internal detector contamination	< 1 Bq/m^3 (0.03 pCi/l)
Range of radon concentration Lower limit Upper limit (1-min flow-through mode)	 2 Bq/m^3 2 000 000 Bq/m^3 (1 000 Bq/m^3 – 2 000 Bq/m^3)
Resolution on LCD display	1 Bq/m^3
Foldback protection	> 10 000 000 Bq/m^3
System linearity error	< 3% within total range
Instrument calibration error	3% (plus uncertainty of primary standard)
Operating range	-10 … +50 °C (+14 … 122 °F) 70 … 1100 mbar 0 … 99% rH

3.3.2 Durridge RAD7 solid state detector

The RAD7 alpha detector by Durridge Company Inc., USA, uses a solid state silicon ion-implanted detector. The system possesses an internal sample cell of about 0.7 liters and has a hemispherical shape, as can be observed in figure 3.7. The inside of the hemisphere is coated with an electrical conductor and a high voltage power supply charges the inside of the conductor to a potential of about 2000-2500 Volts relative to the detector. This creates an electrical field throughout the cell. The electrical field propels the positively charged particles onto the detector in the periodic-fill

cell. A decaying ^{222}Rn atom within the cell leaves behind a positively charged ^{218}Po, which is accelerated onto the detector and sticks to it. The ^{218}Po nucleus has a relatively short half-life and when it decays, it will have a 50% chance [Durridge, 2000] of entering the detector where it will produce an electrical signal, and the energy of the alpha particle can be measured. Then, the electrical signal recorded from the decay of the radionuclide is amplified, filtered and then sorted according to its strength. Different modes of functionality of the RAD7 allow for detection of radon from the ^{218}Po signal, but it can also determine the thoron concentration from the ^{216}Po signal. The ^{218}Po and ^{216}Po signals arise from the 6.00 and 6.78 MeV alpha decays respectively and the alpha energies from the other decay products are ignored. The RAD7 device is almost completely insensitive to further beta decay occurring subsequently in the ^{238}U and ^{232}Th decay series.

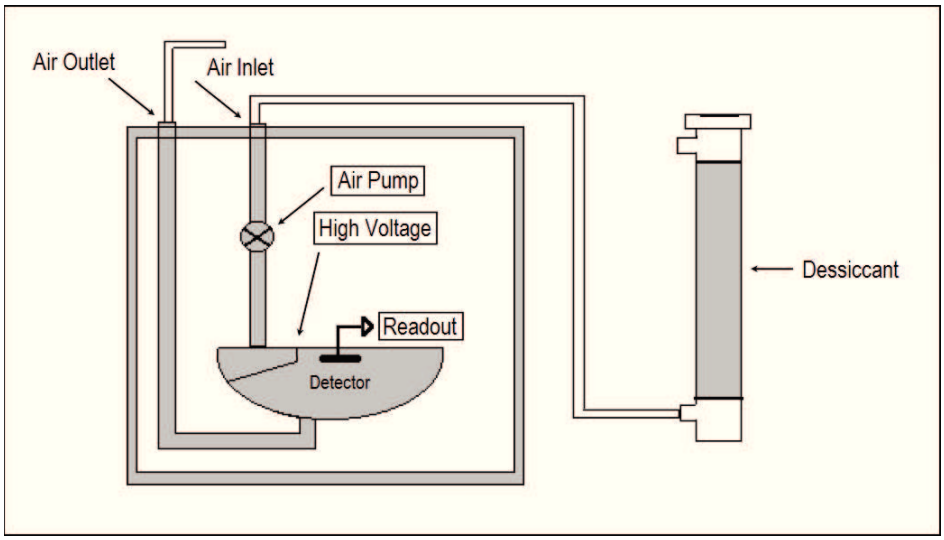

Figure 3.7 - Schematic of the RAD7. The function of the desiccant is to adsorb any moisture that was pumped into the tubing to keep the air relatively dry. However, the radon might also get adsorbed on the desiccant granules; this becomes a problem at very high radon concentrations.

The electrical signal produced in the detector due to alpha particles after amplification is converted to digital form, to allow energy spectra till to 10 MeV, the region of interest being 6 - 9 MeV region, since most of the radon and thoron decay products produ-

ce alpha particles in that range. In particular, 6.00 MeV α-particles from the ^{218}Po one used to derive the radon concentration, while α-particles produced by ^{216}Po and ^{212}Po account for thoron.

3.3.3 CR-39 nuclear track solid state detectors

The principle of radon detection by solid state nuclear track detectors is based on the production of alpha-particle tracks in solid-state materials, such as allyl diglycol carbonate ($C_{12}H_{18}O_7$) plastic films CR-39. The CR-39 detectors supplied by Mi.am S.r.l., Italy, (active area of 25 × 25 mm^2) were placed inside a diffusion chamber of NRPB type [Bartlett et al., 1988] designed to allow the entrance of radon only and neither its decay products nor thoron. The alpha-particles emitted in the radon decay inside the diffusion chamber generate a damaged region in the CR-39 detectors as a latent track.

In order to enlarge the alpha tracks after the exposure, the CR-39 detectors were chemically etched with a 6.25 M NaOH solution at 98 °C for 1 hour [Modgil, 1984]. Then, after removing from the bath, the detectors were water-washed (first time with warm distilled water) and kept 30 min in a 2% acetic acid-distilled water solution (with stirring) to discontinue etching. Subsequently, detectors were water-washed again and dried. The detector read-out was performed with a previously calibrated semiautomatic system. The system consists of an optical microscope (with 10× magnification) connected to a personal computer by means of a CCD camera. A video acquisition software allows capture and storage of the microscope images, segmented in *Field of View* (FOV), with 720×576 resolution. The stored images were then analyzed by means of the ImageJ 1.29x (Image Processing and Analysis in Java) freeware software [NIH]. On this platform, a routine was built for processing each single FOV. More than 200 FOVs were acquired for each detector and processed, discriminating the tracks according to their minor and major axis, their area and grey level. The software routine gives as output both the exposure in Bqh m^{-3} and the ^{222}Rn concentration in Bq m^{-3}, which represent an integration over the entire exposure

period of the detector. The lower limit of detection is of 5 Bq m^{-3}, calculated for an exposure time of three months [Immé et al., 2013].

3.4 Radon transport in fracturated porous media

Spot measurements of soil-gas radon were performed, together with soil thoron and soil carbon dioxide (CO_2) efflux, along a horizontal transect across the fault that, belonging to the Santa Venerina faults system in the east flank of Mt. Etna volcano, comes up over Zafferana Etnea via Primoti (SVF).

The soil-gas analysis method was based on the principle that faults and/or fractures are highly permeable pathways in rock formation where gases, in general, can migrate upward from the deep crust and/or mantle and retain their deep-source signatures in the soil cover. Recent studies [Atallah et al., 2001; Baubron et al., 2002; Ajari et al., 2002; Burton et al., 2004] showed that soil ^{222}Rn tends to increase in proximity to main fault planes. This behavior was explained as a change in the rock properties along the faults (i.e., increased soil permeability to gas; higher surface-to-volume ratio in the fracturing rock, that facilitates radon release from the solid matrix because, due to its short half-life, any radon created must be near the free surface of a rock in order to have any probability of escaping into the gas phase). In this scenario, anomalies of soil-gas radon and other trace gases, like helium and hydrogen, could be correlated with high degassing of carbon dioxide (CO_2), methane (CH_4), Nitrogen (N_2), thus substantiating the occurrence of advective transport of radon through the soil column by a carrier gas, whose flux is controlled by pressure gradients. Among the soil gases in volcanic or geothermal environments like Mt. Etna volcano, carbon dioxide is normally the most important in terms of both abundance and efflux. For this reason, it is essential to correlate ^{222}Rn and CO_2 measurements in soil-gas emissions from such environments.

In order to investigate how fractures in the ground can affect the radon transport and its activity concentration in the vicinity of the soil surface, spot measurements of both

soil-gas radon isotopes were performed, by means of both active devices described in section 5.3, along a profile orthogonal to the main fault plane in the framework of a collaboration with the Catania Department of the Istituto Nazionale di Geofisica e Vulcanologia. The soil-gas was drawn through the 1 m long soil probe using the internal pump of the RAD7 detector and was then passed through two filters: the first one (drierite, 97% $CaSO_4$, 3% $CoCl_2$) removes the moisture and the second one allows only radon to enter the detection system chambers by removing atmospheric particulate as well as radon daughters. At the same time, diffuse CO_2 effluxes were measured using the accumulation chamber method, which consists of measuring the rate of increase of the CO_2 concentration inside a cylindrical chamber opened at its bottom placed on the ground surface. The chamber has an internal fan to achieve an efficient gas mixing and is connected with a portable nondispersive infrared (NDIR) spectrophotometer (PP Systems, UK, mod. EGM4). The change in concentration during the initial measurement is proportional to the efflux of CO_2 [Tonani et al., 1991; Chiodini et al., 1998]. Effluxes values are expressed in g m^{-2} d^{-1}. This is an absolute method that does not require corrections linked to the physical characteristics of the soil. We tested the method in the laboratory with a series of replicate measurements of known CO_2 effluxes. The average error was about ± 5%, the reproducibility in the range 200-1600 g m^{-2} d^{-1} was about 5%. Sampling points were at approximately 10 meters from each other (5 in the proximity of the main fault plane) and extend for 100 meters symmetrically to both sides of the fault plane.

3.4.1 Results and discussion

Soil ^{222}Rn and ^{220}Rn activity concentration, as well as CO_2 efflux values obtained at the sampling points, are shown in figure 3.8. Regardless of the side with respect to the main fault plane, the patterns of soil ^{222}Rn measured values are clearly similar, showing a very good agreement between the two active devices (correlation coefficient r = 0.99). Higher values were measured on the upthrown side of the fault (left part); in detail, ^{222}Rn activity concentrations on the upthrown of the SVF were, on

average, more than five times higher as those measured on the downthrown side, being the lowest ^{222}Rn values measured in close proximity of the fault. Moreover, a significant correlation was found between ^{222}Rn and ^{220}Rn data ($r = 0.87$).

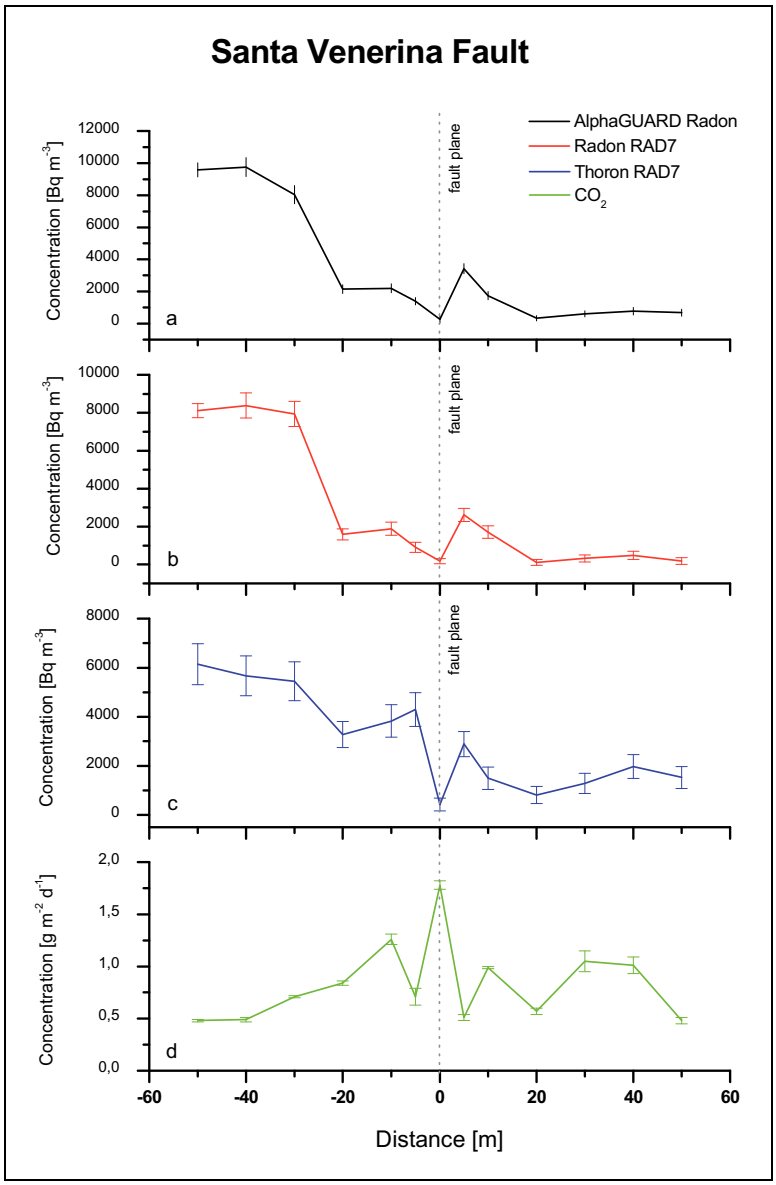

Figure 3.8 - Radon concentration along the SVF using a) the Genitron AlphaGUARD and b) the Durridge RAD7; d) Thoron concentration via RAD7 system; d) soil CO_2 efflux values measured along the profile.

The distribution of soil CO_2 efflux values along the profile is shown in the lower part of figure 3.8. Relative high CO_2 emissions were recorded on the fault plane, remaining

almost constant, on average, on each of two sides of the profile. A negative correlation was found between ^{222}Rn (and ^{220}Rn) and CO_2 concentrations (r = -0.48 and -0.47 respectively). It should be noted that, however, the CO_2 absolute values were not as high as might have been expected, since the measurements were performed during a period of strong, but often pulsating, degassing from the North- and South-east craters characterized, in the following days, by intense paroxysmal eruptive episodes and minor emissions of ash from the Bocca Nuova crater.

There are several conditions that affect soil ^{222}Rn activity concentration as measured in this study: *i)* the concentration of parent radionuclides present in the shallow subsoil; *ii)* the surface to volume ratio of the soil and subsoil clasts (a higher surface area to volume ratio will lead to higher efficiencies of escape of ^{222}Rn from the rock matrix; *iii)* both the average bulk permeability of the subsurface stratigraphy as well as the structure of that permeability; *iv)* the response of the soil column to moisture content (e.g. swelling soil/clays); and *v)* advection driven by gas phase transport from depth. Determining which of these conditions or phenomena are responsible for the differences seen between the upthrown and downthrown sides of the fault, without benefit of detailed stratigraphic data, is clearly impossible. However, we may reasonably suggest that differences in subsurface permeability, due to soil accumulation or ponding of lava flows, on the downthrown side of the fault could contribute to the lower average ^{222}Rn activity concentrations. Moreover, higher ^{222}Rn values measured on the upthrown side of the fault could be due to a peculiar mechanical behavior of the fault. The upthrown side of the fault, in fact, may be actually relatively "stable", while the downthrown side "mobile" and more fracturated. Likewise, differences in the advective gas transport in the upthrown and downthrown sides of the fault may be a contributing factor to the observed differences.

Moreover, the inverse correlation between radon values and soil CO_2 effluxes on the main fault plane would confirm a greater ground fracturing that allows dilution of radon, because the CO_2 flux is high enough to overwhelm the source of ^{222}Rn. Furthermore, ground fracturing due to tectonic activity adds up the already high soil permeability (10^{-6} - 10^{-7} cm^2) of the Etnean lava flows [Aureli, 1973; Ferrara, 1975]. As the

CO_2 decreases on moving away from the fault plane, the dilution of radon is no longer effective and so the radon activity concentration increases to its maximum (this effect is more evident in the upthrown side). On moving further away, both radon concentrations and CO_2 efflux should progressively decrease becoming more stable, as expected due to the decrease in soil permeability relative to the main fault plane.

In any case, the complexity of the problem in volcanic environments suggests that such approach may be useful for geophysical investigations aimed to the individuation of hidden faults, is not sufficient to carry out accurate studies on radon transport mechanisms in situ. In order to understand more about radon transport in porous fracturated media, we are upgrading this experimental technique, in the framework of a collaboration with Czech Technical University in Prague (Czech Republic), by means of geophysical investigations for imaging sub-surface structures from electrical resistivity measurements made by electrodes in boreholes (Electrical Resistivity Tomography). By the example in figure 3.9, which refers precisely to the Santa Venerina fault, it can be seen as the subsoil is far to be homogeneous, making this type of investigation, togheter with the application to other structures, extremely necessary in order to better understand the physical processes involved in radon transport.

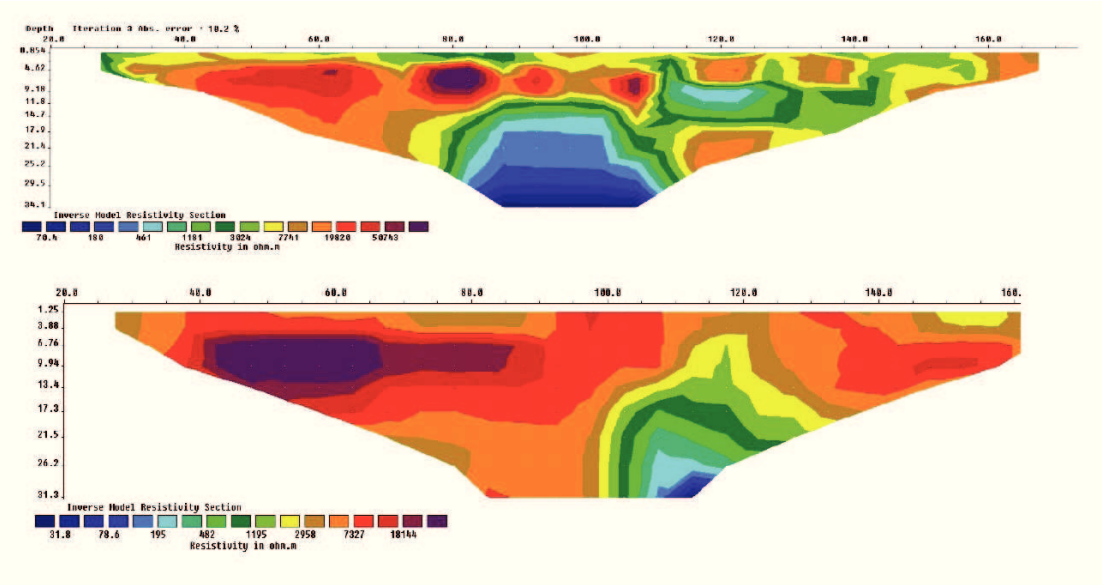

Figure 3.9 - Example of Electrical Resistivity Tomography at Santa Venerina Fault using dipol-dipol array (bove picture) and Schlumberger array.

3.5 In-soil radon vertical profile

More detailed information on some of the parameters that play a key role in radon transport mechanisms can be obtained by studying the in-soil radon concentration vertical profiles. Different measurements were carried out by means of solid state nuclear track detectors (SSNTD, CR-39 type) located inside a closed PVC tube (l = 100 cm, ϕ = 6.3 cm), uniformly pierced along all its length to allow the radon entry. The CR-39 were vertically located, at 20 cm intervals, from 20 to 100 cm, and, to avoid saturation effects, they were removed from the boreholes after 2 weeks.

Five different profiles were obtained between Vena, Cugno di Mezzo and Santa Venerina where, in particular, two boreholes were drilled along the horizontal profile at about 20 m from the fault plane both in upthrown and downthrown sides. Such profiles were obtained by using a different experimental technique in which the spaces between sampling points have been filled with the soil previously removed while making the borehole (figure 3.10). Moreover, unlike the first three profiles, two SSNTDs were placed at each height and no cover were placed to close the PVC tubes.

Figure 3.10 - Closed PVC tube introduced inside the borehole at Vena (left picture). Soil-filled PVC tube located in the vicinity of SVF (right picture).

3.5.1 Results and discussion

The solution of eq. (2.25), which describes mathematically the radon transport, is very difficult to solve exactly and analytically, except for very simple geometries and under simplified boundary conditions. The typical simplification generally adopted is to neglect one of the mechanisms of transport than the other, assuming a homogeneous and isotropic soil type respect to the diffusion, permeability, porosity and emanation coefficients, radium concentration and density. The most important factor in this assessment is the permeability of the soil. For soils with high permeability, transport due to diffusion can be neglected, while in cases of low permeability is the transport due to advection that can be neglected.

As discussed in section 2.5.3, the simplest solution and therefore also the most applicable is that which is obtained by studying the transport along the vertical profile, with the z axis perpendicular to the surface facing down. It is also assumed to be in a stationary state and in presence of an homogeneously radioactive field, in which case the concentration of ^{222}Rn in the soil pores C(z), as a function of depth, is given by (see also eq. (2.51)):

$$c_a(z) = c_\infty \left[1 - \exp\left(- z \sqrt{\frac{\lambda}{D}} \right) \right] \tag{5.1}$$

where c_∞ is the radon concentration at great depth, D is the diffusion coefficient of radon in the pores of the ground, λ is the radon decay constant and z is the depth. The radon vertical profile was determined by fitting measured concentration values to an exponential depth dependence [Jönsson, 2001].

Figure 3.11 shows the obtained radon concentration vertical profile, together with the exponential fit, for Vena, Cugno di Mezzo and Santa Venerina boreholes.

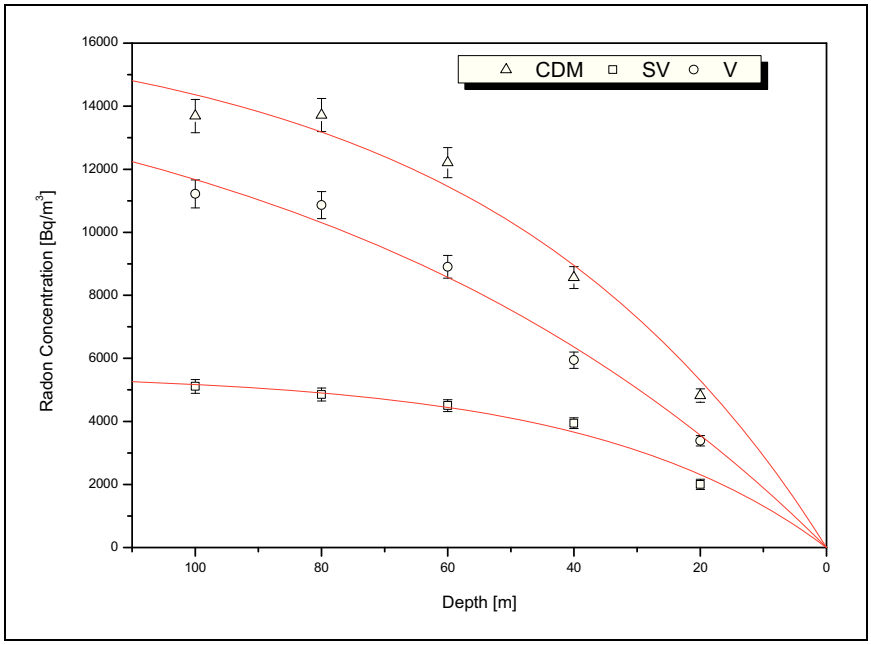

Figure 3.11 - In soil radon concentration vertical profile, together with the exponential fit, for three of the five sites of the etnean area.

The diffusion coefficients extrapolated by the fit and the radon concentrations at one meter depth reported in table 3.1, show corresponding higher values at higher altitudes above sea level, probably related to a major faulting.

Table 3.1 - Diffusion coefficients extrapolated by the fit

Site code	*Radon concentration [kBq m^{-3}]*	*Diffusion coefficient [10^{-7} m^2 s^{-1}]*
V	11 ± 0.4	14.3 ± 0.1
CDM	14 ± 0.5	16.0 ± 0.3
SV	5 ± 0.2	3.50 ± 0.01

The vertical distribution of radon in soil, here determined by measuring the concentrations at different depths under particular assumption of homogeneous and isotropic soil, was also estimated using the RnMod3d. Figure 3.12 and 3.13 show, respectively, the experimental data together with the results of simulations for the three above profiles of Vena, Cugno di Mezzo and Santa Venerina and the profiles in the close

proximity of the Santa Venerina fault at about 20 m in the upthrown and downthrown sides with respect to the main fault plane. Although we could not *a priori* estimate the advective flux, we rejected the assumption of pure diffusive radon transport and forced the model to $C(z=0)=0$ and $C(z_{max}) = C(z_{max})_{experimental}$.

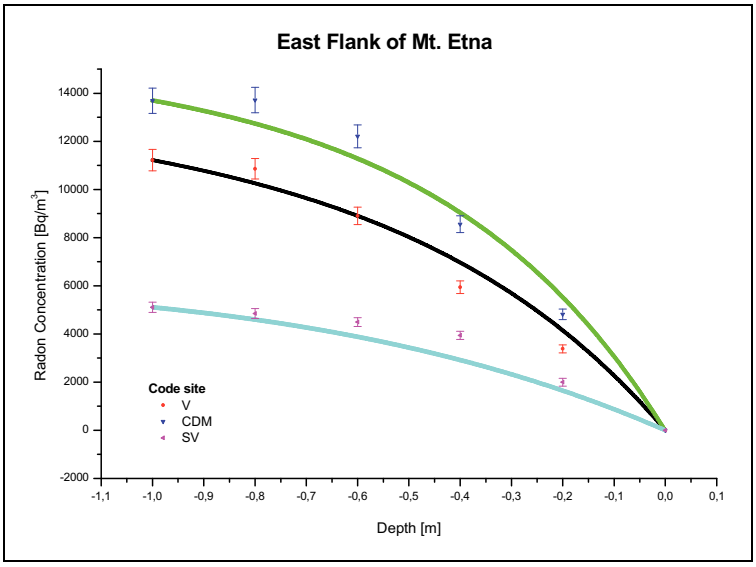

Figure 3.12 - Radon concentrations as a function of depth for V, CDM and SV profiles. Solid lines represent calculated values from the RnMod3d.

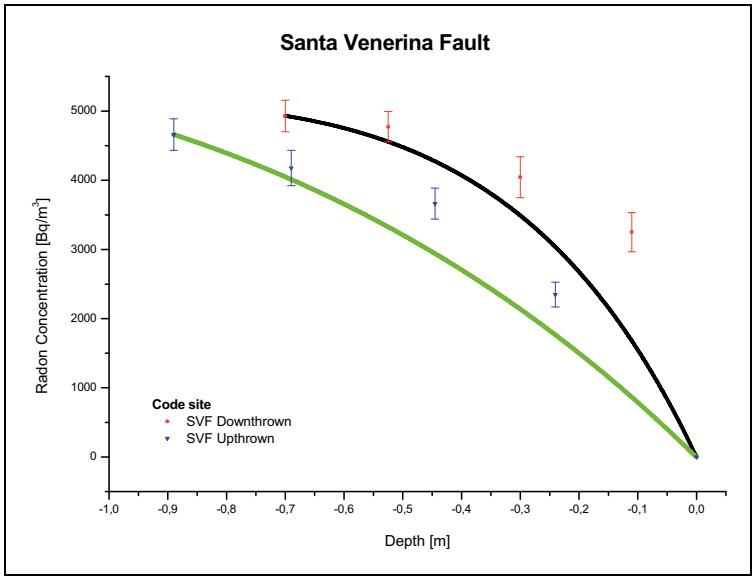

Figure 3.13 - Radon concentrations as a function of depth in the close proximity of SVF. Solid lines represent calculated values from the RnMod3d.

Generally, there is a quite good agreement between experimental data and the results from model calculations, especially for those profiles (V and CDM) in which, probably, the advective flux plays a minor role. The radon activity concentrations decrease exponentially from a constant value at the source in depth up to the surface. The decreasing rate depends on the permeability and porosity of the soil but it is well expressed using as a parameter the effective diffusion coefficient D, extracted by the fit by means of eq. (3.1). No other fit values of bulk diffusivity approximate the experimental data as well as the parameters in table 3.1 if we consider suitable values for disturbance pressures. Moreover, it can be noticed that for high values of the effective diffusion coefficient (V and CDM), constant values for the radon concentration seem to be obtained at greater depths, while in the case of low values of D (SV), more or less constant concentrations are already reached close to the soil surface.

Further evidences of what was said in section 3.4.1 arise from the profiles in the close proximity of the Santa Venerina fault where, at a given depth, lower concentrations are measured at the (more fracturated) downthrown side of the fault. Also in this case, the model calculations approximate quite faithfully the experimental data if, on the basis of the previous considerations, we consider for the downthrown side higher values of both soil permeability and bulk diffusivity, assuming a constant advective flux.

In order to understand more about the radon transport mechanisms in porous media, the approach that takes into account the vertical profile of radon concentrations in the ground is certainly more preferable than the previous one, since the informations we can take from horizontal profiles in more general non-fracturated soils, without a detailed tomography of the subsoil, are really poor. In any case, the complexity generated by the existence of a great number of uncontrollable parameters and processes affecting the production of radon and its transport in the source medium till its exhalation into atmosphere, requires a careful and systematic study in laboratory in which we can vary and keep under control each single parameter.

Chapter 4

Experimental set-up and procedure

The study of the radon transport mechanisms in porous materials is extremely complex if approached only with *in situ* measurements, because of the great number of uncontrollable and varying parameters (physical, geological, meteorological) involved in the processes. Therefore, laboratory measurements were carried out on radon transport under well-defined and controlled conditions and the results were compared with those expected by the radon-transport model presented in chapter 2. For this purpose, a laboratory facility was built which consists of a large cylindrical vessel with inserted measuring 'probes' that allow measurement of radon concentration in the pore spaces of the soil at various depths. The vessel, installed in the Environmental Physics Laboratory of the Department of Physics and Astronomy (University of Catania), has been filled with four different materials in order to simulate different type of soil. Their narrow grain-size distribution and small transition range from saturated pores to dry pores in a partly water-saturated column approach relatively simple conditions. In view of the research strategy of starting with simple conditions and increasing the complexity step by step, these materials are the optimal choice of soil type for this study of radon transport.

The laboratory facility will be described in section 4.1, followed by a description of the procedures and equipment for measuring the pore-air radon concentration. Finally, the properties of the materials that are of importance for radon transport are discussed, together with the computer code developed to run the model.

4.1 Laboratory facility

The laboratory facility, shown in perspective in figure 4.1, consists of a cylindrical stainless steel vessel (height 1.25 m and diameter 0.5 m) with a lateral opening (diameter 0.3 m) that allows the removal of materials from the column.

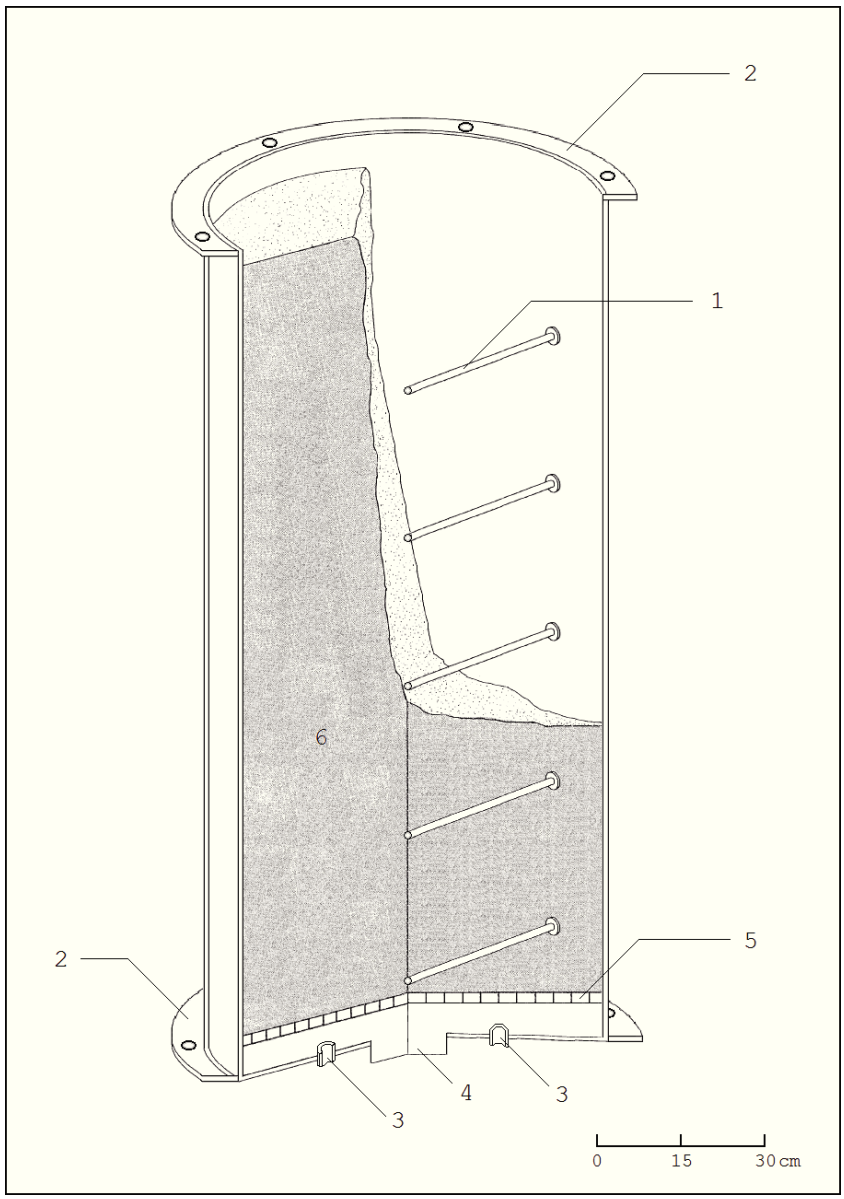

Figure 4.1 - Schematic presentation of the radon vessel. 1) probe; 2) flange; 3) air inlet/outlet; 4) housing for radioactive source; 5) perforated plate; 6) soil.

The vertical dimension of the vessel is of the order of the diffusion length of radon in dry soil, 1-2 m. It is an optimization of reducing boundary effects. The vessel can be closed by screwing a stainless steel lid into the upper flange in such a way that, when the vessel is filled with sample material, the space under the lid approaches a crawl space in radon entry into houses simulations. In figure 4.2 a vertical cross-section of the vessel through the symmetry axis is shown.

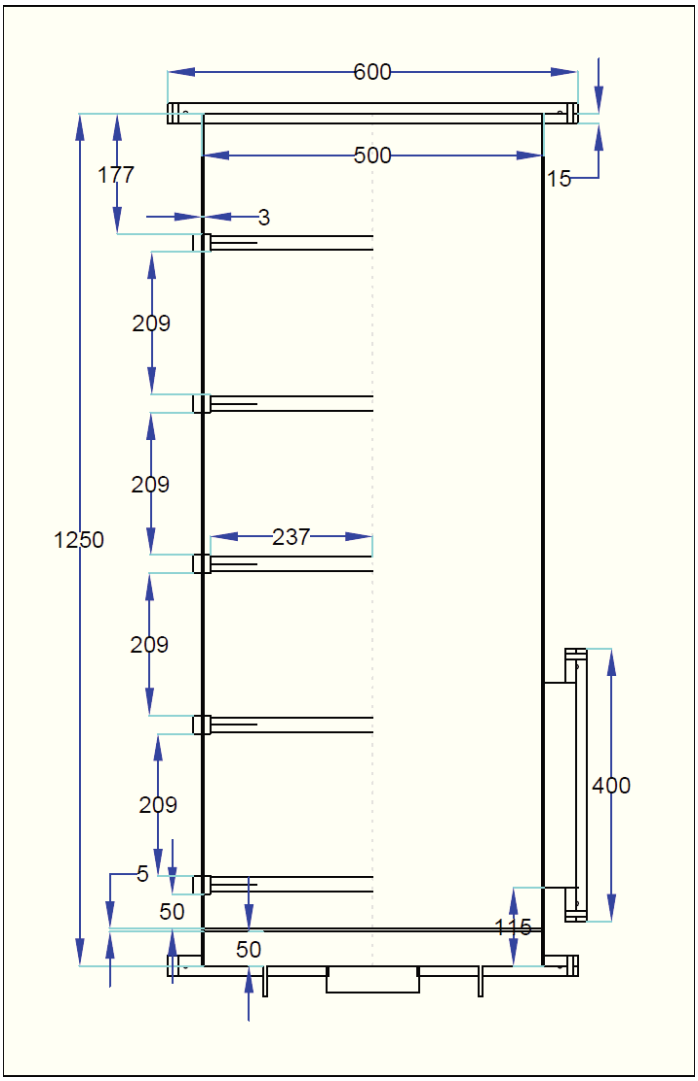

Figure 4.2 - Vertical cross-section of the radon vessel through the symmetry axis. Dimensions are given in millimeters.

The vessel has been oriented such that the tilt angle of the symmetry axis of the vessel is less than 0.5°, according to [Van der Graaf, 1992; van der Spoel, 1998]. Considering other deviations from the ideal situation of a cylindrical symmetric column, the error induced by a possible tilt is negligible.

At five different heights flanged ports are welded in the vessel wall and five 23.7 cm long sleeves are mounted on these flanges. They penetrate the vessel at distances of 18.9, 42.2, 65.5, 88.8 and 112.1 cm below the upper rim and allow, after filling of the vessel with sample, the entry of probes to measure temperature and humidity at the centre of the column. For determining the vertical profile of radon concentration, an appropriate stainless steel adapter can be screwed to the rear-end of each flange in the outer part of the vessel to reduce the diameter of the sleeve from 1.4 cm to 0.6 cm. In this way, pore-air surrounding the sleeve in the inner part of the column may be sampled from the soil, by drawing air by means of a pump if necessary, and conveyed directly to a radon detector through small diameter silicone tubes.

For the study of pressure-driven radon transport, a stainless steel slab (diameter 0.5 m, height 3 mm) consisting of a perforated plate (pitch 0.5 cm) laid on a circular ring, in turn welded inside the vessel, is placed at a distance of 1.2 m below the sample surface and at just 5 cm from the first sleeve. This perforated plate has a very important task, at least for a couple of reasons: first of all, it supports the heavy column of overlying material (under full load conditions its weight ranges from 350 to 450 kg depending on the density of the sample); on the other hand, the holes allow to perform experiments with advective flux, favoring both upward forced ventilation and, if an underlying radioactive source of radon is used, ^{222}Rn entry in the column. As a result, air and radon originating from below the perforated plate can practically only enter the sample by transport through the holes.

The bottom of the vessel is closed with a flange equipped with two inlet/outlets (diameter 0.6 cm) symmetrical to the axis of the container, through which the air can be introduced in or removed from. If pure diffusive experiments are performed and no external radioactive source is used, this openings may be closed to prevent leakage of radon. In the bottom lid, exactly at the centre of the vessel, there is also a circular

compartment (diameter 15 cm) specifically designed for housing radioactive sources within the vessel. Figure 4.3 shows the laboratory facility highlighting, in particular, some of the construction details described in this section.

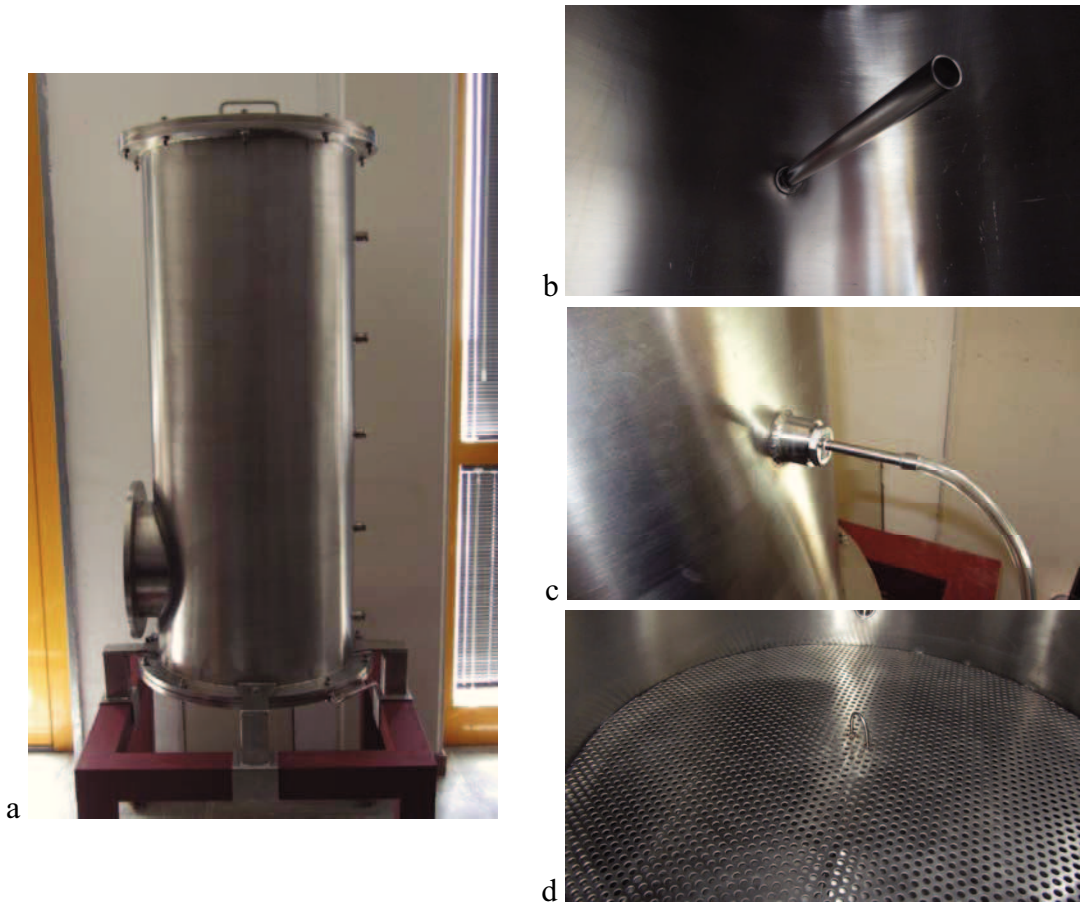

Figure 4.3 - a) Cylindrical stainless steel AISI 304 vessel. Note, on its left side, the lateral opening for removing the materials inside the vessel and, on the right, the five flanged ports; both the upper and lower lids are closed. b) One of the five sleeves mounted on the flanged ports, viewed from the inner part of the vessel. c) Stainless steel adapter screwed to the rear-end of each flange; it reduces the diameter of the sleeves from 1.4 cm to 0.6 cm. d) Perforated plate that allows both upward forced ventilation and radon entry from the radioactive source to the sample.

4.1.1 Radon concentration determination

Radon concentrations in the pore-air of the sample column were generally measured by air sampling through the five sleeves. By conventionally assigning a position from 1 to 5 to the sleeves, from the lowest to highest, sampling is normally started at positions 1,3 and 5 and subsequently at 2, 3 and 4. This procedure allows determination of the radon vertical profile in the material sample. A short, small diameter silicone tube is connected to the adapter on the rear-end of each flange and conveys the sampled air into active detection AlphaGUARD devices (described in section 3.3.1) which allow both short and long term analysis.
Since we used a natural radioactive radon- and thoron-rich source to perform our radon transport study (see section 4.2), it is worth estimate thoron contribution. Thus, in order to continuously monitor thoron concentration that enters the vessel, in our experiments the AlphaGUARDs, that does not discriminate radon and thoron alphas, are always coupled to a monitor RAD7 (see section 3.3.2) that discriminate them..

4.1.2 Temperature variations

Temperature is one of the physical parameters that may most affect the vertical profile of radon concentration inside the vessel. In order to assess its role on radon transport mechanisms in porous media, experiments were performed under well-defined and controlled conditions of temperature by means of a set-up consisting of five heating bands, a PID controller and three solid state contactors (figure 4.4).
The heating bands, manufactured according to our specifications by Lorenzoni s.r.l., Italy, are special etched-foil heaters with silicone insulation formed by chemically etching out a resistive circuit of nickel alloy, provided with hooks to enable the fastening around the laboratory facility. Their high flexibility and adaptability to curved surfaces, the good thermal distribution over the whole heating surface and the reduced thickness made these bands particularly suitable for our purposes.

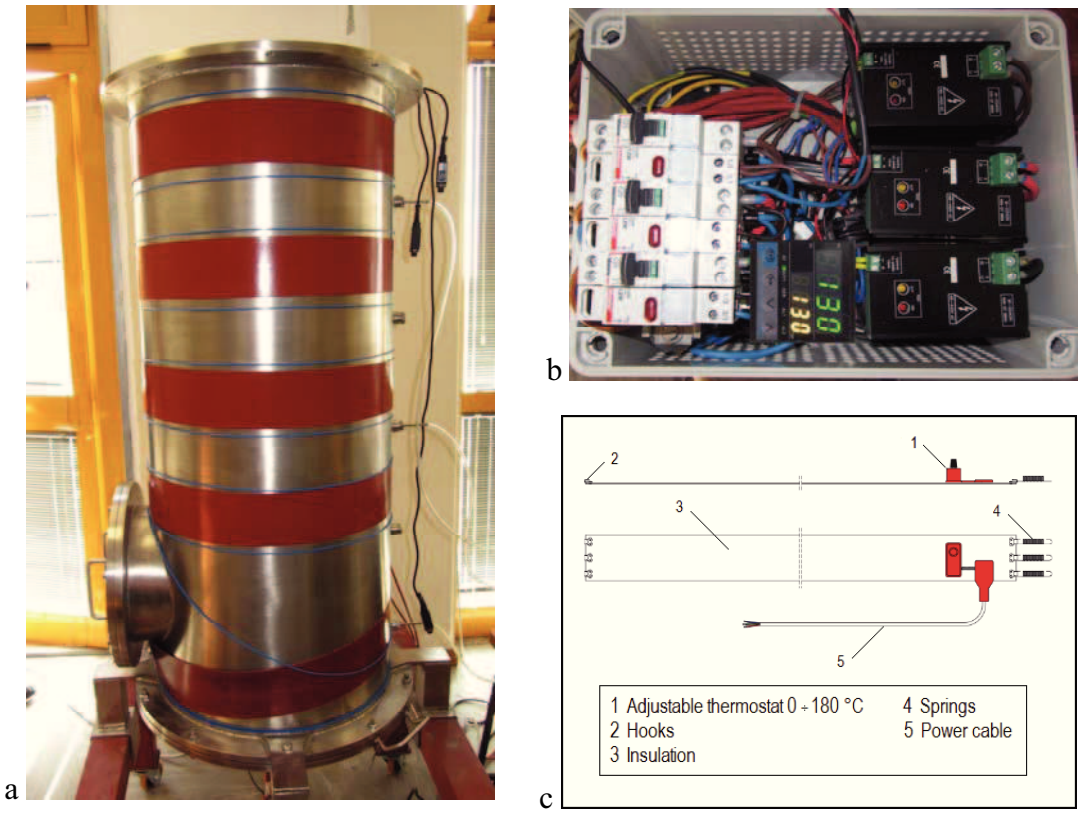

Figure 4.4 - a) Heating bands for temperature variations; b) control unit; c) heating band technical drawing.

The technical specifications of the heating bands are reported in table 4.1.

Table 4.1 - Heating bands technical data

Insulation	Silicone
Working temperature	-30 °C ÷ +180 °C
Insulation minimum thickness	0.4 mm
Supply voltage	24 V ÷ 400 V
Max specific charge	2.0 W/cm^2
Dimensions	1710 x 100 mm, Ø = 570 at 230 V 1500 W
Tests	EN 60335-1, EN 50106

To accurately control the process temperature, a control system relies upon a resistance temperature detector (Pt100 type) as input, connected to a proportional-integral-derivative (PID) controller which corrects the error between a measured process tem-

perature and the desired setpoint. A static zero-crossing three phase relay, endowed with the necessary heat sink, receives AC control signal from the PID controller and provides for keeping constant the temperature of the electric heaters by means of very frequent on/off cycles. A thermal barrier coating, consisting of a sheet of rock wool (thickness 10 cm) wrapped up around the vessel, serves to insulate the system.
The temperature (and the relative humidity) at the sampling points was measured before each measurement with a thermocouple humidity/temperature combined probe (model HP475AC) connected to a hygro-termometer (model HD2301.0) by Delta Ohm s.r.l., Italy. The head of the probe has a stainless steel terminal tip (13.5x75 mm) to facilitate its penetration into the material sample.

4.2 Radon source characterization

In order to identify the proper radon source to be used in our experiments, some man-made radioactive sources of ^{226}Ra were placed inside the housing in the bottom of the vessel, but we did not obtain any appreciable amounts of radon inside the vessel. Thus, to ensure high radon fluxes into the sample, it was decided to opt for a natural source, obtained, on the basis of careful analysis on its radionuclides content, from under ground near the laboratory. To extract the pore-air from this under ground source, we used a soil gas unit consisting of a capillary probe and a drilling rod with an exchangeable drilling tip with air-lock which is closed by a rivet. The drilling rod is hit at 1 m depth into the ground and the capillary probe is inserted into the drilling rod. The higher part of the capillary probe is connected to an aqua stop filter, in order to eliminate as much as possible the moisture, then to a progeny filter that let only the ^{222}Rn and ^{220}Rn pass. The system is connected to the laboratory facility by means of a pump, whose aspiration rate can be set between 0.1 and 3 liter/min, and a 35 meters long rubber tube with a diameter of 0.6 cm (figure 4.5).

Figure 4.5 - Drilling rod hit at 1 meter depth into the ground (left picture) and pump to convey the soil gas into the laboratory facility (right picture).

Some tests were carried out in order to characterize the radon source. Preliminarily, we have determined the natural radionuclides (^{238}U, ^{232}Th and their decay products, especially ^{226}Ra) content in the soil sample by gamma spectrometry technique using high-purity germanium (HPGe) detector.

After oven drying, the sample was gently ground and passed through a 250 μm sieve. Almost 1 kg of meshed soil sample was transferred to a Marinelli beaker of 1000 ml total capacity, which represent the best configuration to provide higher detection efficiency, and sealed for 30 days to allow secular equilibrium in the uranium and thorium series.

The activity of ^{238}U and ^{232}Th cannot be directly determined, since these isotopes emit, respectively, only weak (0.064%) γ-rays at 49.55 keV and α-particle at 4.083 MeV (100%), but any of its γ-emitting daughters could be used for this purpose. For uranium daughters the energies are at 92.8 keV from ^{234}Th, 186.2 keV from ^{226}Ra, 295.2 and 351.9 keV from ^{214}Pb, 609.3 and 2204.2 keV from ^{214}Bi while the gamma-ray peaks of ^{232}Th are at 911.1 and 969.1 keV from ^{228}Ac, 238.6 keV from ^{212}Pb and 583.1 keV from ^{208}Tl. It has been neglected the emission of ^{234m}Pa at 1001 keV because, although this γ-ray does not interfere with other emissions and is practically free from self-absorption effects, because its low emission probability (0.835%) makes it inappropriate for the analysis of soil samples in which uranium activity typically amounts to less than 100 Bq/kg. The activity concentration of ^{40}K was also determined from the peak area of its own gamma rays line (1460.81 keV).

In this study, we used a p-type HPGe coaxial detector (GMX-15185-P POP-TOP, EG&G Ortec), with a crystal diameter of 49.3 mm and length of 47.1 mm. The resolution and the relative efficiency at ^{60}Co 1332.5 keV gamma-ray are 1.79 keV and 25% respectively. The detector and its preamplifier are allocated in a cylindrical lead shield to reduce the background and cooled by LN_2. Standard nuclear electronics was used and the spectra were stored for analysis in 8192 channels MCA system. The spectrum measured with the gamma-ray detector with a measuring (live) time of 24 hours is shown in figure 4.6. It shows, among others, the 186.2 keV gamma-ray from ^{226}Ra, the 609.3 keV gamma-ray from ^{214}Bi, and the 911.1 and 969.1 keV gamma-rays from ^{228}Ac.

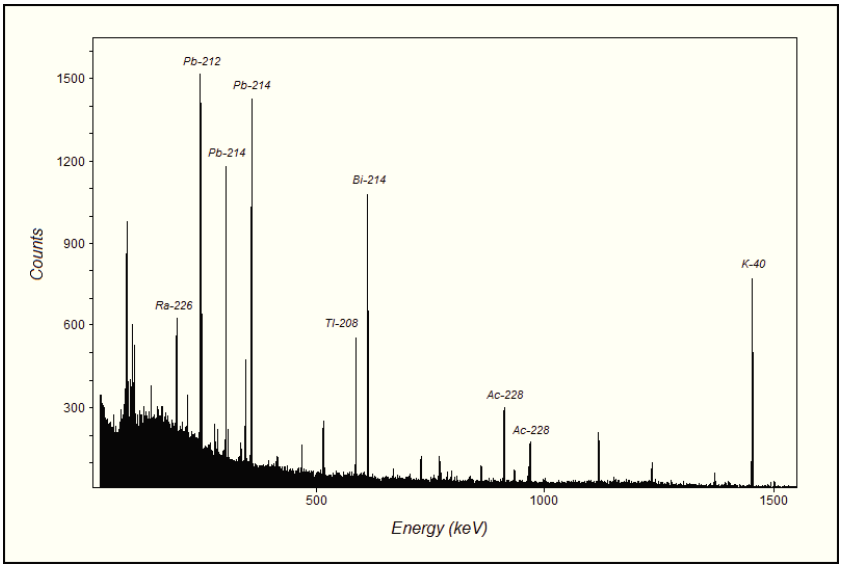

Figure 4.6 - Spectrum (8192 channels) taken with the low-background γ-ray detector ORTEC GMX-15185-P for a measuring (live) time of 24h.

Table 4.2 shows the activity concentrations in Bq kg^{-1} for ^{238}U and ^{232}Th series decay products and ^{40}K. The activity concentration for each radionuclide was determined using the total energy under respective peaks after applying appropriate factors for peak efficiency and self-absorption corrections.

Table 4.2 - Radionuclides activity concentrations in soil sample

Radionuclide	*Concentration [Bq kg^{-1}]*
Ra-226	*26.8 ± 0.9*
Bi-214	*41.7 ± 0.5*
Pb-214	*38.4 ± 0.6*
Ac-228	*31.3 ± 1.0*
Pb-212	*23.9 ± 0.3*
Tl-208	*17.5 ± 0.2*
K-40	*484.0 ± 5.7*

In order to establish radon and thoron contribution from our radioactive source, a separate determination of the two isotopes was performed.

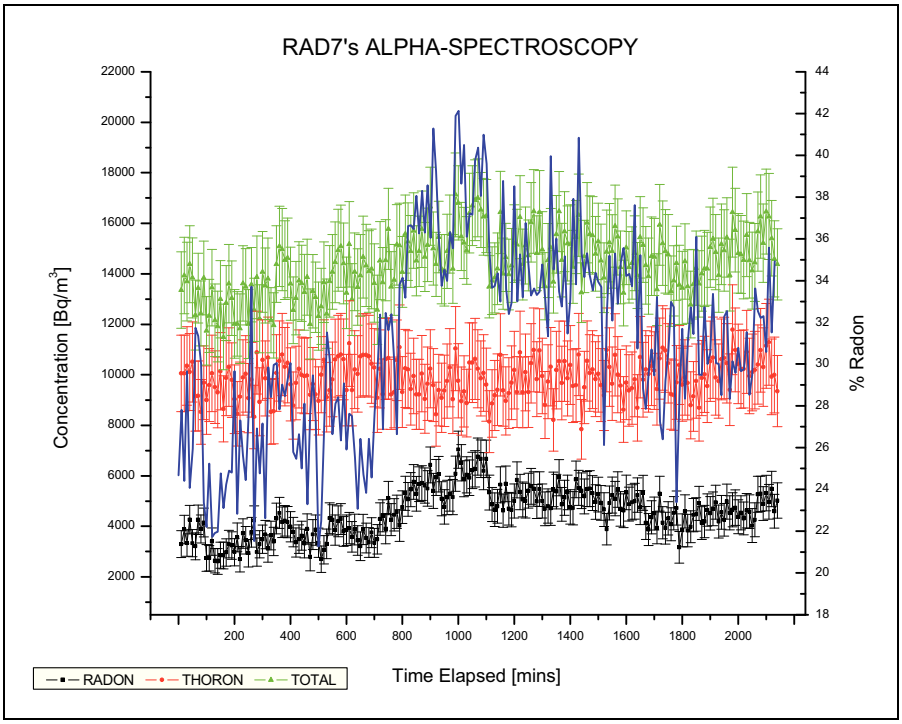

Figure 4.7 - Radon/Thoron discrimination with RAD7 detector.

Figure 4.7 summarizes the results of radon/thoron discrimination with the RAD7 detection system. Higher (and more or less constant) concentrations were seen for thoron time series (in red) while remarkable variations, up to a factor of 2, characterize the radon trend (in black). Consequently, large variations in the percentage of radon (blue line) to respect to the total (green line) were observed, from 20 to 42%. Hence the importance to continuously monitor the isotopes ratio in all our measurements as well as the need to identify a material which reduces significantly the amount of thoron that enters the vessel (see section 4.2.1).

4.2.1 Thoron attenuation inside the vessel

Since we were interested only in radon transport, taking into account the high contribution arising from thoron activity concentration (between 60 and 80% of the total, see figure 4.7), we interposed a filter which acts as a barrier for thoron transport from the under ground into the sample inside the vessel and therefore may reduce the thoron concentration inside the vessel.

A very high density (approx. 155 kg/m^3) circular slab of glass-wool (0.5 m diameter, 5 cm thickness) was placed above the perforated plate and just below the first sleeve in direct contact with the sample inside the vessel. The slab is assumed to be almost completely permeable for air flow and contain no detectable radium. An additional advantage of the glass-wool filter is that allows the air to radially diffuse inside the stainless steel cylinder so as to ensure a flow as uniform as possible along the horizontal direction. To obtain an indication about the effectiveness of the glass wool filter as a barrier for thoron transport, a simple experiment was carried out by flushing radon- and thoron-rich air at a flow rate of 0.8 liter/min from the under-ground into the vessel. Therefore, equilibrium radon and thoron concentrations in the sample (volcanic sand, see section 4.4) were measured with the upper lid closed. First of all, measurements of both radon isotopes were performed by means of the RAD7 system outside the vessel, in order to assess the amount of radon and thoron that may be transferred, through the filter, within the vessel. Then, the same measurements were

repeated inside the vessel, starting at the lower sleeve (1) and subsequently at upper ones (2-5). Figure 4.8 shows the results of this analysis and compares the radon (in black) and thoron (in red) activity concentrations profiles passing through the glass-wool filter.

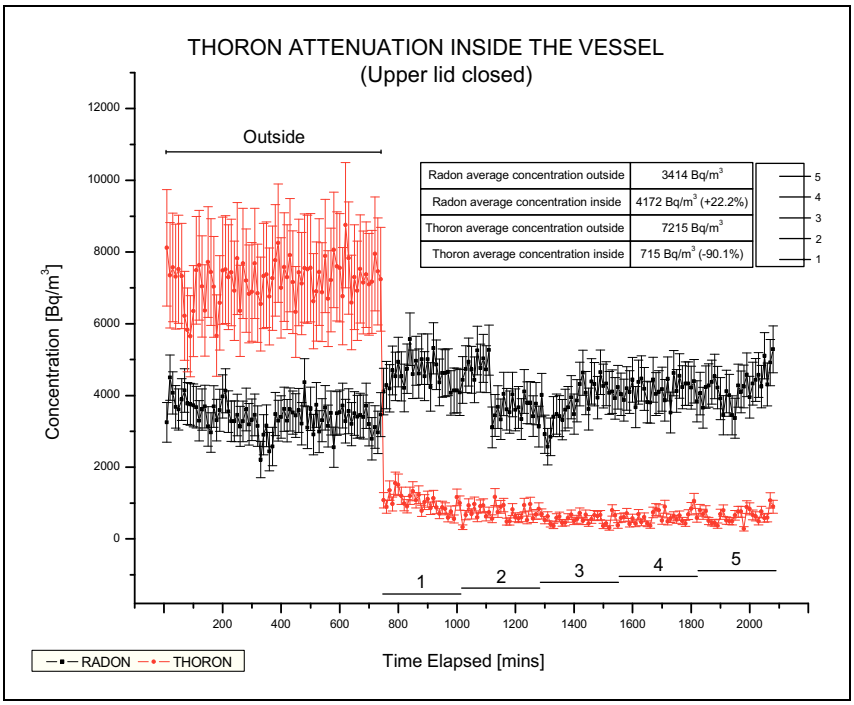

Figure 4.8 - Thoron attenuation inside the vessel

According to expectations, the average activity concentration of thoron sharply decreases of an order of magnitude from 7215 ± 67 Bq/m^3 to 715 ± 22 Bq/m^3, remaining almost constant with height. In terms of percentage decrease, passing through the glass-wool slab, the activity concentration is reduced by 90% showing the effectiveness of the filter to reduce the contribution of thoron from the under ground source (also considering the radioactivity in the sample material inside the vessel).

The situation is totally different for the case of the isotope of interest in the present study, where the measured average activity concentration even increases from 3414 ± 46 Bq/m^3 up to 4172 ± 46 Bq/m^3, corresponding to a percentage growth of over 20%. This behavior, similarly to as already mentioned above for thoron concentration, is

most likely due to the radon contribution arising from the sample within the vessel; in any case, the fluctuations typical of natural sources, together with small but measurable air fluxes at the five sleeves, assure that the major contribution comes from the under ground source. Clearly, unlike what happens for the thoron, the glass wool filter does not inhibit the radon transport proving to be an extremely useful tool for our experiments.

4.3 Radon detectors intercalibration

In order to ensure the quality of the measurements and provide a correct interpretation of the experimental data, an intercalibration analysis for radon detectors was performed by means of a series of measurements using the natural radioactive source.

During the first comparative test, an analysis of radon concentration time series, monitored at 10 minutes intervals over periods of 24 hours, was performed in order to evaluate the 'qualitative' response of the detectors, henceforth called RAD7, AG1274, AG1534 (from their S/N) and AGREF (for AlphaGuard REFerence). The radon data were collected, outside the vessel, connecting the available detectors in series, always placing the RAD7 and the AGREF in the first and third position of the chain respectively and the AG1274 and AG1534 alternatively before and after the reference device. For each configuration (RAD7-AG1274-AGREF-AG1534, RAD7-AG1534-AGREF-AG1274) we applied a simple technique to compare the datasets, based on the correlation analysis of the time series to ascertain if they contain similar features. Figure 4.9-4.12 show the result of this intercomparison. Radon time series exhibit a complex temporal structure and large variability on activity concentration, due to the non-uniformity of the source. It is evident, however, that the radon series measured by the different devices are well correlated (with correlation coefficients between 0.79 and 0.93 if we consider only the AlphaGUARDs and of 0.41 and 0.63 taking into account the different detection systems) and that the differences in the total activity concentration measured with AlphaGUARDs reproduce the radioactive decay of radon passing

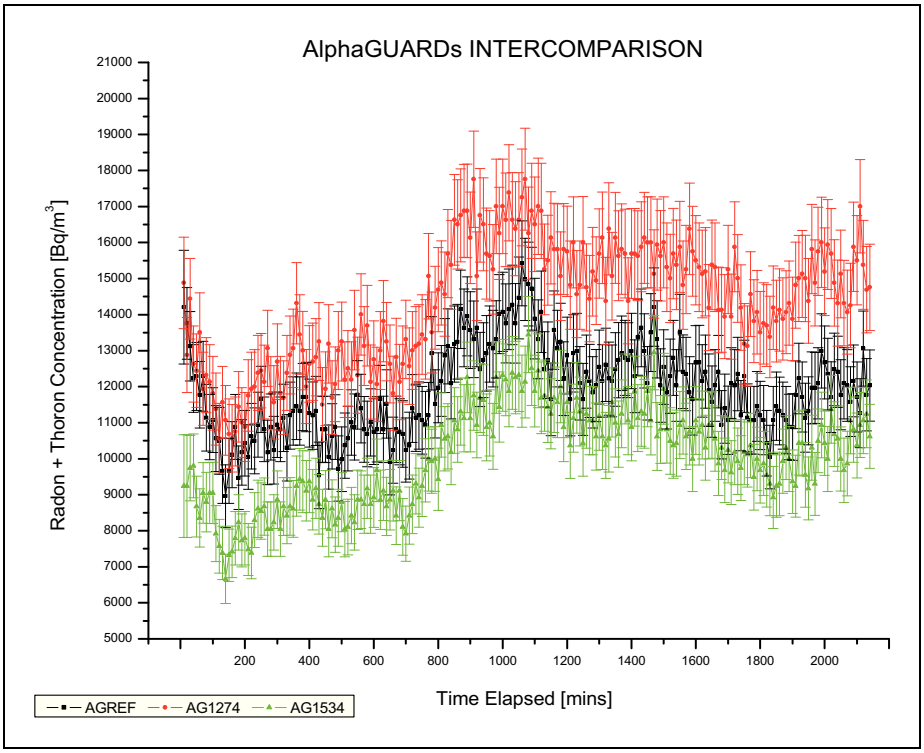

Figure 4.9 - Temporal variations of radon measured with AlphaGUARDs (configuration RAD7-AG1274-AGREF-AG1534).

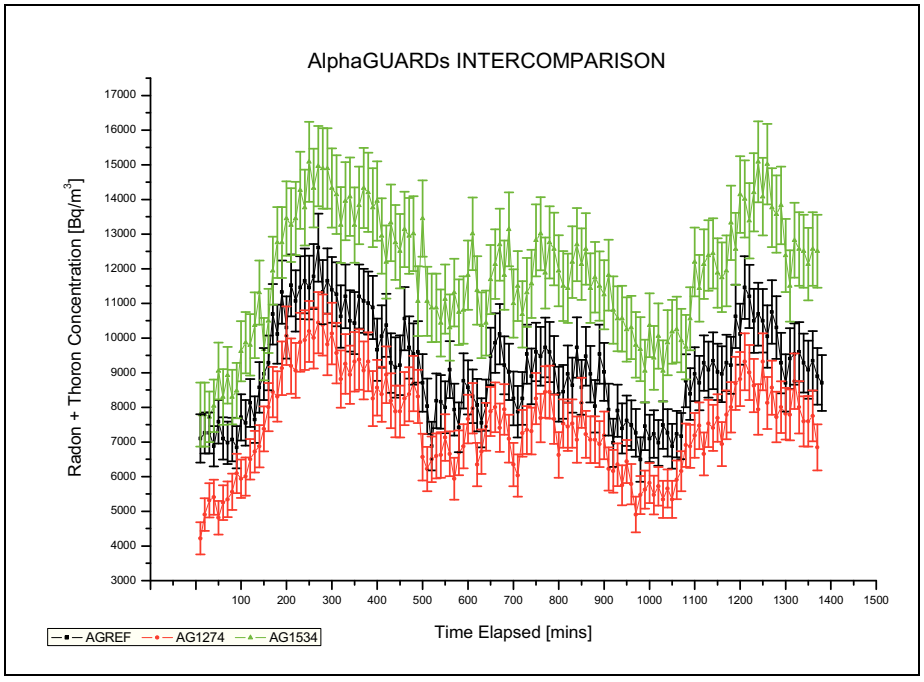

Figure 4.10 - Temporal variations of radon measured with AlphaGUARDs (configuration RAD7AG1534-AGREF-AG1274).

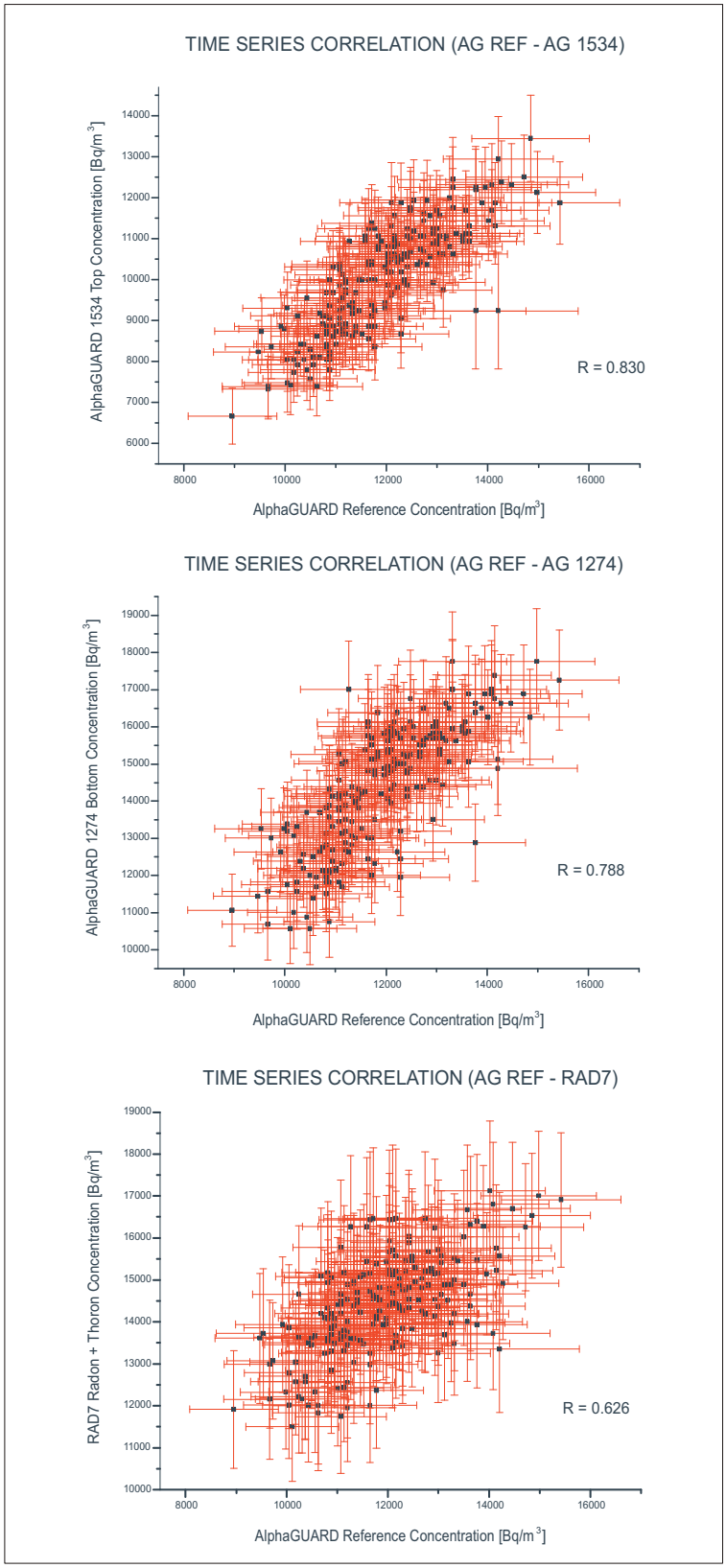

Figure 4.11 - Time-correlated response of the detectors (RAD7-1274-REF-1534).

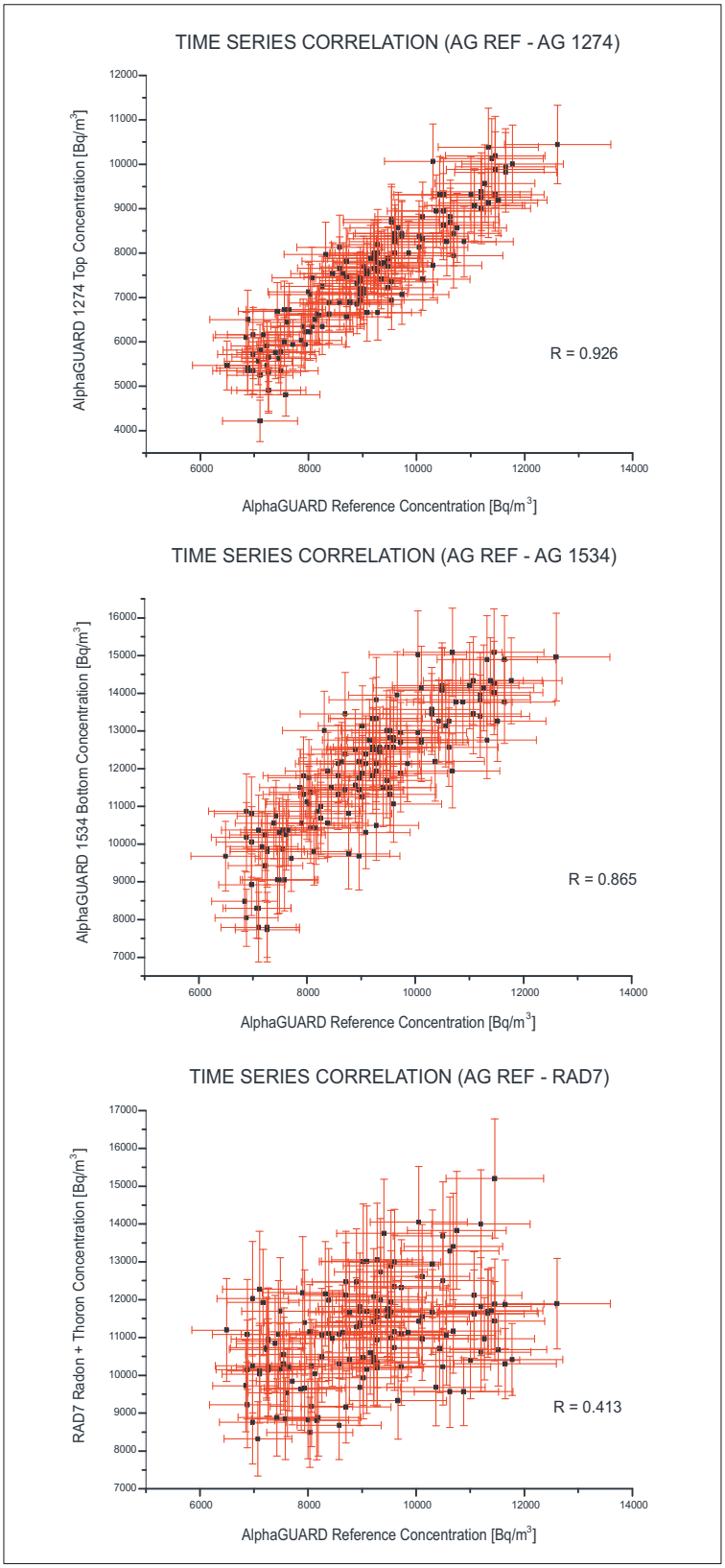

Figure 4.12 - Time-correlated response of the detectors (RAD7-1534-REF-1274).

successively through the three detectors (mainly thoron due to its short half-life). This behavior is confirmed by inverting the order of the devices as reported in figures 4.9 and 4.10.

In order to assess the degree of correlation of the respective outputs, we need to normalize each detector with respect to a reference device. Simultaneous measurements of both radon isotopes were carried out, using each detector and the reference one, by sampling air in close proximity from the under-ground source (setting flow at 0.1 liter/min).

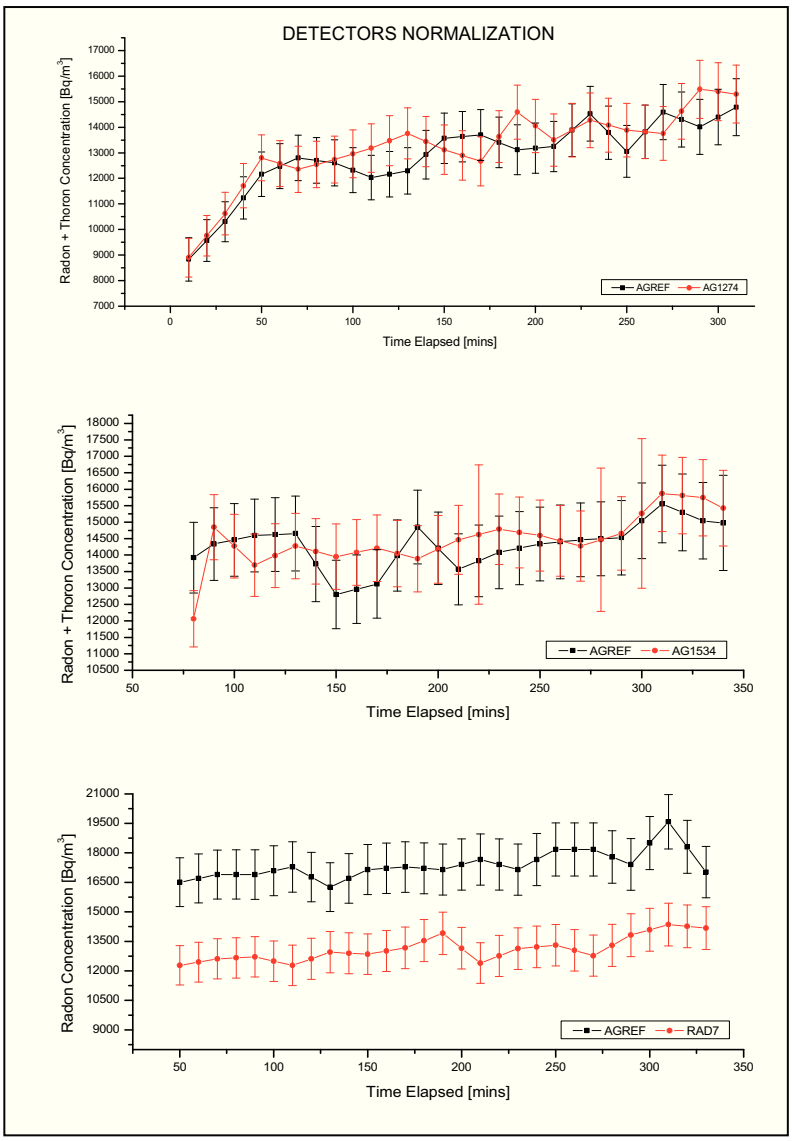

Figure 4.13 - Intercomparison between radon detection systems.

Figure 4.13 shows the results of this intercomparison. In general, there is a quite good agreement between the four devices, even if the RAD7 (figure below) seems to underestimate the total (radon and thoron) concentration. The normalization factors were estimated to be 0.977, 0.982 and 1.327 for AG1274 (above picture), AG1534 (in the middle) and RAD7 (below picture) respectively.

Moreover, we have to note that, before starting each new measurement, the detectors need a lapse time both to avoid influence from the previous measurement and to reach a stable concentration value. To define this lapse time, measurements were performed at a flow rate as low as possible (0.03 liter/ min) and the increase in radon concentration was drawn as a function of time, allowing us to individuate the 'starting point' (figure 4.14).

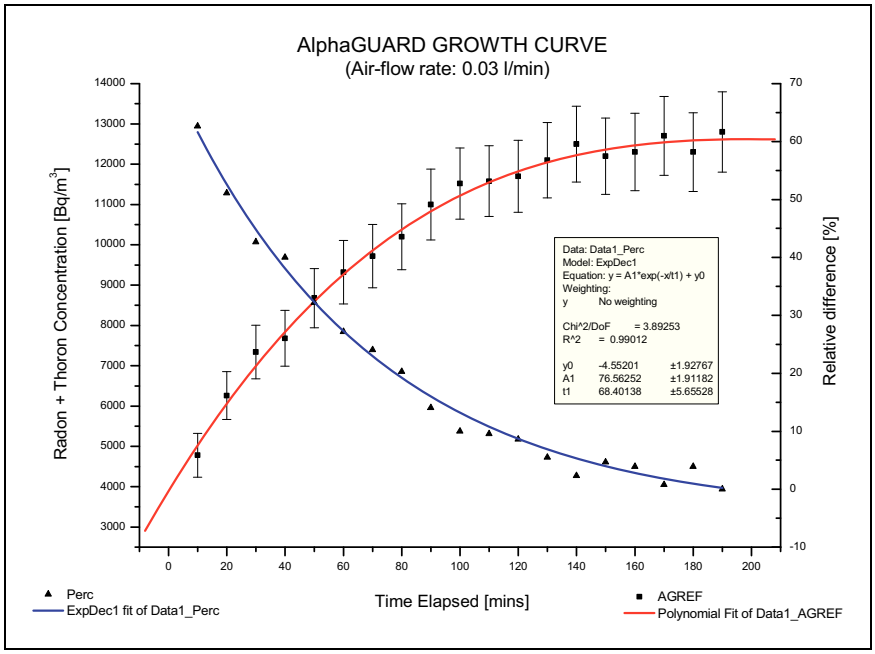

Figure 4.14 - Example of radon concentration increase with time (red line) and corresponding relative difference with respect to the maximum measured value of activity concentration (blue line).

By analyzing the relative differences within each set of data in properly selected time windows, in which we could reasonably assume that the radon activity concentration in the ground did not vary significantly, we identified the time from which the mea-

sured values remained constant within 3%. This time, estimated in about 100 minutes on the basis of the experimental results arising from different measurements of radon activity concentration in the under ground, represents the starting time to begin data acquisition.

Finally, the overall quality of this intercalibration was verified by comparing the experimental data from RAD7 and AGREF.

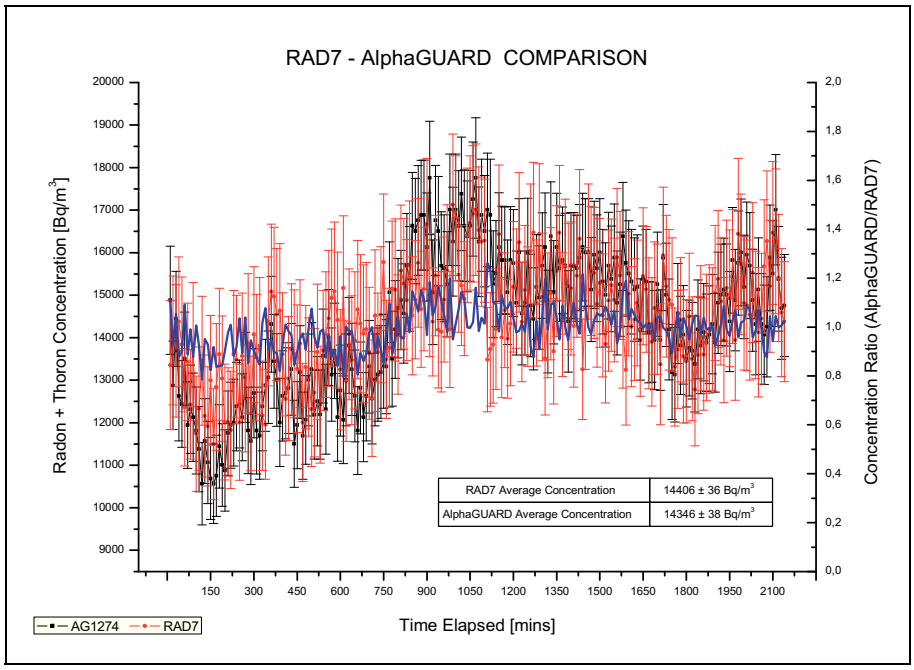

Figure 4.15 - RAD7-AGREF comparison after intercalibration corrections.

Figure 4.15 shows the time series after applying the 'corrections' for response time and normalization factor, together with the AGREF/RAD7 concentration ratio (blue line). The measured average total (radon and thoron) activity concentrations (14406 ± 36 Bq/m^3 and 14346 ± 38 Bq/m^3 for RAD7 and AGREF respectively) are each other comparable within the experimental errors (calculated as their SEMs), indicating good precision and accuracy of measurements and, accordingly, reliability of our radon analysis procedure.

4.4 Material properties

Different properties of the materials, important for radon transport and radon generation have been measured. In principle, referring to eq. (2.25), for the study of radon transport in porous materials it is sufficient to know the partition-corrected porosity and the radon production rate as well as the radon concentration in the air-filled parts of the pores. However, it is more constructive to analyze the radon production rate on the basis of more elementary quantities like density, radon emanation coefficient and radium content. For example, conditions like water content and compaction of the samples are directly related to changes of the emanation coefficient and (air-filled) porosity, respectively. Therefore, these basic parameters will be used in the analysis instead of only the radon production rate.
In this section, the experiments for determining the properties of the sample materials (marble sand, volcanic sand, volcanic rock and clay) that are of importance for radon transport are briefly discussed.

4.4.1 Grain size, density and porosity

The grain-size distribution was measured by dry sieving. The results, presented in figure 4.16 for volcanic and marble sands (for volcanic rock and clay, impossible to sift, we assumed sizes between 18-25 mm and 8-20 mm respectively), show that the mass fractions are distributed around 120 μm and 65 μm with a slightly longer tail to smaller and larger diameters respectively. Assuming a lognormal distribution (the hypothesis of a lognormal distribution cannot be rejected using a significance level of 5%) the estimated values for the geometric mean and geometric standard deviation are 123 μm and 1.4, 64 μm and 1.7 respectively for the two samples.

The porosity ε was determined using the mass increase of a dry cylindrical sample (height 21.6 cm; diameter 14.6 cm) due to water saturation. It was observed that saturating and drying the sample several times compacted the powdered samples notably. For example, a dry volcanic sand sample with an initial porosity of 0.12, could

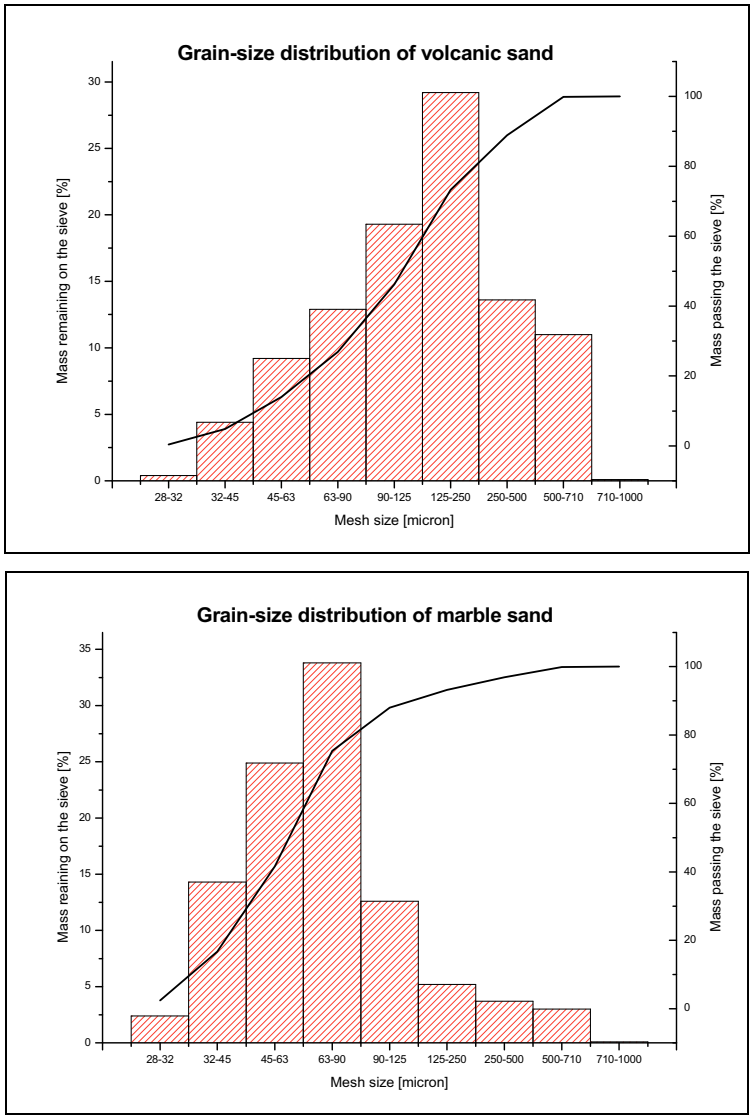

Figure 3.20 - Grain size distribution of the volcanic sand (above picture) and marble sand (below). Bars indicate mass fraction remaining on the sieve with corresponding mesh size (left vertical axis); black curves connects data point indicating the total mass fraction passing the sieve (right vertical axis). Sieving was carried out on a minor part representative of the whole samples.

finally attain a porosity of 0.09. Since the in the laboratory measurements temperature variations were induced inside the vessel, resulting in large changes in moisture content from 0 up to about 13-15% in the center of the laboratory facility, such compaction probably also occurred during our radon transport experiments. Moreover, the weight of the samples on top may have amplified such compaction of the samples at the bottom. In the light of these considerations, it was reasonably decided to consi-

der porosity values the low once in the measured ranges: 0.10 ± 0.01 for volcanic sand, 0.21 ± 0.01 for volcanic rock, 0.11 ± 0.01 for marble sand and 0.34 ± 0.02 for clay.

For an accurate determination of the specific density (mass per unit solid phase), a 500.00 ± 0.25 ml volumetric flask was partly filled with a quantity of sample material with mass M_s (kg) and subsequently filled up with a quantity of water (20 °C) with mass M_w (kg). The specific densities ρ_s (kg m^{-3}) of the samples were determined using the relation:

$$\frac{M_w}{\rho_w} + \frac{M_s}{\rho_s} = V_f \tag{4.1}$$

where ρ_w is the density of water at 20 °C and V_f is the volume (m^3) of the flask. This measurement was repeated several times, obtaining average specific densities of 2850 ± 20 kg m^{-3}, 2734 ± 25 kg m^{-3}, 2249 ± 10 kg m^{-3} and 787 ± 15 kg m^{-3} for volcanic sand, volcanic rock, marble sand and clay respectively. Specific density measurements of sieved samples of volcanic sand with a grain-size range of 28-125, 125-250, 250-500 and 500-710 μm indicate that smaller grains have a slightly higher density [Meschendorp, 1994]. The difference with unsieved sample (< 0.4%) is virtually negligible. As the bulk density ρ_b is related to the specific density ρ_s according to $\rho_b = (1-\varepsilon)\,\rho_s$, values of 2565 ± 45 kg m^{-3}, 2242 ± 40 kg m^{-3}, 2002 ± 40 kg m^{-3} and 519 ± 42 kg m^{-3} are found for volcanic sand, volcanic rock, marble sand and clay respectively (table 4.3).

Table 4.3 - Specific and bulk densities for material samples

Sample	*Specific density [kg m^{-3}]*	*Bulk density [kg m^{-3}]*
Volcanic sand	*2850 ± 20*	*2565 ± 45*
Volcanic rock	*2736 ± 25*	*2242 ± 40*
Marble sand	*2249 ± 10*	*2002 ± 40*
Clay	*787 ± 15*	*519 ± 42*

4.4.2 Radium content

For the determination of the radium content, powdered samples of about one liter were placed in Marinelli beakers and positioned over the hyper-pure germanium detector described in section 4.2 inside the lead shielding, and analyzed for gamma-activities of several lines of radon daughters ^{214}Pb and ^{214}Bi. The ^{226}Ra contents were estimated, even in this case, assuming secular equilibrium in the radioactive series and resulted in 19.5 ± 2.1 Bq kg^{-1} for volcanic sand (and volcanic rock), 3.9 ± 0.4 Bq kg^{-1} for marble sand and 29.4 ± 3.3 Bq kg^{-1} for clay. Since emanated radon could escape the samples during these measurements the actual radium content may be significantly higher

It must be emphasized that, however, knowing the exact value of the radium content could be not so relevant for this study on radon transport, since we used an external radioactive source of which we know the radon production rate and which contributes to our deep-soil radon concentration, i.e. the radon activity concentration at the bottom of the sample column.

4.4.3 Radon emanation coefficient

The radon emanation coefficient *f*, i.e. the total fraction of radon atoms that escape from a mineral grain, can be defined as the ratio between the radon activity outside the material A_{Rn} and the radium activity inside the material A_{Ra} [Kovler, 2006]:

$$f = \frac{A_{Rn}}{A_{Ra}} \tag{3.2}$$

and, in the case of powders, it can be express in terms of exhalation rate *E*:

$$f = \frac{E}{C_{Ra}\,\lambda_{Rn}} \tag{3.3}$$

where C_{Ra} is the ^{226}Ra activity concentration and λ_{Rn} is the decay constant for ^{222}Rn. Known the radium activity concentration from γ-ray spectroscopy measurements, the exhalation rate E per mass M of material (Bq kg^{-1} s^{-1}) was determined by means of the closed-can techinque [Abu-Jarad, 1998] through the following equation [Singh et al., 2004]:

$$E = \frac{C_{Rn} V \lambda_{Rn} t}{M\left[t + 1/\lambda_{Rn}\left(e^{-\lambda_{Rn} t} - 1\right)\right]} \tag{3.4}$$

where C_{Rn} is the radon concentration measured inside the can [Bq/m^3], V is the free volume of the can and t the exposure time.

The determination of radon specific exhalation rate was performed by passive detection technique with solid state nuclear track detectors (SSNTD), CR-39 type. The samples, having a mass of about 300 g, were dried at 80 °C, then placed in sealed cylindrical cans (8.6 cm diameter, 10.5 cm height). Each CR-39 detector (active area of 25x25 mm^2) is fixed, inside its diffusion chamber, on top inside of each can and exposed, for three months, for detecting alpha particles from the decay of the exhalated radon from the sample in the remaining volume of the can.

Table 4.4 presents the results for radon emanation coefficient obtained by using the closed-can method. The effect of grain size on emanation fraction was investigated by sieving the volcanic sand samples to form 4 set according to grain size. The emanation coefficient was then determined for each set at < 2% water content. Emanation was found to be a decreasing function of grain size. Although temperature may influence the magnitude of the radon emanation coefficient, it has been demonstrated that within the normal range of temperature variability of surface soils, this effect is of minor importance [Nazaroff et al., 1988].

Table 4.4 - Radon emanation coefficients for volcanic materials, marble sand and clay.

Sample	*Radon emanation coefficient*
Volcanic sand (φ < 500 μm)	*0.012 ± 0.003*
Volcanic sand (0.5 < φ < 1 mm)	*0.010 ± 0.003*
Volcanic sand (1 < φ < 1.4 mm)	*0.007 ± 0.002*
Volcanic sand (1.4 < φ < 2 mm)	*0.006 ± 0.002*
Volcanic rock (18 < φ < 25 mm)	*0.003 ± 0.001*
Marble sand	*0.075 ± 0.012*
Clay	*0.180 ± 0.027*

4.5 Computer code

In order to carry out calculations with *RnMod3d*, to compare the experimental data with those expected by the radon-transport model, it was necessary to compile a suitable calculation program. This *job file*, written in Pascal, contains a link to the RnMod3d code, with all information on the computational grid, which define the geometry of the problem, the boundary and initial conditions, the soil parameters, what output to calculate, etc. The code lines of the job file are reported in Appendix A. In view of near future developments involving more complicated laboratory measurements, we considered a material column which may take into account up to three layers of different sample materials, with an inhomogeneous moisture vertical profile. As example, it is reported the case of a profile in which the moisture saturation is set at 10% at z = 0, i.e. in correspondence of the material-atmosphere interface, and then increases regularly until reaching a constant value of 100% from a depth of 1 meter.

Chapter 5

Laboratory measurements and results

In this chapter, the results of measurements with steady-state combined diffusive and advective transport in low-moisture samples are discussed and compared with analytical solutions of the governing differential equations given by the simulations. Advective transport was induced by supplying an upward air-flow through the two inlets in the lower part of the laboratory facility. All the experiments were performed without the lid on the vessel in order to reproduce as possible the case of radon transport and exhalation from soil into the atmosphere.

The experiments may be subdivided into two parts. The first, discussed in section 5.3, covers steady-state upward advective transport for increasing flux rates and includes a description of the analytical model. Secondly, the experiments with a well defined upward advective transport, at differrent temperatures in a range of about 70 degrees, are reported in section 5.4. A comparison of the results, in the light also of the different grain size and porosity of the samples, is given in section 5.5. Preliminarily, some considerations about the samples conditions during the experiments and the experimental techniques, procedures and analyzing methods to extract radon concentration profile at different temperatures are described in sections 5.1 and 5.2 respectively.

5.1 Samples characteristics

As outlined in the previous chapter, most material properties such as density, porosity, radium content and radon emanation coefficient could be determined with fair

precision. A main difficulty in the experiments deals with the uncertainty in pore-water content. As the vessel had been completely filled, each sample was dried by inducing an air flow of 3 liter/min (about 5% rel. humidity) through the column for two days. Afterwards, the samples were left undisturbed for more than a week before starting the experiments. Gravitational downward transport and evaporation of remaining pore water during this period further dried the samples.

This process, however, may not have lowered the water content to such an extent that only hygroscopic water remained in the pores. In addition, since all our measurements were performed without the cover, the air in the laboratory might have moisturized the samples again. Therefore, the exact pore-water content was not precisely *a priori* known and might even vary with height and time. This complicates considerably the situation for radon transport, but by measuring the variation of moisture content with height in the vessel, it is feasible, in principle, to model a position-dependant moisture saturation value.

Due to this variations in pore-water content, some significant changes also occurred in partition-corrected porosity β, according to eq. (2.19). Except in cases where the relative humidity approaches zero, the partition-corrected porosity does not equal the value of porosity (ε) and increases with increasing moisture and decreasing temperature (in relation to the Ostwald partitioning coefficient L), reaching values up to 2.7% higher than ε for dry materials. Fortunately, it is not of crucial importance to know with precision the radon adsorption coefficient, which also appears in eq. (2.19), since the influence of adsorption on partition-corrected porosity is small (it is typically of the order of 10^{-6}-10^{-7} m^3 kg^{-1}). For this reason, it appears justified to neglect the effect of adsorption on the value of partition-corrected porosity, unlike what observed about the effect of pore water (0-15%).

An overview of the parameters to be used in the model for radon transport study through porous media are given in table 5.1 (with statistical uncertainties). Although also the emanation coefficient depends on the pore-water content of the sample in the vessel, no variations with height and time, with respect to the dry-material values, are taken into account.

Table 4.1 - Parameters of laboratory samples in the vessel as used in model calculations.

Sample	*Bulk density [kg m^{-3}]*	*Radium content [Bq kg^{-1}]*	*Air-filled porosity*	*Partition-corrected porosity*	*Radon emanation*
Volcanic sand	*2565 ± 45*	*19.5 ± 2.1*	*0.10 ± 0.01*	*0.100 ± 0.010*	*0.012 ± 0.003*
Volcanic rock	*2242 ± 40*	*19.5 ± 2.1*	*0.21 ± 0.01*	*0.211 ± 0.020*	*0.003 ± 0.001*
Marble sand	*2002 ± 40*	*3.9 ± 0.4*	*0.11 ± 0.01*	*(0.111-0.113) ± 0.010*	*0.075 ± 0.012*
Clay	*519 ± 42*	*29.4 ± 3.3*	*0.34 ± 0.02*	*(0.341-0.344) ± 0.030*	*0.180 ± 0.027*

5.2 Experimental procedures and analysis methods

Unfortunately, since we had only three available radon detectors (Alpha-GUARDs) with respect to the five sampling points inside the vessel, we could not perform all the measurements at the same time but we were forced to split each series of measurements into two sets. As already mentioned in section 4.1.1, sampling was started at positions 1,3 and 5 (at bottom, in the middle and at the top of the vessel respectively) and subsequently at positions 2, 3 and 4. Due to the variability of our under-ground radon source, whose concentration value inevitably affects the radon activity concentration measured at any given point and time inside the vessel, some differences were found between the two sets of each measurement series, under the same conditions of flow-rate, temperature or porosity. In order to take into account these variations and bring the raw data into activity concentration values each other consistent, a normalization procedure was carried out over the results from AGREF detector, kept at the same position (sampling point '3') in the two measurement sets. The reliability of this procedure was verified by comparison with data from the RAD7, respect to which a further normalization was also performed in order to compensate for any variations of radon activity concentration in the under-ground source.

The value of radon concentration at each sampling point inside the vessel was determined after a cross-correlation analysis of the time series. In particular, since variations of radon concentration in the ground were 'seen' with a growing delay from the lower sampling point to the upper one, we estimated the delay between each time series in order to align the measurements and, at the same time, cut off those parts of time sequences which, for any reason, did not reproduce the general trend. By way of example, figures 5.1 shows the results of such analysis in a specific case. Note, in particular, how the anomalous behavior of radon detector after a certain point in correspondence of the third sampling points has led us to assess some values as not representative of time series and were neglected.

In order to minimize the effects due to the variability of the under-ground radon source, we performed the two sets of measurement, within each series, always at the

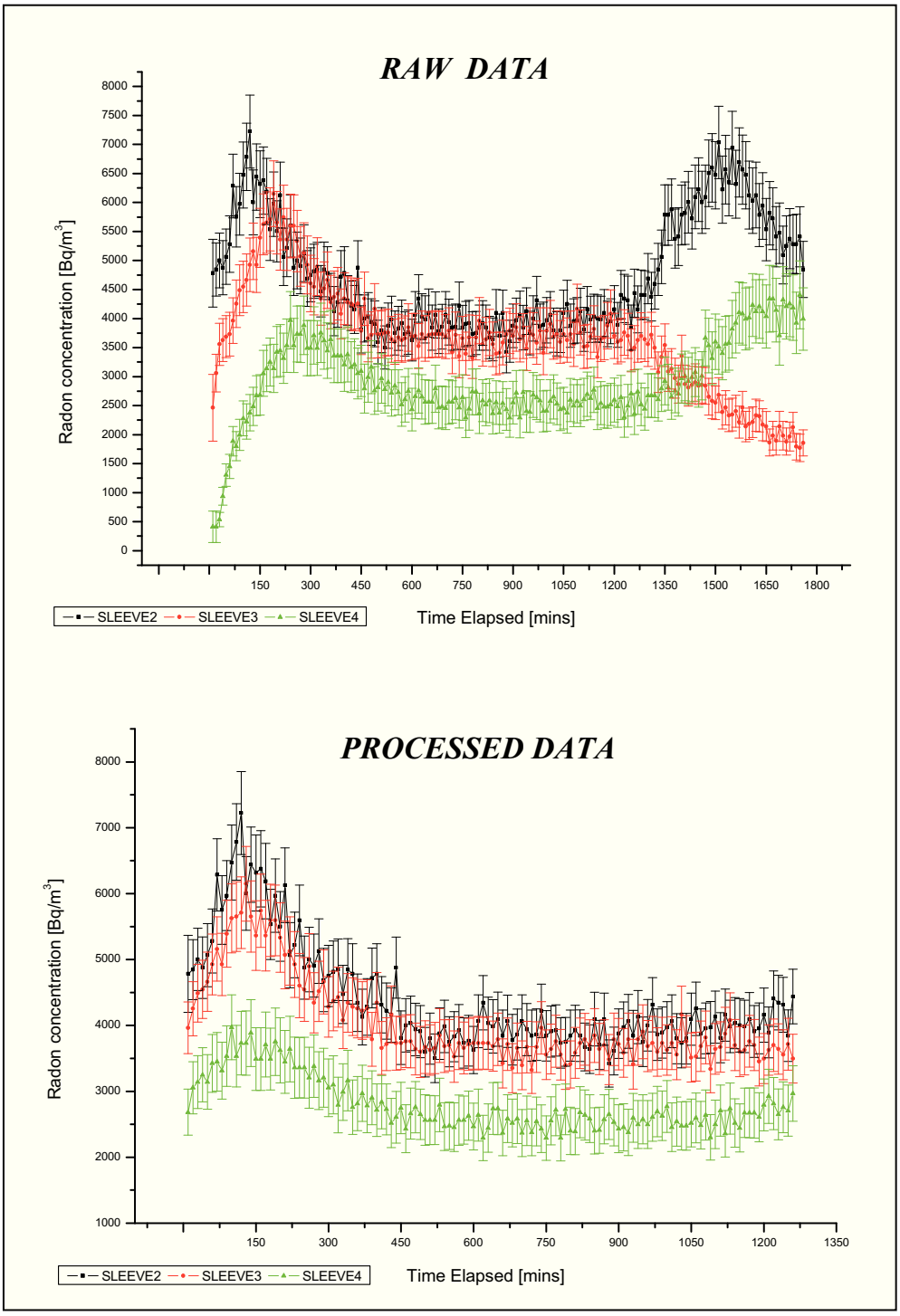

Figure 5.1 - Example of time series before and after cross-correlation analysis. It refers to measurements at sampling points 2, 3 and 4 for volcanic sand at a temperature of 29 °C and an air-flow rate of 0.4 l min^{-1}.

same hours of the day and, as far as possible, under the same meteorological conditions, particularly of temperature and humidity. In any case, we considered two different approaches to trait the processed data, based on different interpretations of the time series.

The first one considers the whole time series. We observed, when analyzing data sets, that the distributions of radon concentrations inside the vessel show right-skewed tails, extending at high magnitudes, typical of log normal distribution (see an example in figure 5.2) The hypothesis for log-normality of measured data was tested and proved using Kolmogorov-Smirnov test with error probability $p \geq 0.05$.

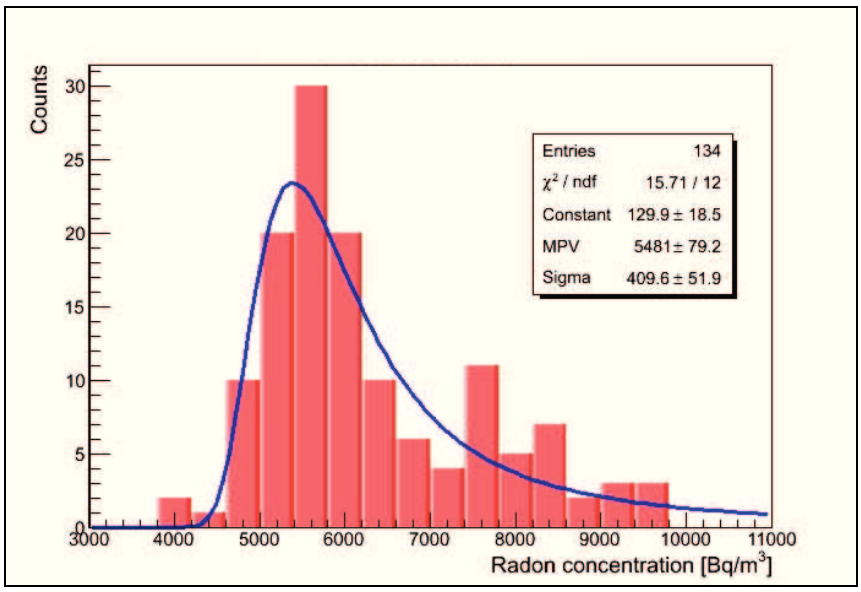

Figure 5.2 - Example of frequency distribution of the radon concentration inside the vessel. It refers to a measurement at the third sampling point with a sample column of volcanic sand and a flow-rate of 0.8 liter/min (see section 5.3). On y-axis the counts for each concentration range are reported.

In the light of these considerations, the best way to determine the radon concentration at each sampling point was based on the determination of the geometric mean (i.e. the 50^{th} percentile, the population center of the distribution) resulting from each sample of data after cross-correlation analysis and normalization procedures. In this context, the dimensionless geometric standard deviations from the log-normally distributed popu-

lation were used to find the bounds of confidence intervals, i.e. the experimental errors to be associated with each measurement. The second approach to determine the radon concentration inside the vessel was based, more precisely, on the selection of an interval in which the values of activity concentration remain constant within the time series. For different series of measurements, in spite of the short duration (in some cases) of such intervals, we verified that the two methods were consistent with each other, returning concentration values that, even if not in absolute value, reproduced with good approximation the same profile trends. Supported by the results of this comparison, we opted, for simplicity, for the first approach

5.3 Experiments with upward advective transport

In this experiment steady-state radon concentrations were measured as function of height in the vessel without a crawl space, i.e. without the upper cover, and an upward air-flow induced by withdrawing radon-rich air from the ground, according to the procedures described in section 4.2. Radon concentration profiles were measured at flow rates J of 0.2, 0.4 and 0.8 liter/min, regulated by a gas-flow controller.
Advective transport of radon in the vessel can be described by a one-dimensional model. Some aspects deteriorate the condition of full one-dimensionality, such as the lateral flange to remove samples, the down perforated plate (not covering the full cross-sectional area), the metal ring surrounding the plate as well as the glass-wool slab placed on the perforated plate, but these are considered to have a minor influence. Moreover, the glass-wool filter may be ignored due to its small volume (about 4%) with respect to the total volume of the stainless steel cylinder. As a consequence, analytical one dimensional modelling may be applied for comparison with the experimental results.

5.3.1 Model description

The one-dimensional steady-state problem, counterpart of eq. (2.25), concerns a column of homogeneous material of height L and cross-sectional area 0.196 m^2. Both steady Darcy flow of soil gas and combined diffusion and advection of radon are considered. The problem is sketched in figure 5.3.

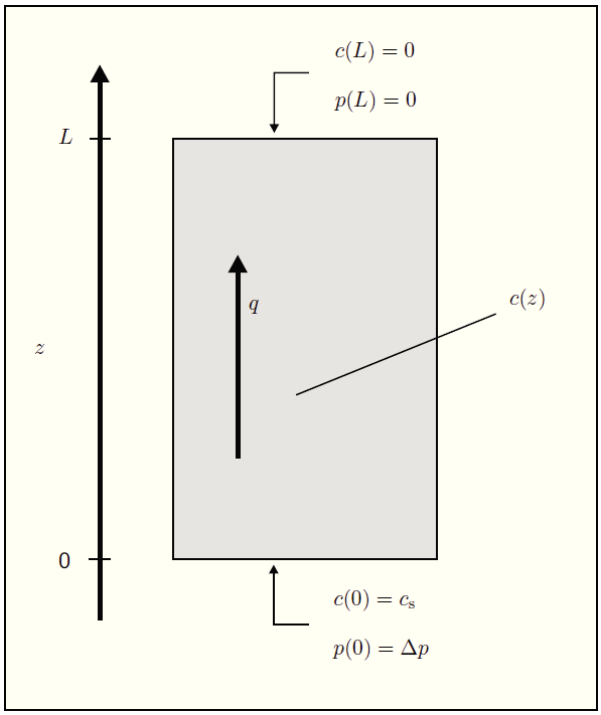

Figure 5.3 - One-dimensional representation of the vessel with boundary conditions for a situation in which air is supplied from below and without the lid installed. Note that an upward air-flow is associated with a positive bulk air (Darcy's velocity) *v*.

The following boundary conditions apply for the flow of soil gas:

1) At $z = L$ the disturbance pressure is 0 Pa.
2) At $(z = 0)$ the disturbance pressure is ΔP ($\Delta P > 0$ means upward air-flow; $\Delta P = 0$ means pure diffusive radon transport, according to eq. (2.38).

Other boundaries are closed for transport. The following boundary conditions apply for the transport of radon:

3) At $z = L$ the concentration is set to 0. This value rounds down, for simplicity, the measured radon concentration value in the (well-ventilated) laboratory (tipically ~ 15 Bq m^{-3}).
4) At $(z = 0)$ the radon concentration is c_s. This value arises from the average concentration of radon-rich air pumped from the ground into the vessel.

Other boundaries are closed for transport. The radon decay constant (λ) is set to $2.09838 \cdot 10^{-6}$ s^{-1} and the dynamic viscosity (μ) is set to $17.5 \cdot 10^{-6}$ Pa s. Air which is supplied to the box will leave the vessel through the surface of the sample column at $z = L$.

The analytical solution to the above problem can be found in [Collé et al., 1981]. The radon concentration in the column $(0 \le z \le L)$ is:

$$c(z) = \frac{G}{\lambda}\left(1 - \frac{\exp\left(\frac{qz}{2D}\right)\sinh\frac{L-z}{\Lambda}\exp\frac{-q\,(L-z)}{2D}\sinh\frac{z}{\Lambda}}{\sinh\frac{L}{\Lambda}}\right) + c_s\exp\left(\frac{qz}{2D}\right)\frac{\sinh\frac{L-z}{\Lambda}}{\sinh\frac{L}{\Lambda}} \qquad (5.1)$$

where G is the radon generation rate per pore volume, q the soil-gas flow rate in the direction of the z-axis:

$$q = \frac{k}{\mu}\frac{\Delta P}{L} \qquad (5.2)$$

L_d is the diffusion length:

$$L_d = \sqrt{\frac{D}{\varepsilon\lambda}} \qquad (5.3)$$

and where Λ is the diffusion length modified by the superimposed flow velocity:

$$\Lambda = \left(\frac{q^2}{4D^2} + L_d^{-2} \right)^{-0.5} \tag{5.4}$$

The flux at $z = L$ is:

$$j = \left(-D \frac{dc}{dz} + qc \right) \Bigg|_{z=L} \tag{5.5}$$

$$= \frac{G}{\lambda} \left(\frac{q}{2} + \frac{D}{\lambda} \frac{\cosh \frac{L}{\Lambda} - \exp \frac{qL}{2D}}{\sinh \frac{L}{\Lambda}} \right) + c_s \frac{D}{\Lambda} \frac{\exp \frac{qL}{2D}}{\sinh \frac{\mathrm{L}}{\Lambda}}$$

Section 4.5 showed how the problem has been implemented in RnMod3d. The job file also contains the exact solution.

It should be remarked that the permeability *k* is a very relevant parameter since, according to eq. (2.28), it determines the air flow rate through the sample at a given pressure difference over the column. However, since the air-flow was set using a mass-flow controller in our experiments with advective transport and since only the bulk air velocity *v* should be needed to model advective transport of radon[1], the permeability of the samples may not be, in principle, relevant for this study (assuming a homogeneous column). Nevertheless, in order to evaluate how this parameter affects the radon transport, its estimate, for each sample, was made by means of pressure field measurements in the column according to eq. (5.2). Absolute pressure differences between the surface and different positions in the samples were measured by vertically entering 30 mm diameter probes (model TP704-20BAI) by Delta Ohm s.r.l., Italy. The tip of the probe has a small perforation while the other end is connected to a manometer (model HD2304.0) by means of a PP471 SICRAM module. These probes were placed, during the filling of the vessel, in correspondence to the top

[1] Air velocities are obtained by dividing the measured flow rate *J* by the surface area of the sample (0.196 m^2).

(sleeve 5), the middle (sleeve 3) and the bottom (sleeve 1) of the sample column. In order to avoid that the perforated tip of the probes could become obstructed by sample grains while it was being covered, it has been protected with a layer of cotton wool. The extracted permeability values, together with the measured pressure differences between the top and the bottom of the vessel for each sample, were included as input parameters in the model calculations.

5.3.2 Results and discussion

Four measurements series were carried out, all of them without cover on the vessel, each one for the four different material samples chosen to perform our study on radon transport mechanisms in porous media. As already mentioned in section 5.1, a nearly zero moisture content in the pore spaces of the samples was established by increasing the temperature inside the vessel up to about 100 °C and continuously flushing the material column with an air-flow of 3 liter/min (through the two inlets in the bottom) during at least two days. Thereafter, the samples were left undisturbed for more than a week before starting the experiments, in order to further dry the column material. Up to 15 liters of water (in the case of marble sand, material characterized by high hygroscopicity) were removed from the vessel just after completing this operation.

Radon concentration profiles were extracted at the five sampling points according to the procedures described in section 5.2, by withdrawing radon-rich air from the under-ground source at flow rates of 0.2, 0.4 and 0.8 liter/min. The measured concentration as function of height, together with results of the analytical one-dimensional model, are shown in figures 5.4. - 5.7. The solid lines represent calculations based on eq. (5.1) using the parameters listed in tables 5.2 - 5.5. Applying fit procedure to the experimental data, we can extract for each material samples the bulk diffusivities.
Note that the radon production rate per pore volume was set by introducing the samples properties according to eq. (2.20), even if, on our time scale, it should be negligible compared to the radon pumped from the ground. The pressure field was

calculated with boundary conditions implying zero pressure at the top and a positive pressure at the bottom of the sample column. The induced flow rate through the samples with these boundary pressures (obtained from the Darcy's law expressed in terms of total discharge rate through a porous media) should reflect with good approximation the true air-flow rate profile inside the vessel.

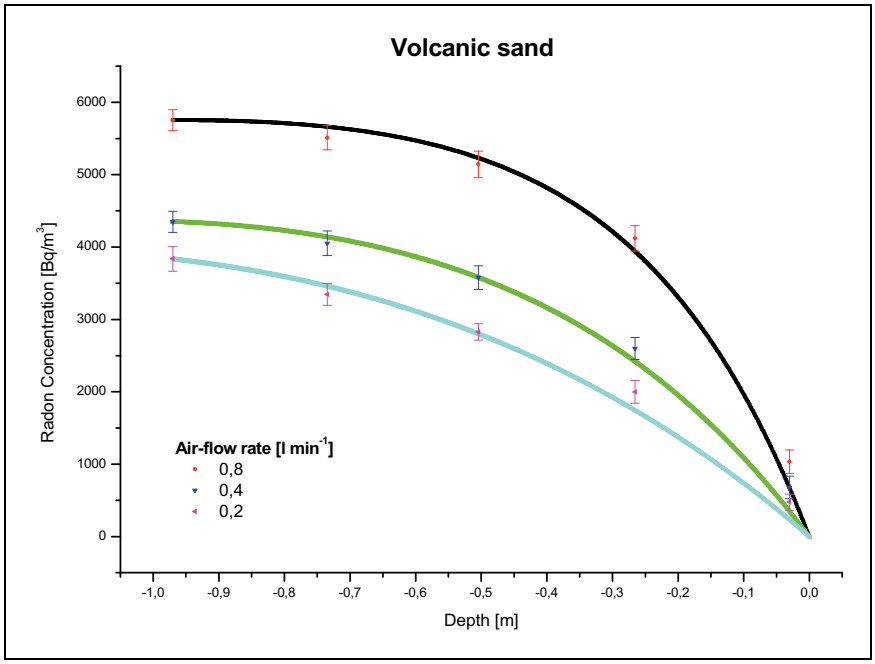

Figure 5.4 - Radon concentration as function of depth for different values of the upward air-flow rate (l min^{-1}) for measurement with combined diffusive and advective transport without a crawl space for volcanic sand. Solid lines represent results from the fit with the analytical 1D model utilizing parameters of the sample as given in table 5.2.

Table 5.2 - Parameters of material sample and radon concentration as used in model calculations.

Air-flow rate [l min^{-1}]	*0.2*	*0.4*	*0.8*
Pressure difference [Pa]	*3.1*	*7.4*	*12.8*
Deep-soil radon concentration [Bq m^{-3}]	*5753*	*4348*	*3836*
Soil permeability [m^2]	*8.63 · 10^{-11}*		
Density of the grain material [kg m^{-3}]	*2565*		
Dynamic viscosity [Pa s]	*17.5 · 10^{-6}*		
Partition-corrected porosity	*10 %*		
Volumetric water content	*0.33 %*		
Ostwald partitioning coefficient	*0.2047*		
Bulk diffusivity [10^{-6} m^2 s^{-1}]	*1.09*		
X^2	*0.52*	*0.40*	*0.83*

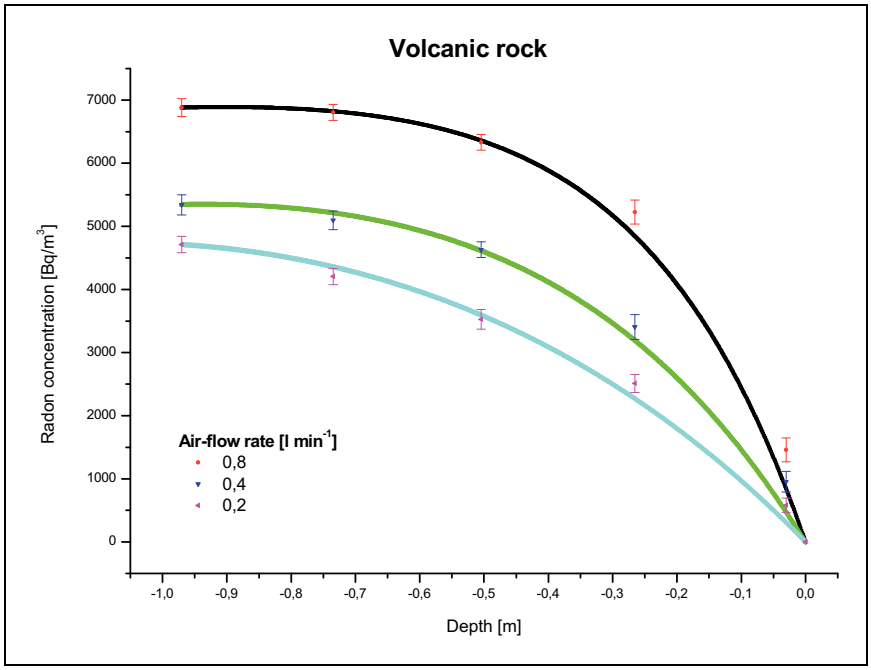

Figure 5.5 - Radon concentration as function of depth for different values of the upward air-flow rate (l min^{-1}) for measurements with combined diffusive and advective transport without a crawl space for volcanic rock. Solid lines represent results from the fit with the analytical 1D model utilizing parameters of the sample as given in table 5.3.

Table 5.3 - Parameters of material sample and radon concentration as used in model calculations.

Air-flow rate [l min^{-1}]	*0.2*	*0.4*	*0.8*
Pressure difference [Pa]	*2.7*	*5.4*	*11.3*
Deep-soil radon concentration [Bq m^{-3}]	*6880*	*5341*	*4712*
Soil permeability [m^2]	*$1.05 \cdot 10^{-10}$*		
Density of the grain material [kg m^{-3}]	*2242*		
Dynamic viscosity [Pa s]	*$17.5 \cdot 10^{-6}$*		
Partition-corrected porosity	*21.1 %*		
Volumetric water content	*1.57 %*		
Ostwald partitioning coefficient	*0.2047*		
Bulk diffusivity [10^{-6} m^2 s^{-1}]	*1.03*		
X^2	*1.03*	*0.46*	*1.11*

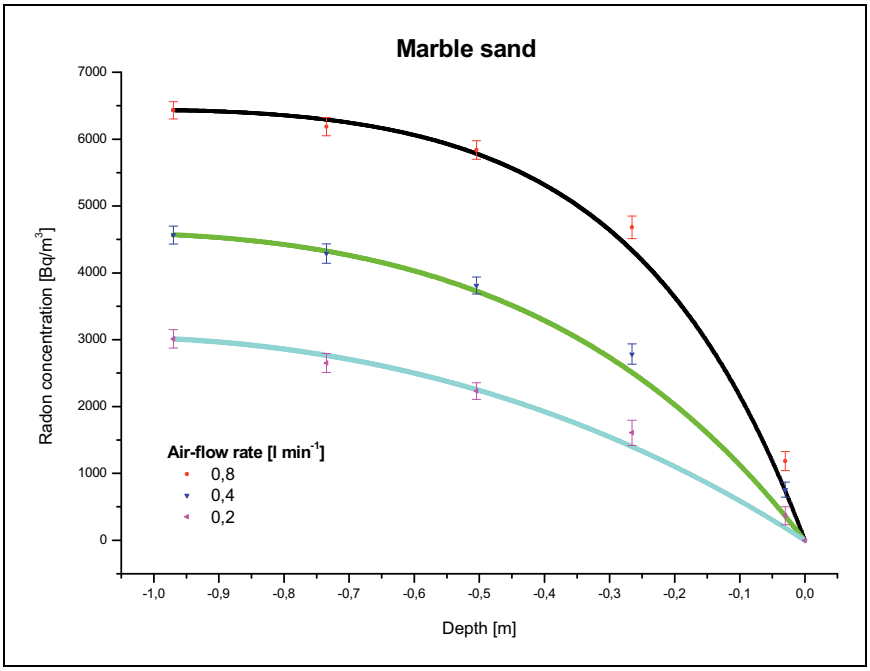

Figure 5.6 - Radon concentration as function of depth for different values of the upward air-flow rate (l min^{-1}) for measurements with combined diffusive and advective transport without a crawl space for marble sand. Solid lines represent results from the fit with the analytical 1D model utilizing parameters of the sample as given in table 5.4.

Table 5.4 - Parameters of material sample and radon concentration as used in model calculations.

Air-flow rate [l min^{-1}]	*0.2*	*0.4*	*0.8*
Pressure difference [Pa]	*3.5*	*7.7*	*15.2*
Deep-soil radon concentration [Bq m^{-3}]	*6432*	*4564*	*3012*
Soil permeability [m^2]	*7.50 · 10^{-11}*		
Density of the grain material [kg m^{-3}]	*2002*		
Dynamic viscosity [Pa s]	*17.5 · 10^{-6}*		
Partition-corrected porosity	*11.3 %*		
Volumetric water content	*15 %*		
Ostwald partitioning coefficient	*0.2047*		
Bulk diffusivity [10^{-6} m^2 s^{-1}]	*1.06*		
X^2	*1.25*	*0.93*	*0.46*

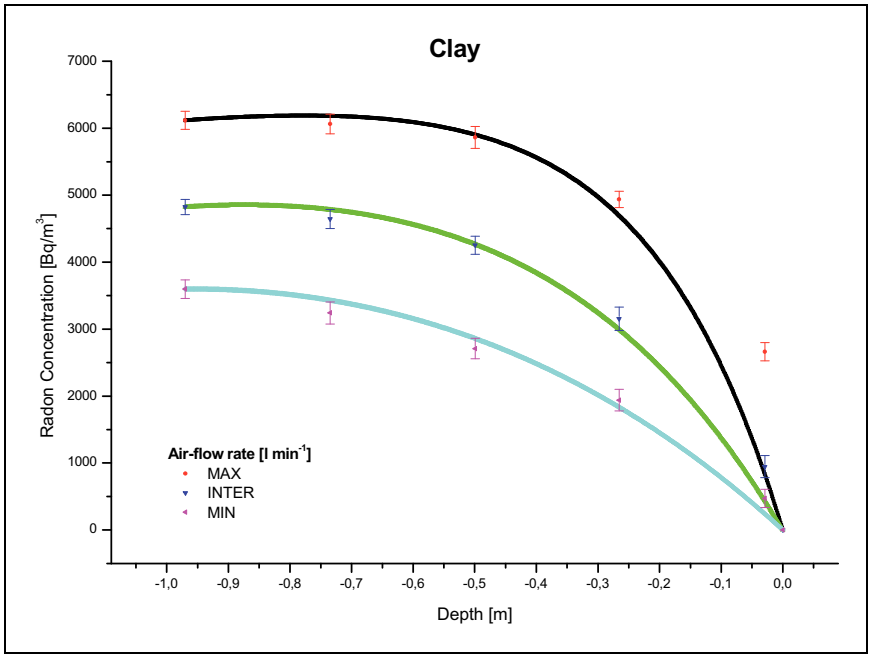

Figure 5.7 - Radon concentration as function of depth for different values of the upward air-flow rate (l min^{-1}) for measurements with combined diffusive and advective transport without a crawl space for clay. Solid lines represent results from the fit with the analytical 1D model utilizing parameters of the sample as given in table 5.5.

Table 5.5 - Parameters of material sample and radon concentration as used in model calculations.

Air-flow rate [l min^{-1}]	*0.2*	*0.4*	*0.8*
Pressure difference [Pa]	*1.5*	*2.7*	*4.3*
Deep-soil radon concentration [Bq m^{-3}]	*6118*	*4822*	*3598*
Soil permeability [m^2]	*2.31 · 10^{-10}*		
Density of the grain material [kg m^{-3}]	*519*		
Dynamic viscosity [Pa s]	*17.5 · 10^{-6}*		
Partition-corrected porosity	*34.4 %*		
Volumetric water content	*5.3 %*		
Ostwald partitioning coefficient	*0.2047*		
Bulk diffusivity [10^{-6} m^2 s^{-1}]	*1.07*		
X^2	*1.21*	*0.44*	*0.68*

It is seen that, in general, agreement with experiments is good, for all the air-flow rates and types of sample. The measured concentration profiles follow a reasonably smooth curve and no notable deviations from the simulations seem to occur, although the model tends to slightly overestimate the radon concentrations in the lower part of the vessel. On the other hand, more remarkable deviations are observed in the last 30 centimeters near the top of the column where the RnMod3d underestimates (exceeding in some cases the experimental errors) the results of our experiments.

The discrepancies at these heights might be explained by the influence of conditions or processes which are not considered in the one-dimensional model. Another cause may be the presence of a greater amount of moisture in the samples close to the top of the vessel than that modeled; in this case the pore-air radon concentration is increased due to a higher emanation coefficient and also by the partitioning of radon between the water and air phases. Moreover, the influence of atmospheric pressure differences should be addressed. During a barometric pressure drop radon-rich air leaves the sample column due to expansion; vice versa, during a barometric pressure rise radon-poor ambient air enters the sample column due to compression. These air displacements, referred to as the barometric pump effect, may have, in some cases, a rather large effect on radon transport processes.

Also, model parameters may be varied such that a better agreement between model and experiments is obtained. This could be realized by using, for example, different values for samples permeability than those estimated by means of pressure differences between the top and the bottom of the material sample, the values being available from the literature. It may be remarked here that increased calculated concentrations at positions close to the top of the vessel, i.e. a better correspondence between model calculation and experimental data, could have been obtained using little higher permeabilities. Nevertheless, because different values for this parameter may result for the same sample, it seems wise to continue using the model parameters as given in tables 5.2-5.5.

It can be concluded that the measurements carried out by withdrawing air from the under-ground at different flow rates are well described by model calculations. The

maximum differences between model and experiment are less than 10% for sleeves 1-4, being (in one case) significantly higher for the sampling point close to the top of the column. These differences may be explained by processes inside the vessel which are hard to control and/or difficult to measure (especially the moisture content and the barometric pressure).

To better define the differences in terms of radon concentration arising from different air-flow rate for any given sample, we expressed each value as a fraction of the corresponding maximum concentration at the deeper sampling point, plotting the results as a function of depth. Figure 5.8 shows the obtained profile for volcanic sand, volcanic rock, marble sand and clay respectively. As expected, the slopes vary significantly as a result of changes of the air-flow rate, maintaining, however, the same general trend independently of the sample. Thus, the percentage of radon that reaches a given point inside the vessel increases with increasing flux, ranging, for example, from 73.7 to 89.4% and from 76 to 53.3% for volcanic sand and volcanic rock at the third and the fourth sampling points respectively.

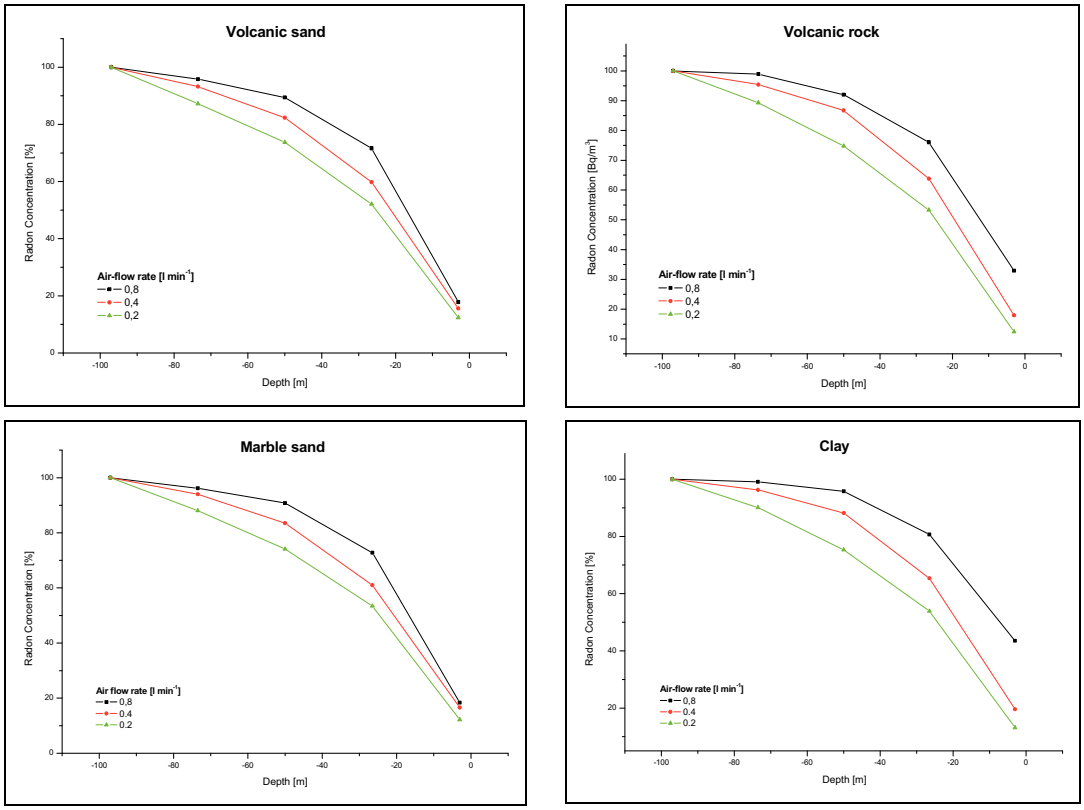

Figure 5.8 - Percentage of radon concentration as function of depth for different values of the upward air-flow rate for volcanic sand (in the upper left), volcanic rock (in the upper right), marble sand and clay (lower pictures).

5.4 Experiments with temperature variations

In order to assess the role of temperature on radon transport mechanisms in porous media, four experiments were performed at a constant air-flow rate of 0.4 liter/min under well-defined and controlled conditions by means of the set-up, described in section 4.1.2, which keeps constant (within an experimental error of ± 1.5 °C) the temperature along both vertical and horizontal dimensions inside the vessel. No thermal gradients were allowed in the sample column since the RnMod3d cannot treat soil-gas flow in non-isothermal soil.

For each sample, four different temperatures (between 29 °C and 96 °C) were considered in order to approach different soil conditions, providing, at the same time, the

basic knowledge to further develop the laboratory facility and carry out, in a near future, measurements at much higher temperatures to simulate, with the best possible approximation, a volcanic environment.

To implicitly account for these variations in temperature in radon transport model, some considerations need to be made, since this parameter (that cannot be introduced as input in our calculations) strongly depends on the solubility of radon in water and on the fraction of water saturation of the pore volume in the samples. In particular, the Ostwald's solubility coefficient L of radon in water, defined as the ratio of water radon concentration to air radon concentration, is confirmed to decrease with increasing temperature by about 3% per °C [Surbeck, 1996] due to a hydrophobic effect [Kolomeiesky et al., 1999], varying in our measurements from 0.2047 at 29 °C to 0.1424 at 52 °C, 0.1259 at 69 °C and 0.1186 at 96 °C.

Something similar happens for volumetric water content, introduced in section 2.1 in terms of the volume of the liquid phase and the volume of the pore spaces, since it depends on sample temperature, decreasing with increasing temperature. Its content can be expressed, more simply, on mass basis, w, as the ratio of the mass of the liquid phase, M_w, in the given sample to the mass of the solid material, M_s, according to the following expression:

$$w = \frac{M_w}{M_s} \tag{5.6}$$

The volumetric water content, θ_V, represents the fraction of the total volume of sample that is occupied by the water. Assuming that V_w is the volume of the liquid phase in the sample and that V_t is the total volume of the sample, the volumetric water content can then be defined as follows:

$$\theta_V = \frac{V_w}{V_t} = \frac{V_w}{V_s + V_p} \tag{5.7}$$

where V_s and V_p represent, respectively, the volumes of the solid phase and the pore space. From the definitions in equations (5.6) and (5.7), the volumetric water content,

θ_V, can be expressed in terms of the mass-basis water content, *w*, according to the following formula:

$$\theta_V = w\left(\frac{\rho_b}{\rho_w}\right) \tag{5.8}$$

where ρ_b is the bulk density of the soil (see table 5.1) and ρ_w is the water density. Experimentally, we found values for volumetric water content in the range between practically 0% at 96 °C and 0.33-15%, depending on the characteristics of the sample, at 29 °C. For simplicity, due to the relatively small dimensions of the vessel, assuming constant the temperature of the sample inside, we can consider an uniform volumetric water content, in a confidence interval of ± 5% with respect to the calculated value, along the height of the vessel for each measurement.

4.4.1 Results and discussion

Figures 5.9 - 5.12 show the trend of measured radon concentrations as function of height, for different temperatures inside the vessel, together with the results of the analytical one-dimensional model. As before, the solid lines represent calculations based on eq. (5.1) using the parameters listed in tables 5.6 - 5.9. Now, the Ostwald's solubility coefficient *L* and the volumetric water content θ_V assume a capital importance, since through changes in these parameters we could take into account the temperature variations in RnMod3d.

The general agreement with experiment is observed also in this case, particularly for the experiments with the highest temperature since very small deviations from calculated data were found even in proximity of the sample surface, where theoretical and experimental results are each other comparable within experimental errors. At lower temperatures, the model calculations continue to approximate very well the concentrations at the deeper sleeves, gradually losing in accuracy approaching the low-concentration area inside the vessel. This behavior confirms that we are dealing with systematic discrepancies due, probably only in part, to the reasons discussed above.

The parameter that most affects the vertical profile of radon concentration, being able to describe the temperature variations inside the vessel, is the bulk diffusivity.

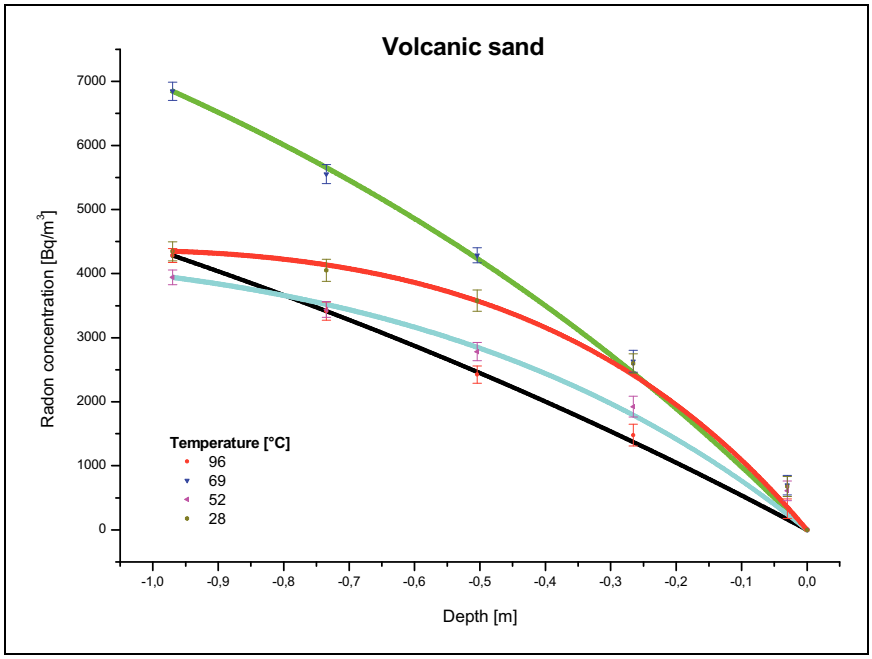

Figure 5.9 - Radon concentration as function of depth for different values of temperature for volcanic sand. Solid lines represent results from the fit with the analytical 1D model utilizing the parameters given in table 5.6.

Table 5.6 - Parameters of material sample and radon concentration as used in model calculations.

Cross-sectional area [m^2]	*0.196*			
Temperature [°C]	*29*	*52*	*69*	*96*
Deep-soil radon concentration [Bq m^{-3}]	*4283*	*6847*	*3941*	*4348*
Soil permeability [m^2]	*$8.63 \cdot 10^{-11}$*			
Density of the grain material [kg m^{-3}]	*2565*			
Partition-corrected porosity	*10 %*			
Ostwald partitioning coefficient	*0.2047 – 0.1186*			
Volumetric water content	*0 – 0.33 %*			
Pressure difference [Pa]	*7.4*			
Bulk diffusivity [10^{-6} m^2 s^{-1}]	*1.09*	*2.30*	*6.98*	*9.97*
X^2	*0.12*	*0.42*	*0.33*	*0.40*

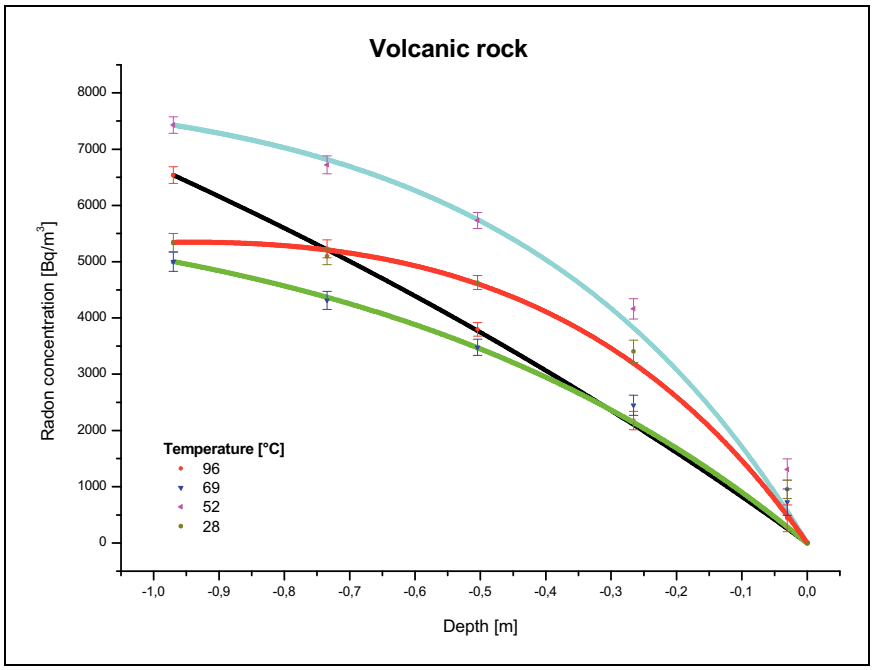

Figure 5.10 - Radon concentration as function of depth for different values of temperature for volcanic rock. Solid lines represent results from the fit with the analytical 1D model utilizing the parameters given in table 5.7.

Table 5.7 - Parameters of material sample and radon concentration as used in model calculations.

Cross-sectional area [m^2]	*0.196*			
Temperature [°C]	*29*	*52*	*69*	*96*
Deep-soil radon concentration [Bq m^{-3}]	*6539*	*4998*	*7428*	*5341*
Soil permeability [m^2]	*$1.25 \cdot 10^{-10}$*			
Density of the grain material [kg m^{-3}]	*22242*			
Partition-corrected porosity	*21.1 %*			
Ostwald partitioning coefficient	*0.2047 – 0.1186*			
Volumetric water content	*0 – 1.57 %*			
Pressure difference [Pa]	*5.4*			
Bulk diffusivity [10^{-6} m^2 s^{-1}]	*1.03*	*2.07*	*7.12*	*9.88*
X^2	*0.07*	*0.77*	*0.98*	*0.44*

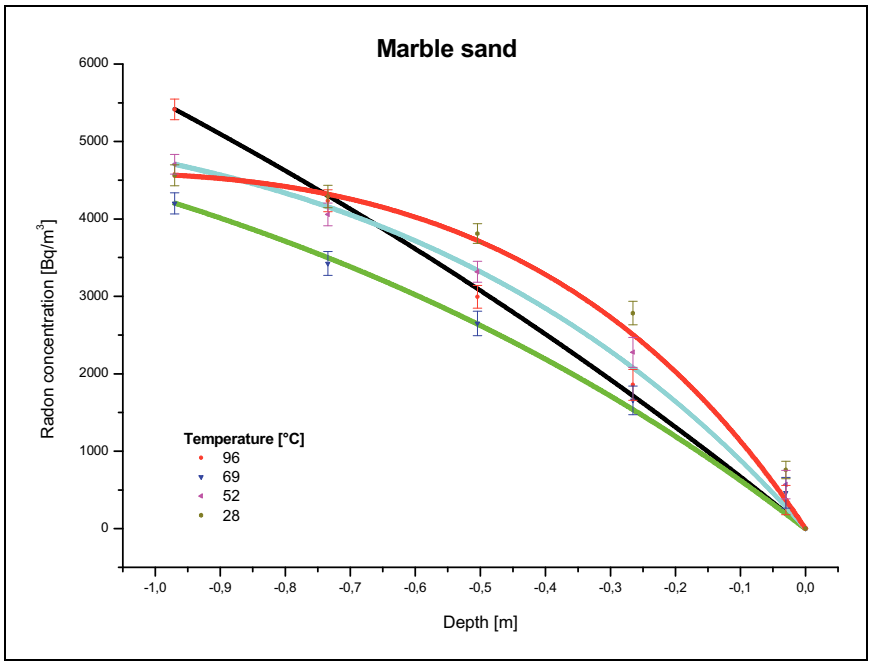

Figure 5.11 - Radon concentration as function of depth for different values of temperature for marble sand. Solid lines represent results from the fit with the analytical 1D model utilizing the parameters given in table 5.8.

Table 5.8 - Parameters of material sample and radon concentration as used in model calculations.

Cross-sectional area [m^2]	*0.196*			
Temperature [°C]	*29*	*52*	*69*	*96*
Deep-soil radon concentration [Bq m^{-3}]	*5415*	*4202*	*4705*	*4564*
Soil permeability [m^2]	*$7.50 \cdot 10^{-11}$*			
Density of the grain material [kg m^{-3}]	*2002*			
Partition-corrected porosity	*11.3 %*			
Ostwald partitioning coefficient	*0.2047 – 0.1186*			
Volumetric water content	*0 – 15 %*			
Pressure difference [Pa]	*7.7*			
Bulk diffusivity [10^{-6} m^2 s^{-1}]	*1.06*	*2.33*	*7.01*	*9.94*
X^2	*0.30*	*0.16*	*0.38*	*0.93*

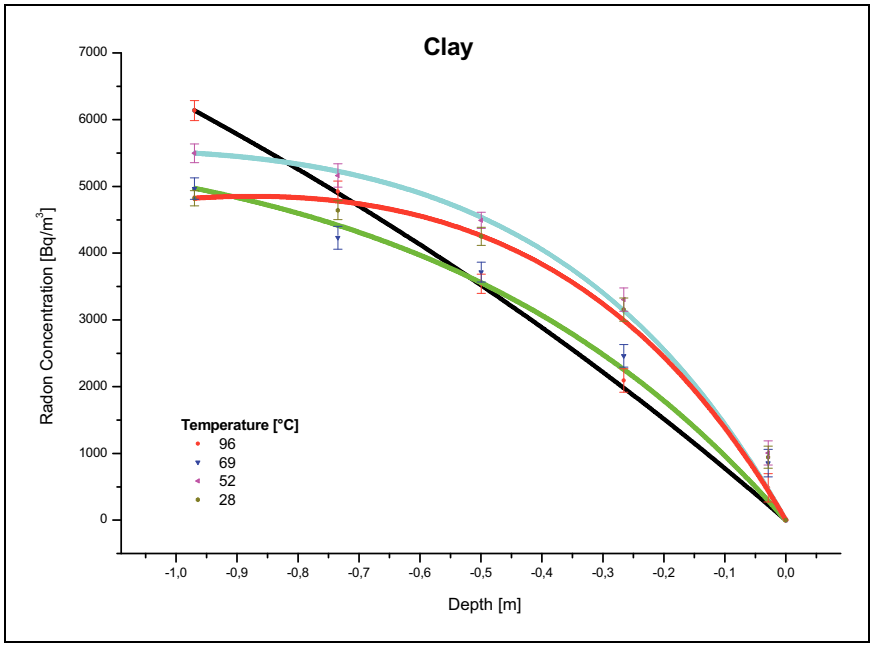

Figure 5.12 - Radon concentration as function of depth for different values of temperature for clay. Solid lines represent results from the fit with the analytical 1D model utilizing the parameters given in table 5.9.

Table 5.9 - Parameters of material sample and radon concentration as used in model calculations.

Cross-sectional area [m^2]	*0.196*			
Temperature [°C]	*29*	*52*	*69*	*96*
Deep-soil radon concentration [Bq m^{-3}]	*6137*	*4968*	*5498*	*4822*
Soil permeability [m^2]	*$2.31 \cdot 10^{-10}$*			
Density of the grain material [kg m^{-3}]	*519*			
Partition-corrected porosity	*34.4 %*			
Ostwald partitioning coefficient	*0.2047 – 0.1186*			
Volumetric water content	*0 – 0.53 %*			
Pressure difference [Pa]	*2.7*			
Bulk diffusivity [10^{-6} m^2 s^{-1}]	*1.07*	*2.03*	*7.02*	*9.98*
X^2	*0.12*	*0.93*	*0.29*	*0.44*

It is seen that diffusion is the most temperature sensitive transport parameter, in comparison to solubility of radon in water and fraction of water saturation. The rate at which gas atoms migrate inside porous media, i.e. the mobility of diffusing radon through sample materials, in fact, strongly depends on the thermal conditions inside the vessel, increasing with increasing temperature. In our measurements, although the range in temperature is rather limited, significant variations of the coefficients D are observed, diffusivities being an order of magnitude higher at 96 °C than at 29 °C (10^{-5} against 10^{-6} m^2 s^{-1}, see tables 5.6-5.9).

Previous studies of noble gases reported Arrhenian behavior (e.g. [Roselieb et al., 1995]) which means that their diffusivity decreases exponentially with reciprocal temperature, following the equation:

$$D = D_0 \times \exp\left(\frac{-E_a}{RT}\right) \tag{5.9}$$

where D_0 is the pre-exponential constant, i.e. the maximum diffusion coefficient (at infinite temperature), R the gas constant, T the absolute temperature in Kelvin and E_a the activation energy of the diffusion process. The dependence of D on reciprocal temperature is shown in figure 5.13 and a least squares fit of the data yields the following expression (for volcanic sand):

$$D = 4.53 \cdot 10^{-1} \, (m^2 \, s^{-1}) \times \exp\left(\frac{-31.3 \left(kJ \, mol^{-1} \right)}{RT}\right) \tag{5.10}$$

where the time-independent pre-exponential was extrapolated by the intercept of $ln\ D_0$ on y-axis (corresponding to infinite temperature, 1/T = 0) and the activation energy for diffusion, which expresses the slope of the curve $-E_a/R$, was calculated by means of the equation:

$$E_a = -R\left[\frac{\log D_1 - \log D_2}{1/T_1 - 1/T_2}\right] \tag{5.11}$$

where T_1, T_2 and D_1, D_2 are, respectively, the temperatures and the corresponding bulk diffusivities of two different points in figure 5.13.

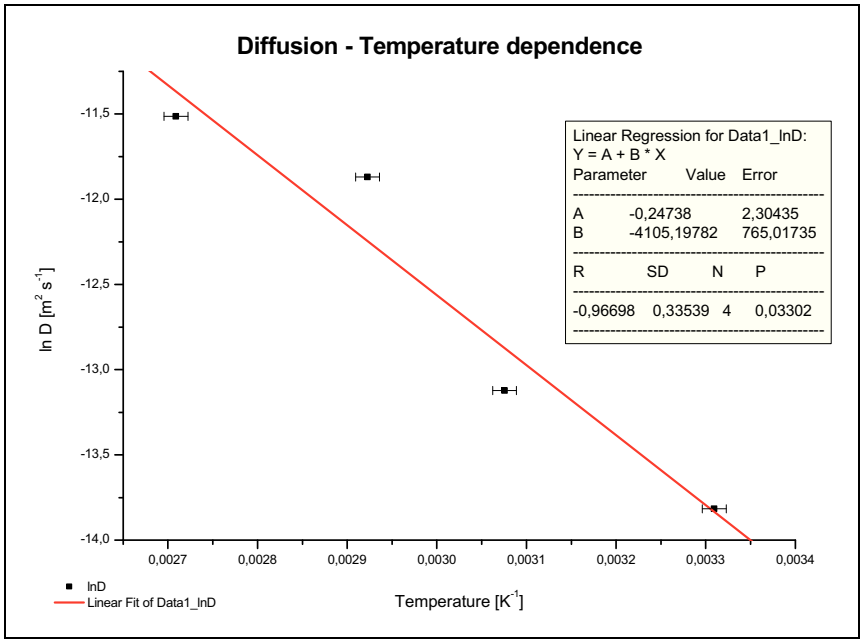

Figure 5.13 - Dependence of *D* on reciprocal temperature. Error bars on the abscissa correspond to uncertainties of about 1.5 °C on temperature determinations. The solid line represents the best fit line.

In any case, the analysis of temperature effects on bulk diffusivity must be further investigated in order to develop a more general equation useful to assess the correlation of diffusion coefficients at higher temperatures, to be applied especially in volcanic environments, and establish, if possible, a technique to study radon anomalies in deep-soil on the basis of time diffusion through the Earth's crust.

To better understand the differences in terms of radon concentration arising from different temperatures inside the vessel, we expressed, as in the previous case of airflow rate variations, each value of radon activity concentration as a fraction of the corresponding maximum value at the deeper sleeve, plotting the results as a function of depth. Figure 5.14 show the obtained profile for volcanic sand, volcanic rock, marble sand and clay respectively.

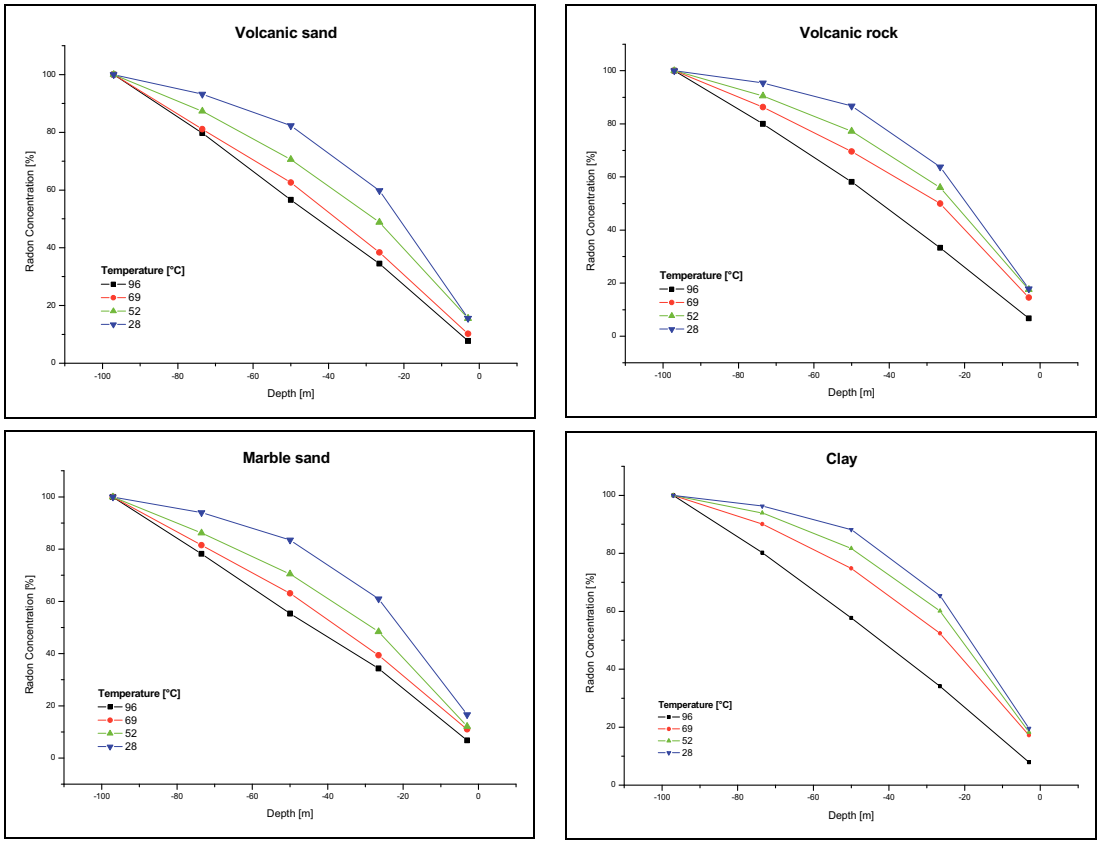

Figure 5.14 - Percentage of radon concentration as function of depth for different values of the temperature for volcanic sand (in the upper left), volcanic rock (in the upper right), marble sand and clay (lower pictures).

The slopes vary significantly as a result of changes of temperature, maintaining, also in this case, the same general trend independently of the sample. Thus, the percentage of radon that reaches a given point inside the vessel increases with decreasing temperature in accordance with the considerations on diffusion coefficient variations, ranging, for example, from 78.2 to 94% and from 57.7 to 88.2% for marble sand and clay at the second and the third sampling points respectively. Note, finally, the practically linear decrease of radon concentration from C_{max} to zero at 96 °C that suggests different scenarios for T > 100 °C.

4.5 Considerations on samples porosity

In order to assess the dependence of radon concentrations on grain size and porosity, we compared the vertical profiles for different materials obtained under the same conditions of air-flow rate and temperature.

Figure 5.15 summarizes the results for the four samples at air-flow rates of 0.2, 0.4 and 0.8 liter/min and temperatures of 29, 52, 69 and 96 °C respectively, in terms of per-cent concentration. Some dependence of concentration from porosity is rather evident both for air-flow and temperature variations. In particular, the vertical profiles are practically overlapped at the lowest flow rate, where any distinction between low-porosity (volcanic sand and marble sand) and medium-porosity (volcanic rock and clay) samples is impossible; the differences grow when the advective transport starts to dominate, becoming highly significant near the sample column surface where the percentage of radon concentration seems to increase almost proportionally to the value of porosity (figure 5.16).

Similar considerations can be made for temperature variations. Here, the differences seem to be related to the porosity in a range of temperatures between 29 and 69 °C, clearly increasing with increasing temperature. Something different happens at 96 °C where the vertical profiles again overlap, indicating some reversal due, probably, to higher thermal convection inside the vessel. In any case, further measurements with different air-flow rates in a more extensive range of temperatures and porosities, could represent a very useful, and necessary, tool to better understand the relationships between porosity, temperature and radon concentrations.

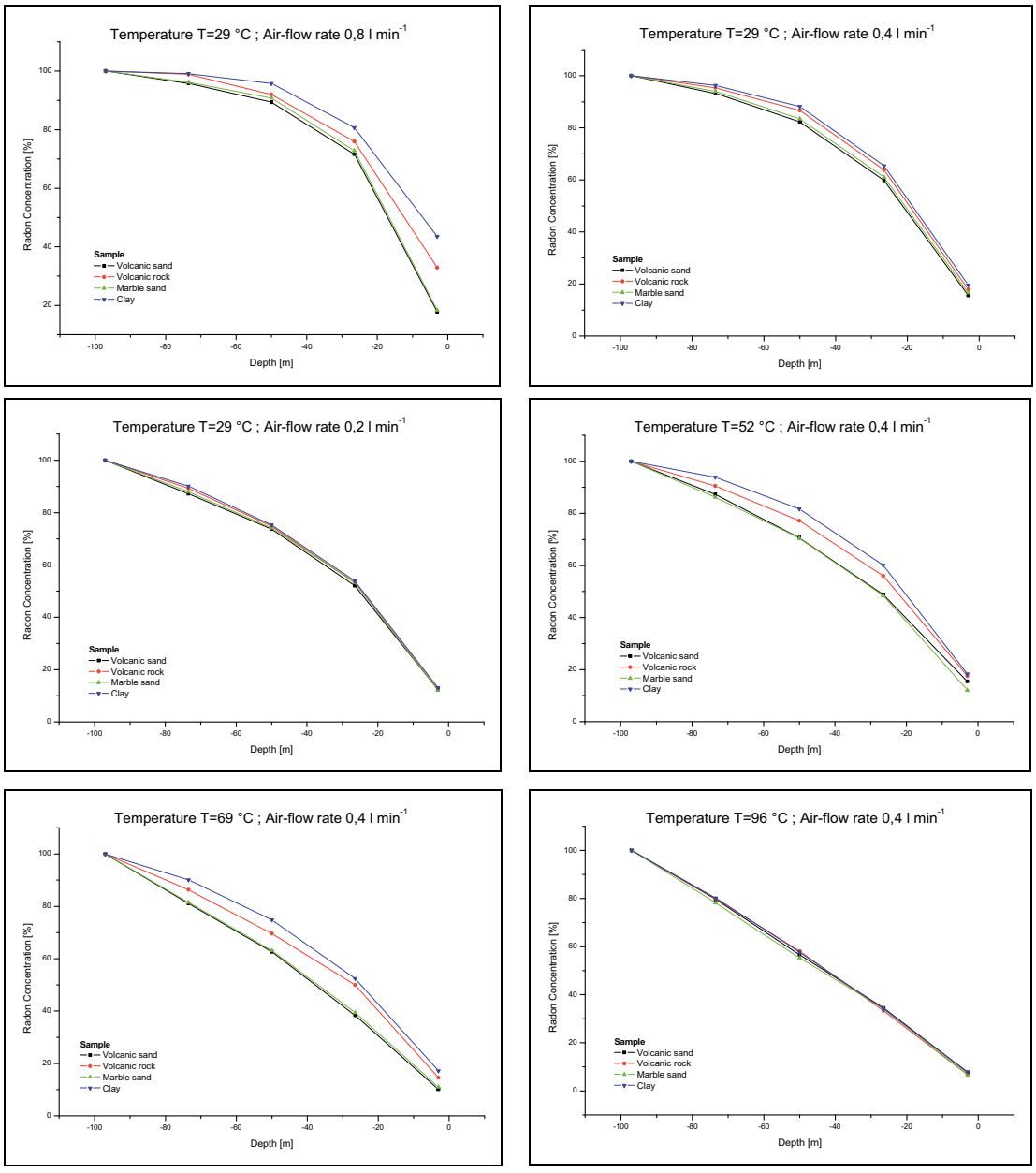

Figure 5.15 - Comparison of the vertical profiles for different materials obtained under the same conditions of air-flow rate and temperature.

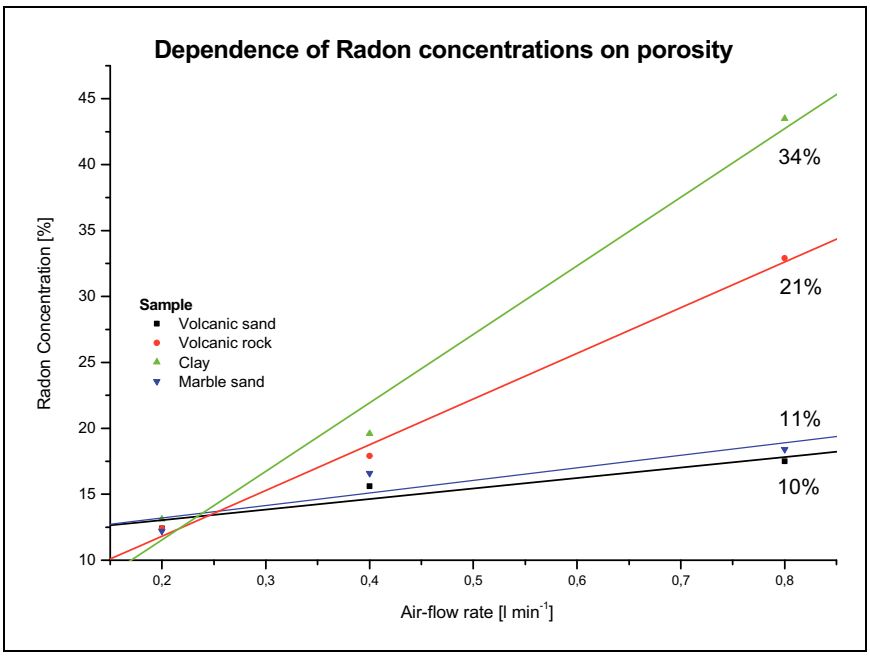

Figure 5.16 - Percentage of radon concentration versus air-flow rate for different porosities.

Concluding remarks and future perspectives

The present work deals with the influence that some physical processes and parameters (advection, temperature, porosity) have on radon transport in porous media from its generation in the soil grains till its exhalation into the atmosphere. The approach chosen in this study focuses on three different aspects of the problem, concerning *in situ* measurements, laboratory experiments and comparisons o data with theoretical models.

The first part of this thesis has been devoted to the study of radon transport in fracturated porous media on the east flank of Mt. Etna volcano, by means of soil-gas radon measurements along a horizontal transect across an active fault in Santa Venerina. More than five times higher values were detected on the upthrown side of the fault than on its downthrown side, indicating a greater structural instability of the downthrown side and hence a greater fracturing which would result in a higher degree of radon dispersion. Moreover, along the main fault plane, advective transport of deep carbon dioxide occurs due to the high ground fracturing and permeability; thus, near the surface, dilution of radon by CO_2 prevails, producing very low radon values. The study of diffusion processes in different geological environments through measurements of vertical profiles of radon concentration was also performed, giving us more detailed information on the radon diffusion parameter which is strongly related with the permeability of rock and soil.

In any case, the complexity of such study, linked to the presence of a great number of uncontrollable and varying parameters and processes affecting the radon transport in the source medium, suggested us to carry out a laboratory study on radon transport under well-specified and controlled conditions. For this purpose, a laboratory facility was built, consisting of a large cylindrical stainless steel vessel, homogeneously filled with different materials, with inserted sleeves that allow measurements of radon

concentration in the sample pores at various depths. Radon concentration vertical profiles were extracted for different advective fluxes, corresponding to air-flow rates between 0.2 and 0.8 liter/min, different temperatures, in the range 29-96 °C, and porosities, arising from four different type of samples (volcanic sand, volcanic rock, marble sand and clay). The experimental results were also compared with those expected by a theoretical model proposed by Andersen. The input parameters for the transport model, relatively to material samples, were obtained separately: the specific density by weighing, the radium content using gamma-ray spectroscopy, the emanation coefficient with a closed-can method and the porosity, the most important one in our laboratory study, from the mass increase due to water saturation. Other parameters were measured, like pressure differences between the bottom and the top of the column and the air-flow rate, or estimated from these measurements, like sample permabilities. The diffusion coefficient for radon in air, furthermore, was extracted from fit radon transport model data to experimental results.

The vessel measurements have shown that, within the uncertainties of the experimental conditions, combined diffusive and advective radon transport can be reproduced by model calculations on the basis of known transport processes and measured parameters. In general, the agreement between experimental data and model calculations is quite good. The measured concentration profiles follow a reasonably smooth curve and no notable deviations from the simulations seems to occur in the lower part of the vessel, while discrepancies, occasionally up to 30%, were observed near the top of the sample column, probably due to greater amounts of moisture than modelled or barometric effects. A strong dependence from the sample temperature is clearly shown by the increase of bulk diffusivity with increasing temperature, the diffusion coefficient changing of a order of magnitude (from 10^{-6} to 10^{-5}) over a increase in temperature of less than 70 °C, independently from sample porosity.

In overviewing the measurements with the radon vessel, it has been demonstrated that the research strategy of starting with simple porous media has proven to be a good choice. This, because the transport processes in these simple materials already turned out to be complex and difficult to model in some cases. In the light of the good results

obtained we are currently studying the possibility to improve our methodology, in order to take into account, for example, layers of different materials inside the vessel to approach more real geological conditions and/or higher temperatures to simulate volcanic environments.

In this context, more systematic *in situ* studies are also necessary and, in the framework of a collaboration with Czech Technical University in Prague (Czech Republic), we are carrying out geophysical investigations for imaging sub-surface structures by means of Electrical Resistivity Tomography technique (ERT), in order to better correlate the radon concentrations profiles to the local geological situations. Such analysis, together with more detailed laboratory studies, in which we can take under control other physical parameters (first of all the moisture content), could be a very useful tool for at least three important reasons: to correlate deep-soil radon concentrations anomalies to geodynamic events (both volcanic and tectonic), to characterize geological formations with confinement properties, porosity and permeability, ideal for storage of radioactive waste and, from a radioprotection point of view, to determine conditions of compaction of building materials in order to reduce the diffusion through them in indoor environments.

Appendix A

```
program radonprg;
(* ---------------------- RnMod3d jobfile ---------------------- *)
(* Project: Roberto Catalano PhD thesis:                        *)
(*          Steady radon diffusion + advection, 1D.             *)
(*          Column of inhomogeneous sample (three layers)       *)
(* Created: December 11, 2012                                   *)
(* Revised: January 16, 2013                                    *)

{$I R3dirs03}
uses
  R3Defi03,
  R3Main03,
  R3Writ03;

(*We define the Radon decay constant, the dynamic viscosity and the Ostwald*)
(*partitioning coefficient*)
const lambda_use = 2.09838e-6; (* 1/s *)
      mu         = 17.5e-6;    (* Pa s *)
      LOstwald   = 0.3016;     (* water/gas partitioning at T = 288.15 K *)

var ksoil,cS,dP,velocity,Lx,Ly,Lz,Lz1,Lz2,Dsoil,esoil,Gsoil,N:datatype;
var k2,k3,k4:datatype;               (*Input soil permeability*)
var esoil2,esoil3,esoil4:datatype;   (*Input porosity*)
var Dsoil2,Dsoil3,Dsoil4:datatype;   (*Input bulk diffusivity*)
var rhog2,rhog3,rhog4:datatype;      (*Input grain density*)
var frac2,frac3,frac4:datatype;      (*Input fraction of emanation*)
var ARa2,ARa3,ARa4:datatype;         (*Input Ra-226 activity concentration*)

(*We create the grid of control volumes by subdividing each of the three axes*)
procedure grid;
begin
set_FixVal(xFix1,0.0);  (*x-axis*)
set_FixVal(xFix2, Lx);
set_axis_single(xFix1,xFix2,1,FocusA,1.0);

set_FixVal(yFix1,0.0);  (*y-axis*)
set_FixVal(yFix2, Ly);
set_axis_single(yFix1,yFix2,1,FocusA,1.0);

set_FixVal(zFix1,0.0);  (*z-axis*)
set_FixVal(zFix2,Lz1);
set_FixVal(zFix3,Lz1+Lz2);
set_FixVal(zFix4, Lz);
set_axis_double(zFix1,zFix2,30,30,FocusA,FocusB,2,2,0.5);
set_axis_double(zFix2,zFix3,30,30,FocusA,FocusB,2,2,0.5);
set_axis_double(zFix3,zFix4,30,30,FocusA,FocusB,2,2,0.5);
end;

(*We set the soil gas boundary condition by introducing a pressure difference field*)
(*between the top and the bottom of the column*)
procedure boundary_conditions_Soilgas(i:itype;j:jtype;k:ktype);
begin
cBC[fixed1]:=dP;     (*bottom*)
if in_plane([inside,eqAB],
            i,xFix1,xFix2,
            j,yFix1,yFix2,
            k,zFix1,zFix1) then set_node(i,j,k,fixed1);
cBC[fixed2]:=0.0;    (*top*)
```

```
if in_plane([inside,eqAB],
            i,xFix1,xFix2,
            j,yFix1,yFix2,
            k,zFix4,zFix4) then set_node(i,j,k,fixed2);
end;

(*We impose the boundary conditions*)
procedure boundary_conditions_Rn(i:itype;j:jtype;k:ktype);
begin
cBC[fixed1]:=cS;   (*Deep-soil Radon concentration at the bottom*)
if in_plane([inside,eqAB],
            i,xFix1,xFix2,
            j,yFix1,yFix2,
            k,zFix1,zFix1) then set_node(i,j,k,fixed1);
cBC[fixed2]:=0.0;   (*No Radon at the Earth's surface*)
if in_plane([inside,eqAB],
            i,xFix1,xFix2,
            j,yFix1,yFix2,
            k,zFix4,zFix4) then set_node(i,j,k,fixed2);
end;

(*We introduce the flux measurement probes in order to monitor the fluxes at zFix1,*)
(*zFix2, zFix3 and zFix4*)
procedure fluxes(i:itype;j:jtype;k:ktype);
begin
if in_plane([inside,eqAB],
            i,xFix1,xFix2,
            j,yFix1,yFix2,
            k,zFix1,zFix1) then update_flxval(Flx1,top,i,j,k,plus);
if in_plane([inside,eqAB],
            i,xFix1,xFix2,
            j,yFix1,yFix2,
            k,zFix2,zFix2) then update_flxval(Flx2,top,i,j,k,plus);
if in_plane([inside,eqAB],
            i,xFix1,xFix2,
            j,yFix1,yFix2,
            k,zFix3,zFix3) then update_flxval(Flx3,top,i,j,k,plus);
if in_plane([inside,eqAB],
            i,xFix1,xFix2,
            j,yFix1,yFix2,
            k,zFix4,zFix4) then update_flxval(Flx4,bottom,i,j,k,plus);
end;

(*This procedure finds the field value in the middle of the column*)
procedure probes;
var cc:datatype; valid:boolean;
begin
cc:=fieldvalue(0.5,0.5,Lz/2,valid);
if not valid then cc:=0.0;
obsval[obs1]:=cc;
end;

(*We consider the inhomogeneous problem with different materials in the column*)
(*experiment*)
function materials(i:itype;j:jtype;k:ktype):mattype;
var mat:mattype;
begin
mat:=mat1;
if in_cube([inside,eqAB],i,xFix1,xFix2,j,yFix1,yFix2,k,zFix1,zFix2) then
(*First layer from the bottom*)
mat:=mat2;
if in_cube([inside,eqAB],i,xFix1,xFix2,j,yFix1,yFix2,k,zFix2,zFix3) then
(*Second layer from the bottom*)
mat:=mat3;
if in_cube([inside,eqAB],i,xFix1,xFix2,j,yFix1,yFix2,k,zFix3,zFix4) then
(*Third layer from the bottom*)
mat:=mat4;
materials:=mat;
end;
```

```
(*We define a function that describes the moisture saturation profile*)
function m(i:itype;j:jtype;k:ktype):datatype;
var mres,depth:datatype;
begin (*Moisture saturation, m=ew/e*)
depth:=znod(k);
mres:=0.10-0.9*depth;   (*Moisture saturation vertical profile*)
if mres>1 then mres:=1;
if mres<0 then error_std('Moisture error!');
m:=mres;
end;

(*Variables of the soil gas problem*)
function e_soilgas(i:itype;j:jtype;k:ktype):datatype;
begin
e_soilgas:=0;
end;

function beta_soilgas(i:itype;j:jtype;k:ktype):datatype;
begin
beta_soilgas:=0;
end;

function D_soilgas(dir:dirtype;i:itype;j:jtype;k:ktype):datatype;
var ksoil:datatype;
begin
ksoil:=0;   (*Variable initialized*)
case materials_def(i,j,k) of   (*Blockwise inhomogeneous soil permeability*)
  mat2: ksoil:=k2;
  mat3: ksoil:=k3;
  mat4: ksoil:=k4;
end;   (*case*)
D_soilgas:=ksoil/mu;
end;

function G_soilgas(i:itype;j:jtype;k:ktype):datatype;
begin
G_soilgas:=0;
end;

function lambda_soilgas(i:itype;j:jtype;k:ktype):datatype;
begin
lambda_soilgas:=0;
end;

(*We define the characteristics of the different materials*)
function e_Rn(i:itype;j:jtype;k:ktype):datatype;
var esoil:datatype;
begin
esoil:=0;   (*Variable initialized*)
case materials_def(i,j,k) of   (*Blockwise inhomogeneous porosity*)
  mat2: esoil:=esoil2;
  mat3: esoil:=esoil3;
  mat4: esoil:=esoil4;
end;   (*case*)
e_Rn:=esoil;
end;

function beta_Rn(i:itype;j:jtype;k:ktype):datatype;
var ea,ew:datatype;
begin
ew:=m(i,j,k)*e_Rn(i,j,k);
ea:=e_Rn(i,j,k)-ew;
beta_Rn:=ea+LOstwald*ew;   (*Blockwise partition-corrected porosity*)
end;

function D_Rn(dir:dirtype;i:itype;j:jtype;k:ktype):datatype;
var Dsoil:datatype;
begin
Dsoil:=0;   (*Variable initialized*)
case materials_def(i,j,k) of   (*Blockwise bulk diffusivity of Radon*)
  mat2: Dsoil:=Dsoil2;
```

```
  mat3: Dsoil:=Dsoil3;
  mat4: Dsoil:=Dsoil4;
end;   (*case*)
D_Rn:=Dsoil;
end;

function Density_soil(i:itype;j:jtype;k:ktype):datatype;
var rhog:datatype;
begin
rhog:=0;   (*Variable initialized*)
case materials_def(i,j,k) of   (*Blockwise soil grain density*)
  mat2: rhog:=rhog2;
  mat3: rhog:=rhog3;
  mat4: rhog:=rhog4;
end;   (*case*)
Density_soil:=rhog;
end;

function Ema_soil(i:itype;j:jtype;k:ktype):datatype;
var frac:datatype;
begin
frac:=0;   (*Variable initialized*)
case materials_def(i,j,k) of   (*Blockwise fraction of emanation*)
  mat2: frac:=frac2;
  mat3: frac:=frac3;
  mat4: frac:=frac4;
end;   (*case*)
Ema_soil:=frac;
end;

function Activity_soil(i:itype;j:jtype;k:ktype):datatype;
var ARa:datatype;
begin
ARa:=0;   (*Variable initialized*)
case materials_def(i,j,k) of   (*Blockwise Ra-226 activity concentration*)
  mat2: ARa:=ARa2;
  mat3: ARa:=ARa3;
  mat4: ARa:=ARa4;
end;   (*case*)
Activity_soil:=ARa;
end;

function G_Rn(i:itype;j:jtype;k:ktype):datatype;
var Gsoil,rhog,esoil,frac,ARa:datatype;
begin
Gsoil:=0;   (*Variable initialized*)
rhog:=Density_soil(i,j,k);
esoil:=e_Rn(i,j,k);
frac:=Ema_soil(i,j,k);
ARa:=Activity_soil(i,j,k);
case materials_def(i,j,k) of   (*Blockwise radon generation rate per pore volume*)
  mat2: Gsoil:=rhog*(1-esoil)/esoil*lambda_use*frac*ARa;
  mat3: Gsoil:=rhog*(1-esoil)/esoil*lambda_use*frac*ARa;
  mat4: Gsoil:=rhog*(1-esoil)/esoil*lambda_use*frac*ARa;
end;   (*case*)
G_Rn:=Gsoil;
end;

function lambda_Rn(i:itype;j:jtype;k:ktype):datatype;
begin
lambda_Rn:=lambda_use;
end;

(*We define the function hyperbolic sine*)
function sinh(x:datatype):datatype;
var z:datatype;
begin
z:=exp(x);
sinh:=(z-1/z)/2
end;
```

```
(*We define the function hyperbolic cosine*)
function cosh(x:datatype):datatype;
var z:datatype;
begin
z:=exp(x);
cosh:=(z+1/z)/2
end;

(*We introduce the equation for steady-state radon concentration profile*)
function c_exact(z:datatype):datatype;
var v,D,cinf,s,alpha,Ld:datatype;
(* See NBS technical note 1139, p. 26, for more details [Collé et al., 1981]*)
begin
D:=Dsoil;
v:=velocity;   (*see below*)
alpha:=v/2/D;
Ld:=sqrt(D/esoil/lambda_use);   (*Diffusion lenght*)
s:=1/sqrt(sqr(alpha)  +  sqr(1/Ld));  (*Diffusion  lenght  modified  by  the  superimposed
flow velocity v*)
cinf:=Gsoil/lambda_use;   (*Deep-soil radon concentration*)
c_exact:=cinf*(1-1/sinh(Lz/s)*(exp(v*z/2/D)*sinh((Lz-z)/s)        +        exp(-v*(Lz-
z)/2/D)*sinh(z/s)))+
         cS*exp(v*z/2/D)*sinh((Lz-z)/s) / sinh(Lz/s);
end;

(*We introduce the equation for the total flow of radon per unit area through the*)
(*surface at z=0*)
function j_exact:datatype;
var v,D,cinf,s,alpha,Ld:datatype;
(* See NBS technical note 1139, p. 26, for more details [Collé et al., 1981]*)
begin
D:=Dsoil;
v:=velocity;   (*see below*)
alpha:=v/2/D;
Ld:=sqrt(D/esoil/lambda_use);   (*Diffusion lenght*)
s:=1/sqrt(sqr(alpha)  +  sqr(1/Ld));  (*Diffusion  lenght  modified  by  the  superimposed
flow velocity v*)
cinf:=Gsoil/lambda_use;   (*Deep-soil radon concentration*)
j_exact:=cinf*(V/2 + D/s/sinh(Lz/s)*(cosh(Lz/s)-exp(v*Lz/2/D)))+
         cS*D/s*exp(v*Lz/2/D)/sinh(Lz/s);
end;

procedure wr_flux;
begin
(*This procedure sets the outputs on the screen for Radon fluxes at z=0*)
writeln(LOG,' dP = ',dP:6:2);
writeln(LOG,'RnMod3d Rn flux at z=0: ',FlxVal[flx4].j:16,' Bq/m2/s');
writeln(LOG,'Exact Rn flux at z=0:   ',j_exact:16,' Bq/m2/s');
writeln(LOG,'Deviation:         ',100*(FlxVal[flx4].j-j_exact)/j_exact:16:4,' %');
end;

procedure wr_profile;
var Nsteps,zstart,zstop,dzz,zz,cc:datatype;
    valid:boolean;
begin
(*This procedure finds the field at (x,y,z) where x=0.5m and y=0.5m, and z is looped*)
(*through the values from top to bottom*)
Nsteps:=N;   (*Number of steps in which the column is subdivided*)
if not (wFixVal[zFix1].defined and wFixVal[zFix4].defined) then
  error_std('wr_profile','Undefined fixpoints!');
zstart:=wFixVal[zFix1].w;
zstop :=wFixVal[zFix4].w;
dzz:=(zstop-zstart)/Nsteps;
zz :=zstart;
writeln(RES,'z':12,',','c':12,',','cexact':12);
while (zz<zstop) do
  begin
    cc:=fieldvalue(0.5,0.5,zz,valid);
    if valid then
      writeln(RES,zz:12:6,',',cc:12:6,',',c_exact(zz):12:6);   (*Output*)
```

```
    zz:=zz+dzz;
  end;
end;

begin (* main *)
runid                          := '0001';
runtitle                       := 'Steady Rn-222 diffusion and advection - Layers of 3
materials';
solution                       := steady;
geometry                       := cartesian3d;
Ly                             := 1.0;
grid_def                       := grid;
flux_def                       := fluxes;
probe_def                      := probes;
materials_def                  := materials;
flux_convset                   := [flx1,flx2];
probe_convset                  := [obs1];
conv_evaluation_period         := 200;
min_iterations                 := 100;
max_iterations                 := 5000;
wr_axes                        := false;
wr_node_numbers                := false;
wr_materials_volumes           := false;

(*We introduce the column characteristics and the disturbance pressure from keyboard*)
WriteLn;
WriteLn (' PLEASE INSERT THE FOLLOWING PARAMETERS:');
WriteLn;
Write (' COLUMN SIZE ALONG THE X-DIRECTION (in m):  ');
readLn(Lx);
Write (' COLUMN SIZE ALONG THE Y-DIRECTION (in m):  ');
ReadLn(Ly);
Write (' COLUMN DEPTH (in m):  ');
ReadLn(Lz);
Write (' PRESSURE DIFFERENCE (in Pa):  ');
ReadLn(dP);
Write (' NUMBER OF STEPS IN WHICH THE COLUMN IS SUBDIVIDED: ');
ReadLn(N);
WriteLn;

(*User-defined soil characteristics from keyboard*)
WriteLn (' CHARACTERISTICS OF THE FIRST LAYER FROM THE BOTTOM');   (*First layer*)
Write (' THICKNESS (in m): ');
ReadLn(Lz1);
Write (' SOIL PERMEABILITY (in m^2):  ');
ReadLn(k2);
Write (' BULK DIFFUSIVITY (in m^2 s^-1):  ');
ReadLn(Dsoil2);
Write (' POROSITY:  ');
ReadLn(esoil2);
Write (' DENSITY OF THE GRAIN MATERIAL (in kg m^-3):  ');
ReadLn(rhog2);
Write (' RN-222 EMANATION FRACTION FROM SOIL GRAINS:  ');
ReadLn(frac2);
Write (' RA-226 ACTIVITY CONCENTRATION PER DRY MASS (in Bq kg^-1):  ');
ReadLn(ARa2);
WriteLn;

(*User-defined soil characteristics from keyboard*)
WriteLn (' CHARACTERISTICS OF THE SECOND LAYER FROM THE BOTTOM');   (*Second layer*)
Write (' THICKNESS (in m): ');
ReadLn(Lz2);
Write (' SOIL PERMEABILITY (in m^2):  ');
ReadLn(k3);
Write (' BULK DIFFUSIVITY (in m^2 s^-1):  ');
ReadLn(Dsoil3);
Write (' POROSITY:  ');
ReadLn(esoil3);
Write (' DENSITY OF THE GRAIN MATERIAL (in kg m^-3):  ');
ReadLn(rhog3);
```

```
Write (' RN-222 EMANATION FRACTION FROM SOIL GRAINS:  ');
ReadLn(frac3);
Write (' RA-226 ACTIVITY CONCENTRATION PER DRY MASS (in Bq kg^-1):  ');
ReadLn(ARa3);
WriteLn;

(*User-defined soil characteristics from keyboard*)
WriteLn (' CHARACTERISTICS OF THE THIRD LAYER FROM THE BOTTOM');   (*Third layer*)
Write (' SOIL PERMEABILITY (in m^2):  ');
ReadLn(k4);
Write (' BULK DIFFUSIVITY (in m^2 s^-1):  ');
ReadLn(Dsoil4);
Write (' POROSITY:  ');
ReadLn(esoil4);
Write (' DENSITY OF THE GRAIN MATERIAL (in kg m^-3):  ');
ReadLn(rhog4);
Write (' RN-222 EMANATION FRACTION FROM SOIL GRAINS:  ');
ReadLn(frac4);
Write (' RA-226 ACTIVITY CONCENTRATION PER DRY MASS (in Bq kg^-1):  ');
ReadLn(ARa4);
WriteLn;

Dsoil := 0.1;   (*The program needs this line to generate a valid RES file. The*)
(*value given to Dsoil is irrelevant to the result!*)
esoil := 0.1;   (*The program needs this line to generate a valid RES file. The*)
(*value given to esoil is irrelevant to the result!*)
Gsoil := 0.1;   (*The program needs this line to generate a valid RES file. The*)
(*value given to Gsoil is irrilevant to the result!*)

velocity:=ksoil/mu*dP/Lz;   (*The program calculates the flow velocity from bottom*)
(*to top*)
cS:=rhog2*(1-esoil2)/esoil2*frac2*ARa2;   (*The program calculates the deep-soil*)
(*Radon concentration at the bottom of the column*)

(* First, the soil gas problem *)
boundary_conditions_def      := boundary_conditions_soilgas;
D_def                        := D_soilgas;
e_def                        := e_soilgas;
beta_def                     := beta_soilgas;
G_def                        := G_soilgas;
lambda_def                   := lambda_soilgas;
flowfield                    := export_to_qBUF;
relax_factor                 := 1.9;
max_change                   := 1e-12;
max_residual_sum             := 3e-16;
run_model;

(* Second, the radon problem *)
flowfield                    := import_from_qBUF;
boundary_conditions_def      := boundary_conditions_Rn;
D_def                        := D_Rn;
e_def                        := e_Rn;
beta_def                     := beta_Rn;
G_def                        := G_Rn;
lambda_def                   := lambda_Rn;
relax_factor                 := 1.0;
max_change                   := 1e-12;
max_residual_sum             := 3e-16;
run_model;

wr_flux;
wr_profile;
close_model;
end.
```

References

1. Abu-Jarad F. (1988). *Application of nuclear track detectors for radon related measurements*. Nuclear Tracks and Radiation Measurements **15**, 1, 525-534.

2. Ajari T.R., Adepelumi A.A. (2002). *Reconnaissance soil-gas Radon survey over faulted crystalline area of Ile-Ife, Nigeria*. Environmental Geology **41**, 608-613.

3. Alzaydi A.A., Moore C.A. (1978). *Combined pressure and diffusional transition region flow of gases in porous media*. American Institute of Chemical Journal **24**, 1, 35-43.

4. Andersen C.E. (1992). *Entry of Soil Gas and Radon into Houses*. PhD Thesis, Risø National Laboratory, DK-4000, Roskilde, Denmark.

5. Andersen C.E., Albarracín D., Csige I., van der Graaf E.R., Jiránek M., Rehs B., Svoboda Z., Toro L. (1999). *ERRICCA radon model intercomparison exercise*. Risø-R-1120, Risø National Laboratory, DK-4000, Roskilde, Denmark (available as internet publication at http://www.risoe.dk).

6. Andersen C.E. (2001). *Numerical modelling of radon-222 entry into houses: an outline of techniques and results*. The Science of the Total Environment **272**, 33-42.

7. Atallah M.Y., Al-Bataina B.A., Mustafa H. (2001). *Radon emanation along the Dead Sea transform (rift) in Jordan*. Environmental Geology **40**, 1440-1446.

8. Aureli A. (1973). *Idrogeologia del fianco occidentale etneo*. In: Proceedings of the Second International Congress on Underground Waters, Palermo, Italy, 425-487.

9. Azzaro R. (1999). *Earthquake surface faulting at Mount Etna volcano (Sicily) and implications for active tectonics*. Journal of Geodynamics **28**, 193-213.

10. Azzaro R., Branca S., Gwinner K., Coltelli M. (2012). *Volcano-Tectonic map of Etna volcano*. The Italian Journal of Geosciences (Bollettino della Società Geologica Italiana e del Servizio Geologico d'Italia) Vol. **131**, No. X.

11. Azzaro R., Bonforte A., Branca S., Guglielmino F. (2013). *Geometry and kinematics of the fault systems controlling the unstable flank of Etna volcano (Sicily)*. Journal of Volcanology and Geothermal Research **251**, 5-15.

12. Bartlett D.T., Gilvin P.J., Still R., Dixon D.W., Miles J.C.G. (1988). *The NRPB radon personal dosimetry service*. Journal of Radiological Protection **8** (1), 19-24.

13. Baubron J.-C., Rigo A., Toutain J.-P. (2002). *Soil-gas profiles as a tool to characterise active tectonic areas: the Jaut Pass example (Pyrenees, France)*. Earth and Planetary Science Letters **196**, 69-81.

14. Bear J. (1979). *Hydraulics of groundwater*. McGraw-Hill International Book Co., ISBN 007-00-4170-9.

15. Bird R.B., Stewart W.E., Lightfoot E.N. (1960). *Transport phenomena*. John Wiley and Sons.

16. Bruno N., Caltabiano T., Giammanco S., Romano R. (2001). *Degassing of SO_2 and CO_2 at Mount Etna (Sicily) as an indicator of pre-eruptive ascent and shallow emplacement of magma*. Journal of Volcanology and Geothermal Research **110**, 137-153.

17. Brusseau M.L. (1991). *Transport of organic chemicals by gas advection in structured or heterogeneous porous media: Development of a model and application to column experiments*. Water Resources Research **27**, 12, 3189-3199.

18. Burton M., Neri M., Condarelli D. (2004). *High spatial resolution radon measurements reveal hidden active faults on Mt. Etna*. Geophysical Research Letters **31**, L07618, doi: 10.1029/2003GL019181.

19. Campbell G. (1974). *A simple method for determining unsaturated conductivity from moisture retention data*. Soil Science **117**, 6, 331-314.

20. Chen C., Thomas D.M., Green R.E. (1995). *Modeling of radon transport in unsaturated soil*. Journal of Geophysical Research **100**, B8, 15517-15525.

21. Chiodini G., Cioni R., Guidi M., Raco B., Marini L. (1998). *Soil CO_2 flux measurements in volcanic and geothermal areas*. Applied Geochemistry **13**, 135-148.

22. Clever H.L. (ed.) (1979). *Solubility data series*. Volume 2, Krypton, xenon and radon - gas solubilities. Pergamon Press.

23. Collé R., Rubin R.J., Knab L.I., Hutchinson J.M.R. (1981). *Radon transport through and exhalation from building materials: A review and assessment*. NBS Technical Note 1139. National Bureau of Standards, U.S. Department of Commerce, Washington, DC 20234.

24. D'Alessandro W., De Domenico R., Parello F., Valenza M. (1992). *Soil degassing in tectonically active areas of Mt. Etna*. Acta Vulcanol. **2**, 175-183.

25. Domenico P.A., Schwartz F.W. (1992). *Physical and Chemical Hydrogeology*. John Wiley and Sons.

26. Durridge Company Inc. (2000). Reference Manual version 6.0.1, RAD7^{TM} Electronic Radon Detector.

27. Falta R.W., Javandel I., Pruess K. (1989). *Density-driven flow of gas in the unsaturated zone due to the evaporation of volatile organic compounds*. Water Resources Research **25**, 10, 2159-2169.

28. Ferrara V. (1975). *Idrogeologia del fianco orientale dell'Etna*. In: Proceedings of the Third International Congress on Underground Waters, Palermo, Italy, 91-144.

29. Ferziger J.H., Perić. (1999). *Computational methods for fluid dynamics.* Second Edition, Springer, Berlin, Germany.

30. Fleischer R.L. (1980). *Isotopic disequilibrium of uranium: Alpha-recoil damage and preferential solution effects*. Science **207**, 979-981.

31. Garbesi K. (1993). *Toward resolving model-measurement discrepancies of radon entry into houses*. LBL-34244, Lawrence Berkeley Laboratory, CA 94720, USA.

32. Gauthier P-J., Condomines M., Hammouda T. (1999). *An experimental investigation of radon diffusion in a anhydrous andesitic melt at atmospheric pressure: implication for radon degassing from erupting magmas*. Geochimica et Cosmochimica Acta **63**, 5, 645-656.

33. Gauthier P-J., Condomines M. (1999). *^{210}Pb - ^{226}Ra radioactive disequilibria in recent lavas and radon degassing: inferences on the magma chamber dynamics at Stromboli and Merapi volcanoes*. Earth and Planetary Science Letters **172**, 1-2, 111-126.

34. Giammanco S., Gurrieri S., Valenza M. (1995). *Soil CO_2 degassing on Mt. Etna (Sicily) during the period 1989-1993: Discrimination between climatic and volcanic influences*. Bullettin of Volcanology **57**, 52-60.

35. Gierke J.S., Hutzler N.J., Crittenden J.C. (1990). *Modeling the movement of volatile organic chemicals in columns of unsaturated soil*. Water Resources Research **26**, 7, 1529-1547.

36. Goh T.B., Oscarson D.W., Cheslock M., Shaykewich C. (1991). *Fluence rate of radon from soil: Effect of sorption barriers, moisture content, and temperature*. Health Physics **61**, 3, 359-365.

37. He B., Shang A-G., Guo H-P. (1998). *Discussion about surface boundary conditions of radon concentration and surface exhalation rate calculations in indoor concrete slab*. Health Physics **74**, 3, 366-369.

38. Helmig R. (1996). *Einführung in die numerischen Methoden der Umweltströmungsmechanik*. Institut für Computer Anwendungen im Bauingenieurwesen, Techniche Universität Braunschweig, Germany.

39. Hoff A. (1997). *Radon transport in fractures soil: Laboratory experiments and modelling*. Ph.D. dissertation, Risø-R-975 (EN), Risø National Laboratory, DK-4000, Roskilde, Denmark.

40. Holford D.J., Schery S.D., Wilson J.L., Phillips F.M. (1993). *Modeling radon transport in dry, cracked soil*. Journal of Geophysical Research **98**, B1, 567-580.

41. Immé G., Morelli D., Aranzulla M., Catalano R., Mangano G. (2013). *Nuclear track detector characterization for alpha-particle spectroscopy*. Radiation Measurements **50**, 253-257.

42. Janssen M.P.M., de Vries L., Phaff J.C., van der Graaf E.R., Blaauboer R.O., Stoop P., Lembrechts J. (1998). *Modelling radon transport in Dutch dwellings*. RIVM report no. 610050005, Bilthoven, the Netherlands.

43. Jönsson G. (2001). *Soil radon depth dependence*. Radiation Measurements **34**, 415-418.

44. Jury W.A., Spencer W.F., Farmer W.J. (1984). *Behavior assessment model for trace organics in soil: I. Model description*. Journal of Environmental Quality **13**, 567-572.

45. Jury W.A., Spencer W.F., Farmer W.J. (1984). *Behavior assessment model for trace organics in soil: IV. Review of experimental evidence*. Journal of Environmental Quality **13**, 4, 580-586.

46. Kigoshi K. (1971). *Alpha-recoil ^{234}Th: Dissolution into water and the $^{234}U/^{238}U$ disequilibrium in nature*. Science **173**, 47-48.

47. Kolomoiesky A.B., Widom B. (1999). *Model of the hydrophobic interaction*. Faraday Discussions **12**, 81-89.

48. Kovler K. (2006). *Radon exhalation of hardening concrete: monitoring cement hydration and prediction of radon concentration in construction site*. Journal of Environmental Radioactivity **86**, 354-366.

49. La Delfa S., Patanè G., Clocchiatti R., Joron J-L., Tanguy J.-C. (2001). *Activity of Mount Etna preceding the February 1999 fissure eruption: inferred mechanisms from seismological and geochemical data*. Journal of Volcanology and Geothermal Research **105**, 121-139.

50. La Delfa S., Vizzini F., Patanè G. (2010). *Identification of radon anomalies at Mt. Etna (Sicily) by using three different methods*. Environmental Semeiotics **1**, 1-16, 1971-3460.

51. Lo Giudice E., Patanè G., Rasà R., Romano R.. (1982). *The structural framework of Mount Etna*. Memorie della Società Geologica Italiana **23**, 125-158.

52. Loureiro C.O. (1987). *Simulation of the steady-state transport of radon from soil into houses with basements under constant negative pressure*. LBL-24378, Lawrence Berkeley Laboratory, CA 94720 USA.

53. Markkanen M., Arvela H. (1992). *Radon emanation from soils*. Radiation Prot. Dosimetry **45**, 269-272.

54. Massmann J.W. (1989). *Applying groundwater flow models in vapor extraction system design*. Journal of Environmental Engineering **115**, 129-149.

55. Meschendorp J.G. (1994). *Properties of porous media: measurements on, and modelling of permeability and tortuosity*. Master's thesis, Rijksuniversiteit Groningen, KVI Report R-76.

56. Modgil S.K., Virk H.S. (1984). *Effect of etchant concentration and temperature on bulk etch rate for solid state track detectors*. Nuclear Tracks and Radiation Measurements **8**, 95-98.

57. Monaco C., Tortorici L. (2000). *Active faulting in the Calabrian arc and eastern* Sicily. Journal of Geodynamics **29**, 407-424.

58. Nazaroff W.W., Moed B.A., Sextro R.G. (1988). *Soil as a source of Indoor Radon: Generation, Migration, and Entry*. In: Nazaroff W.W. and Nero A.V. (eds.). Radon and its Decay Products in Indoor Air. Wiley-Interscience.

59. Nazaroff W.W. (1992). *Radon transport from soil to air*. Review of Geophysics **30**, 2, 137-160.

60. NIH, http://rsb.info.nih.gov/ij/.

61. Nilson R.H., Peterson E.W., Lie K.H. (1991). *Atmospheric pumping: A mechanism causing vertical transport of contaminated gasses through fracturated permeable media*. Journal of Geophysical Research **96**, B13, 21933-21948.

62. Olsen S.R., Kemper W.D. (1968). *Movement of nutrients to plant roots*. Advances in Agronomy **20**, 91-151.

63. Patanè G., Montalto A., Imposa S., Menza S. (1994). *The role of regional tectonics, magma pressure and gravitational spreading in earthquakes of the eastern sector of Mt. Etna volcano (Italy)*. Journal of Volcanology and Geothermal Research **61**, 253-266.

64. Patankar S.V. (1980). *Numerical heat transfer and fluid flow*. Hemisphere Publishing Corporation, New York.

65. Petersen L.W., El-Farhan Y.H., Moldrup P., Rolston D.E., Yamaguchi T. (1996). *Transient diffusion, adsorption, and emission of volatile organic vapors in soils with fluctuating low water contents*. Journal of Environmental Quality **25**, 5, 1054-1063.

66. Riley W.J., Gadgil A.J., Bonnefous Y.C., Nazaroff W.W.. (1996). *The effects of steady winds on radon-222 entry from soil into houses*. Atmospheric Environment **30**, 7, 1167-1176.

67. Rogers V.C., Nielson K.K. (1991). *Multiphase radon generation and transport in porous materials*. Health Physics **60**, 6, 807-815.

68. Rogers V.C., Nielson K.K. (1993). *Generalized Source Term for the Multiphase Radon Transport Equation*. Health Physics **64**, 3, 324-326.

69. Rogers V.C., Nielson K.K., Holt R.B., Snoddy R. (1994). *Radon diffusion coefficients for residential concretes*. Health Physics **67**, 3, 261-265.

70. Rose A.R., Ciolkosz E.J., Washington J.W. (1990). *Effects of regional and seasonal variations in soil moisture and temperature on soil gas transport*. The International Symposium on Radon and Radon Reduction Technology: Volume III. Preprints. EPA/600/9-90/005c. Paper number: C-VI-5. January 1990.

71. Roselieb K., Rammensee W., Büttner H., Rosenhauer M. (1995). *Diffusion of noble gases in melts of the system SiO_2-$NaAlSi_2O_6$*. Chemical Geology **120**, 1-13.

72. Sabol J., Weng P.-S. (1995). *Introduction to radiation protection dosimetry*. World Scientific Publishing Co. Pte. Ltd., Singapore, ISBN 981-02-2116-9.

73. Schery S.D., Gaeddert D.H., Wilkening M.H. (1984). *Factors affecting exhalation of radon from a gravelly sandy loam*. Journal of Geophysical Research **89**, D5, 7299-7309.

74. Sing S., Kumar M., Mahajan R.H. (2004). *The study of indoor radon in dwellings of Bathinda district, Punjab, India and its correlation with uranium and radon exhalation rate in soil*. Radiation Measurements **39**, 535-542.

75. Spencer W.F., Cliath M.M. (1990). *Movement of pesticides from soil to the atmosphere*. In: Long Range Transport of Pesticides, edited by D.A. Kurtz, pp. 1-15, Lewis, Chelsea, Mich.

76. Surbeck H. (1996). *A Radon-in-water monitor based on fast gas transfer membranes*. In: International Conference on Technologically Enhanced Natural Radioactivity (TENR) caused by non-uranium mining, October 16-19, 1996, Szczyrk (PL).

77. Tanner A.B. (1980). *Radon migration in the ground: A supplementary review*. In: Natural Radiation III, edited by T.F. Gesell and W. M. Lowder, U.S.D.O.E. Rep. CONF-780422, pp. 5-56, U.S. Dep. of Energy, Washington, D.C.

78. Tanner A.B. (1988). *A tentative protocol for measurement of radon availability from the ground*. Northeastern Environmental Science **7**, 1, 58-62.

79. Taylor A.W., Spencer W.F. (1990). *Volatilization and vapor transport processes*. In: Pesticides in the Soil Environment, SSSA Book Ser., no. 2, pp. 213-269, Soil Sci. Soc. of Am., Madison, Wis.

80. Thomas D.M., Cotter J.M., Holford D. (1992). *Experimental design for soil gas radon monitoring*. Journal of Radioanalytical and Nuclear Chemistry **96**, 2, 313-323.

81. Thomson N.R., Sykes J.F., van Vliet D. (1997). *A numerical investigation into factors affecting gas and aqueous phase plumes in the subsurface*. Journal of Contaminant Hydrology **28**, 39-70.

82. Thorstenson D.C., Pollock D.W. (1989). *Gas transport in unsaturated porous media: The adequacy of Fick's law*. Reviews of Geophysics **27**, 1, 61-78.

83. Tonani F., Miele G. (1991). *Methods for measuring flow of carbon dioxide through soils in the volcanic setting*. Istituto di analisi globale e applicazioni C.N.R., Firenze, Italy.

84. UNSCEAR (1988). *Sources, Effects and Risks of Ionizing Radiation*. United Nations Scientific Committee on the Effects of Atomic Radiation, United Nations, New York.

85. Van der Graaf E.R. (1992). *Orientation of the radon vessel and determination of positions of the multi-functional measuring probes*. Technical Report RV-03, KVI, Zernikelaan 25, 9747 AA, Groningen, The Netherlands.

86. van der Spoel W.H., van der Graaf E.R., de Meijer R.J. (1997). *Diffusive transport of radon in a homogeneous column of dry sand*. Health Physics **72**, 5, 766-778.

87. van der Spoel W.H. (1998). *Radon transport in sand: A laboratory study*. Ph.D. dissertation, Technical University Eindhoven, Netherlands, ISBN 90-386-0647-8.

88. Versteeg H.K., Malalasekera W. (1995). *An Introduction to computational fluid dynamics. The finite volume method*. Longman, Edinburg, England.

89. Washington J.W., Rose A.R. (1992). *Temporal variability of radon concentration in the interstitial gas of soils in Pennsylvania*. Journal of Geophysical Research **97**, B6, 9161-9170.

90. Washington J.W., Rose A.R., Ciolkosz E.J., Dobos R.R. (1994). *Gaseous diffusion and permeability in four soil profiles in central Pennsylvania*. Soil Science **157**, 2, 65-76.

91. Wattananikorn K., Kanaree M., Wiboolsake S. (1998). *Soil gas radon as an earthquake precursor: some consideration on data improvement*. Radiation Measurements **29**, 6, 593-598.

92. Wong C.S., Chin Y-P., Gschwend P.M. (1992). *Sorption of radon-222 to natural sediments*. Geochimica and Cosmochimica Acta **56**, 3923-3932.